

Thesis for the Degree of Licentiate of Engineering

Determining the Functional Nanostructure of Polymeric Systems for Electronic Neuro- Pharmaceuticals by Electron Microscopy

Rebecka Rilemark



CHALMERS

Department of Physics

Chalmers University of Technology

Gothenburg, Sweden 2024

Determining the Functional Nanostructure of Polymeric Systems for Electronic Neuro-Pharmaceuticals by Electron Microscopy

Rebecka Rilemark

© Rebecka Rilemark, 2024

Department of Physics
Chalmers University of Technology
SE-412 96 Gothenburg
Sweden
Telephone +46 (0)31 772 3334

Cover image:

Upper left: BF LPTEM image of ETE-S monomer clusters in an electrolyte solution.

Upper middle: SEM secondary electron image of clusters in the PETE-S transistor channel of an OECT.

Upper right: SEM secondary electron image of the porous surface morphology of a hyaluronan hydrogel made conductive by the addition of 5 mg/ml PETE-S.

Lower left: An 8 μ L drop of ETE-PC monomer solution on the bottom chip of a Nano-Cell for the DENSolutions Stream Liquid Biasing holder.

Lower middle: Insertion of a TEM holder into the FEI Titan 80-300 TEM instrument. Image credit: Eric Ljungberg.

Lower right: The JEOL JSM-7800F Prime SEM instrument.

Printed at Chalmers Digital Printing
Gothenburg, Sweden 2024

Determining the Functional Nanostructure of Polymeric Systems for Electronic Neuro-Pharmaceuticals by Electron Microscopy

Rebecka Rilemark

Department of Physics

Chalmers University of Technology

Abstract

Advances in diagnostics and therapies for brain disorders are opening new treatment options. While typical treatments rely on biochemical mechanisms and invasive electrical therapies, electronic neuro-pharmaceuticals have recently emerged as an alternative. These pharmaceuticals are based on creating organic electronic devices *in vivo* within brain tissue. The material of such devices must be soft enough to integrate with the central nervous system tissue, conduct both electronic and ionic signals, and be small enough for the brain. Water-soluble thiophene-based monomer precursors of conducting polymers are promising candidates. These monomers have been used to create biocompatible electrodes through *in vivo* polymerisation in living organisms, in neuromorphic organic electrochemical transistors (OECTs), and in conducting hydrogels. However, the detailed structure of the materials in these bioelectronics is not well known. Knowledge about the material structure is important for understanding and optimising the physical properties.

This thesis uses electron microscopy to investigate the micro- and nanostructure of polymeric systems for electronic neuro-pharmaceuticals. The evolution of material structures is studied using transmission electron microscopy (TEM), liquid-phase TEM, scanning electron microscopy (SEM), and atomic force microscopy (AFM). This work shows that the morphology of electropolymerised transistor channels for OECTs is influenced by the surface for film growth, with a smooth polymer film forming directly on surface modified OECT substrates. Subsequent growth on the polymer surface leads to a more rough surface morphology. In addition, large aggregates containing nanoscale features are found in the film. Imaging of monomer solutions reveals nanoscale aggregation, which impacts the morphology of OECT films in regions of low electric potential. This thesis also studies enzymatically polymerised conducting hydrogels, which show promise as scaffolds for 3D neural cell cultures. The porosity of the hydrogels is a key factor. SEM analysis shows that increased conducting polymer content leads to larger pore sizes but reduced interconnectivity. The findings in this work provides important structural information needed to understand and optimise the properties of neuro-pharmaceuticals.

Keywords: Electron microscopy, conducting polymer, morphology, structural evolution, OECT, aggregation, hydrogel, neuro-pharmaceuticals

Acknowledgements

This thesis is based on research carried out in the Eva Olsson Group at the Division of Nano and Biophysics, Department of Physics at Chalmers University of Technology. This work was performed in part at the Chalmers Material Analysis Laboratory, CMAL.

This work is part of the e-NeuroPharma project, funded by VR strategic research environment, in collaboration with researchers at Linköping University and Lund University.

If there is one thing I have learned during my time as a PhD student, it is that things - experimental work in particular - will never work out quite the way you had expected the first time around. There are always new opportunities and challenges showing up. I would like to express my gratitude to a number of people who have helped me navigate during my PhD studies: My supervisor Eva Olsson for guiding me through my thesis work, offering valuable discussions to better my understanding of the fields of electron microscopy and material science, enabling helpful connections to other researchers and creating an inspiring work environment. My co-supervisor Christian Müller for offering to share your expertise on polymers and organic electronics. All members of the Eva Olsson Group for all your knowledge and insights during our scientific (and not so scientific) discussions that help foster a curious and creative research environment. I would especially like to thank Maria Brollo and Alok Ranjan for all the cheerful conversations around our offices. Thanks to Stefan Gustafsson, Ludvig de Knoop and Katarina Logg from CMAL for all your help with the electron microscopes and equipment in the labs. To Ola Löfgren for powering through all technological issues.

I also want to thank my collaborators at Linköping University and Lund University for all your inspiring work that acts as a constant motivating force. An extra portion of gratitude goes to Jennifer Gerasimov, Benjamin Granroth, Diana Priyadarshini and Changbai Li at the Laboratory of Organic Electronics for always welcoming me with open arms, teaching me more about bioelectronics and providing further insight into the conducting polymers used in this project.

At last, I would like to thank my friends and family for all the love and support they always show. Thanks to my dogs and cats for always keeping both my feet and my heart warm. To my partner Jakob for always pulling me out into the fresh air when needed. And finally, thank you dear reader for showing interest in this thesis.

List of appended papers

This thesis is based on the following papers:

Paper I

Nanostructure evolution of electropolymerized transistor channels in organic electrochemical transistors

Rebecka Rilemark, Benjamin Granroth, Jennifer Y. Gerasimov, Alok Ranjan, Simone Fabiano, Daniel T. Simon, Magnus Berggren, and Eva Olsson

In manuscript

Paper II

Tuning the organic electrochemical transistor (OECT) threshold voltage with monomer blends

Diana Priyadarshini, Changbai Li, Rebecka Rilemark, Tobias Abrahamsson, Mary J. Donahue, Xenofon Strakosas, Fredrik Ek, Roger Olsson, Chiara Musumeci, Simone Fabiano, Magnus Berggren, Eva Olsson, Daniel T. Simon, and Jennifer Y. Gerasimov

Advanced Electronic Materials, (Submitted)

Paper III

Engineering conductive hydrogels with tissue-like properties: a 3D bioprinting and enzymatic polymerization approach

Changbai Li, Sajjad Naeimipour, Fatemeh Rasti Boroojeni, Tobias Abrahamsson, Xenofon Strakosas, Yangpei Yi, Rebecka Rilemark, Caroline Lindholm, Venkata K. Perla, Chiara Musumeci, Yuyang Li, Hanne Biesmans, Marios Savvakis, Eva Olsson, Klas Tybrandt, Mary J. Donahue, Jennifer Y. Gerasimov, Robert Selegård, Magnus Berggren, Daniel Aili and Daniel T. Simon

Small Science, (Published online September 01, 2024)

DOI: 10.1002/smssc.202400290

My contributions to the appended papers

Paper I: I planned the study together with Benjamin Granroth who fabricated the samples. All SEM, FIB and TEM experiments and image analysis was performed by me. I participated in AFM measurements together with Alok Ranjan and performed the data analysis after the experiments. Interpretation of all data was carried out together with the co-authors. I wrote the initial draft of the manuscript and finalized it together with my co-authors.

Paper II: I prepared TEM samples and carried out CV experiments to control the quality of the samples and experimental setup. I performed TEM and SEM experiments, interpreted the data and wrote parts of the manuscript together with my co-authors.

Paper III: I performed SEM and FIB experiments on samples prepared by my co-authors and performed all image analysis on the resulting data. I interpreted the results of the structural characterisation in relation to results from experiments on mechanical properties and cytocompatibility together with my co-authors. I wrote parts of the manuscript together with my co-authors.

Contents

List of Figures	xi
List of Abbreviations	xviii
1 Introduction	1
1.1 Background	1
1.2 Scope of the Thesis	3
2 Organic Electronics Used for Treatment of Neurodegenerative Diseases	5
2.1 Conducting Polymers	5
2.1.1 The Building Blocks of Polymers	5
2.1.2 Electronic Properties of Conducting Polymers	6
2.1.3 Charge Transport in Conducting Polymers	7
2.1.4 Conducting Polymers in Organic Electronics	9
2.2 Organic Electronics	9
2.2.1 Characteristics of Organic Electronics	9
2.2.2 Signalling in Biological Systems	10
2.2.3 Electronic and Ionic Conductivity	11
2.2.4 Bioelectronic Interfaces with Cells	11
2.3 Organic Electrochemical Transistors (OECTs)	12
2.3.1 Structure, Physics and Electronic Properties of OECTs . . .	13
2.3.2 Materials in OECTs	15
2.4 Conducting Hydrogels for Cell Cultures and Neural Tissue Engineering	16
2.4.1 The Importance of Porosity in Biological Scaffolding and Hydrogels	17
2.4.2 Materials in Conducting Hydrogels	18
3 Experimental Techniques, Methods and Materials	19
3.1 Material Systems	19
3.1.1 ETE-S and ETE-PC	19
3.1.2 OECT Devices	23

3.1.3	Electrically Conducting Hyaluronan Hydrogels	26
3.2	Structural Characterisation	29
3.2.1	Scanning Electron Microscopy (SEM)	29
3.2.2	Transmission Electron Microscopy (TEM)	36
3.2.3	Electron Beam Damage	39
3.2.4	Liquid Phase Transmission Electron Microscopy (LPTEM)	43
3.2.5	Focused Ion Beam - Scanning Electron Microscopy (FIB-SEM)	47
3.2.6	Atomic Force Microscopy (AFM)	49
3.2.7	Sample Preparation for Electron Microscopy	51
3.2.8	Detailed Information About the Instruments and Techniques Applied in This Thesis	53
4	Results and Discussion	57
4.1	Structural Evolution of Conducting Polymer Films in OECTs	57
4.1.1	Nucleation of the Polymer Film	58
4.1.2	Film Evolution	59
4.1.3	A Layered Structure of the Polymer Film	69
4.1.4	Origin of the Aggregates in the Rough Surface Morphology of the Film	70
4.2	Monomer Aggregation in Solution	71
4.2.1	Morphology of ETE Monomer Clusters	71
4.2.2	Polymerisation Properties and Aggregation Behaviour	73
4.2.3	Monomer Aggregates in Solution and in OECT Films	74
4.2.4	Comparison Between Electron Microscopy Characterisation and Alternative Techniques	75
4.3	Correlation Between the Structure of OECT Polymer Films and Their Electronic Properties	75
4.4	Structure of Conducting Hydrogels	76
4.4.1	Structure of Hydrogel Surfaces - Description and Origin of Porous Morphologies	76
4.4.2	Internal Structure of the Hydrogels	79
4.4.3	The Influence of the Material Structures on the Mechanical and Electrical Properties of the Hydrogels and Their Bio- compatibility	81
5	Conclusions and Outlook	83
	Bibliography	87

List of Figures

2.1	Illustration of a) the chemical structure of the conjugated polymer PEDOT-S, here shown with six repeating monomer units, and b) ordering in conjugated polymers due to π - π stacking.	8
2.2	The typical structure of an organic electrochemical transistor showing the source, drain and gate electrodes with an organic semiconductor film in contact with an electrolyte.	13
2.3	Illustration of a hydrogel consisting of a three-dimensional porous network of cross-linked polymers capable of holding large amounts of water. Image created with BioRender.com	17
3.1	Chemical structure of the self-doped conducting polymers a) PETE-S in the reduced state where the sulfonate group on the side chain is compensated by a sodium ion and b) PETE-PC with its zwitterionic side chain. The trithiophenes represent one monomer unit of ETE-S and ETE-PC, respectively.	20
3.2	Determination of onset potential from a cyclic voltammogram of ETE-S using a biasing setup with Pt electrodes. Linear functions are fitted to the cyclic voltammogram before and at the slope of the first peak of the anodic (positive) sweep of the first cycle. This peak represents oxidation of the monomers. The onset potential is taken as the potential value at the intersection of the two lines. The corresponding onset potential for this sample is 0.08 V.	21
3.3	Schematic of the OECT device consisting of a pair of Au source and drain electrodes patterned on an APTES-modified SiO ₂ substrate. A voltage is applied to the drain electrode for a given amount of time to oxidatively electropolymerise the ETE-S monomers in the electrolyte solution.	25
3.4	Schematic of the key components of an SEM. Electrons are emitted by the electron source and accelerated to high velocities by an electric field between the electron source (cathode) and the anode. A set of electromagnetic lenses and apertures are used to control the beam diameter. The scan coils deflect the small diameter beam and raster scan it across the sample surface. Signals are generated at the different positions where the beam interacts with the sample and collected, pixel-by-pixel in synchronisation with the beam by a set of detectors to form an image of the analysed area.	30

- 3.5 Qualitative illustration of the effective interaction volume in SEM. The volume from which secondary electrons, backscattered electrons and characteristic X-rays can escape and be detected is different for each signal type. This volume can be seen as the information depth and is smallest for secondary electrons. 31
- 3.6 Illustration of the effect of surface topography on the SE signal strength. The red circles show the fraction of SEs that can escape from the sample for different surface features including a flat surface (a), a sharp edge (b), a thin structure (c), a valley (d), a thick overhang (e) and an area underneath an overhang (f). The SE yield is highest for edges, tilted surfaces and thin protruding structures. . 35
- 3.7 Light-optical analogy to an SEM image generated with a positively biased E-T detector. A viewer sees a landscape from above, lit with directional light from the Sun and diffuse light scattered from an atmosphere or objects in the landscape. The viewer's line of sight corresponds to the incident electron beam in the SEM. The position of the source of directional light represents the positively biased E-T detector which collects the direct signals from BSEs and SEs. The diffuse light corresponds to SE signals and can be seen even in places not struck by the directional light. For this reason, some signal is detected from side (a) on the triangular feature but the signal is weaker than from side (b) which is facing the E-T detector (Sun). Site (c) is completely dark since it can not be reached by the electron beam (line of sight). 35
- 3.8 Simplified schematic of the typical components of a TEM. Electrons are emitted at the top of the instrument and accelerated by an electric field. The beam is focused using electromagnetic lenses into a broad beam, parallel to the optical axis, or focused beam that illuminates the sample. Objective lenses forms an image of the sample and the diffraction pattern which is further magnified and projected onto the fluorescent screen or CCD camera. Note that different microscopes can have different amounts of lenses and apertures. 37
- 3.9 Schematic of two types of closed liquid cells for TEM. a) Cross section of a silicon microchip system where a liquid sample is placed between two silicon chips with electron beam transparent silicon nitride windows. b) Graphene liquid cell where the liquid sample is encapsulated between two thin sheets of graphene. 44

3.10	Schematic illustration of the typical components in a FIB-SEM. The sample stage is tilted to an angle $\theta \approx 50^\circ - 55^\circ$ so that the ion beam has normal incidence to the sample surface. The FIB column and SEM column are also placed at angle θ relative to each other. This allows the ion beam to perform milling simultaneous to imaging with the electron beam without having to tilt the sample in between operations. A GIS consisting of needles can be used to inject a gas into the specimen chamber.	47
3.11	Schematic illustration of an AFM. The tip and cantilever is scanned over the surface of a sample. Forces between the sample and tip deflects the cantilever in the vertical direction. A laser is reflected off the back of the cantilever into a photodetector to measure the amplitude of the deflection.	50
4.1	Spreading behaviour of PETE-S films for OECT transistor channels. SEM images recorded at 2 kV of PETE-S films polymerised by a drain voltage of 0.50 V applied to the top electrode in each image for a) 2 s, b) 30 s, c) 60 s, d) 120 s. Nucleation of the polymer film starts on top of the drain electrode (white arrows). The polymer film extends laterally (red arrows) from the drain with time. The source electrode (black arrow) was kept grounded. No polymer film growth is found on the source electrode. The insets on the left show the morphology on top of the drain electrode and source electrode at a higher magnification.	58
4.2	Area covered by the PETE-S film. a) Relative film area as a function of time. The relative areas in the graph are the ratio between the areas covered by the polymer film and the area of the drain electrode. At time zero there is no film growth yet. The area covered by the polymer film for each time was calculated from the SEM images on the right. b)-e) SEM images recorded at 1kV of PETE-S film at b) 2 s, c) 30 s, d) 60 s, e) 120 s. Each image shows a 1600 μm x 1100 μm region containing the source electrode (black arrows), drain electrode with grown polymer film (red arrows) and surrounding substrate (blue arrows).	59

- 4.3 Time evolution of the PETE-S film in the OECT transistor channel. SEM images at 1 kV showing the surface morphology of the film in the gap between the two electrodes. The images show the film after a) 2 s, b) 30 s, c) 60 s, and d) 120 s. The approximate position of the drain edge is marked by the dashed line in each image. The source electrode is grounded. Two distinct surface morphologies can be observed: a smooth surface in the upper half of the film by the drain electrode and a rough surface in the lower half of the film, closer to the source electrode. Areas of bright contrast (white arrows) in the rough part of the film originate from clusters of particles at or near the film surface. 60
- 4.4 Electrical characterisation of OECT devices. Measured drain current, I_D , as a function of time during device fabrication. In the graphs, a drain voltage $V_D = 0.50$ V is applied for a total time of a) 2 s, b) 30 s, c) 60 s and d) 120 s. This was followed by $V_D = 0$ V until the current stabilised. The drain current starts to increase significantly after approximately 4-7 s, marked by red arrows. This indicates the point where the conducting polymer film makes electrical contact with the grounded electrode. Triplicates of each sample were fabricated to investigate the reproducibility. 62
- 4.5 Percentage increase of drain current and polymer area as a function of time. The percentages are calculated relative to the values at the time 2 s. The mean (blue line) and standard deviation (shaded area) of the drain current measured for three devices are shown. The drain current increases much more rapidly than the area covered by the polymer film. 63
- 4.6 Cross sectional view of the polymer film grown for 30 s. a) SEM image recorded at 1 kV showing a FIB cross section. The thin, dark layer in the middle of the image is the polymer film. The film thickness varies along the length of the gap. The average film thickness is estimated to be 80 nm and the maximum thickness is measured as 210 nm in the gap region. The edge of the ground electrode (left arrow), positive electrode edge (right arrow), and approximate position of the threshold line (middle arrow) where the surface morphology starts to show a significant increase in roughness are all marked. b) Higher magnification image of the polymer film by the source electrode edge. c) Schematic illustration of the different regions of the FIB cross section (not to scale) identifiable by changes in contrast in the SEM image. d) Schematic showing the placement of the cross section in the OECT device. 64

-
- 4.7 AFM images of the PETE-S channels grown for a) 2, b) 30, c) 60, and d) 120 s. The images show height information. The scan size is $55\text{ }\mu\text{m} \times 40\text{ }\mu\text{m}$. The gap region is marked between the two dashed lines at the electrode edges. The height of the source electrode (furthest left part in each image) is set to 0 nm through data levelling by mean plane subtraction on the electrode and setting the plane to zero. The same colour scale bar is applied to all images except a). 65
- 4.8 Average sample height measured by AFM as a function of distance from the edge of the source electrode for OECT channels at four different times. Large variations in polymer film thickness are found in the gap region between the electrodes, highlighted in yellow. The zero-level is set at the height of the SiO_2 substrate. The edges of the source and drain electrodes are marked with dashed lines. The threshold line marks the position where the surface morphology changes from smooth to rough, similarly to Figure 4.10. 66
- 4.9 RMS roughness determined by AFM as a function of time and location. The mean value of the surface roughness are displayed for the source electrode, the polymer film in the smooth and rough part of the gap region and the polymer film on the drain electrode. The error bars represent the standard deviation of the value. 67
- 4.10 Surface morphology in different parts of the PETE-S channel. SEM images at 1kV of the PETE-S channel grown between source and drain electrodes for 30 s. The inset images to the right show different regions of the polymer film at a higher magnification. Dashed lines mark the position of the drain edge and the approximate distance from the drain electrode where the film morphology starts to change. White arrows point to fibrous structures within the clusters of material in the film. 69
- 4.11 Higher magnification images of the PETE-S film after 2 s of polymerising bias. SEM images recorded at 1 kV of the leading edge of the polymer film. The polymer film consists of two parts: a smooth film growing in direct contact with the substrate (white arrow) and a more course film on top (red arrow). b) shows a higher magnification image of the course film in the dashed region in Figure a). 70

4.12	Morphology of ETE monomer clusters. Top row: Bright field LPTEM images recorded at 300 kV. Bottom row: SEM secondary electron (SE) images recorded at 1 kV of the same solutions after drying. a) and d) 5 mM ETE-S 100%, b) and e) 5 mM ETE-S:PC 50:50 and c) and f) 5 mM ETE-PC 100% in DI water with 10 mM NaCl. The dark features in the LPTEM images and bright features in the SEM images correspond to monomers aggregated into clusters (arrowed), which are present in all three solutions. Red arrows in figure a) and d) mark ETE-S platelet clusters which are seen edge-on. Blue arrows mark platelet clusters that are more parallel to the substrate.	72
4.13	Overview of cluster distributions. SEM SE images recorded at 1 kV taken at a low magnification of dried solutions of DI water with 0.01 M NaCl and 5mM a) ETE-S 100%, b) ETE-S:PC 50:50 mix and c) ETE-PC 100%.	72
4.14	Cyclic voltammograms showing the oxidation peak in the first part of the anodic trace in the first scan cycle for the three monomer solutions. The position and shape of the oxidation peak is different for all three samples. The ETE-S:PC 50:50 sample shows evidence of two separate oxidation peaks (black arrows). Scan rate: 0.1 V s^{-1} . The working electrode, counter electrode and reference electrode are all Pt.	74
4.15	Surface morphology of freeze-dried hydrogels. SEM SE images at 1 kV of hydrogel samples showing the morphology of a) Gel sample, b) 5 mg/ml PETE-S Gel sample, c) 10 mg/ml PETE-S Gel sample, and d) 20 mg/ml PETE-S Gel sample. The structure consists of pores separated by walls. The walls become more continuous as the PETE-S concentration increases.	77
4.16	Higher magnification images of surface structures in freeze-dried hydrogels. SEM SE images at 1 kV of hydrogel samples showing a) the web-like network of the HA-BCN/PEG hydrogel acting as scaffolding for the 10 mg/ml PETE-S polymer and b) the rough surface texture of a 20 mg/ml PETE-S Gel sample.	78
4.17	Illustration of how the internal structure of a hydrogel sample is revealed. A focused ion beam is used to mill away material from the bulk hydrogel sample which exposes a cross-section inside the hydrogel.	79

- 4.18 Internal structure of freeze-dried hydrogels. SEM SE images at 1 kV of cross-sectioned freeze-dried hydrogel samples showing the internal microstructure of a) Gel sample, b) 5 mg/ml PETE-S Gel sample, c) 10 mg/ml PETE-S Gel sample, and d) 20 mg/ml PETE-S Gel sample. The images show the pore structure within the bulk materials. The wall thickness of the pores increases as the amount of PETE-S increases. The walls become more continuous with increasing distance from the sample surface (top part of the images) when PETE-S is incorporated in the hydrogel. 80

List of Abbreviations

Biological systems

BBB	Blood brain barrier
CNS	Central nervous system
ECM	Extracellular matrix

Experimental techniques

AFM	Atomic force microscopy
BF	Bright-field
BSE	Backscattered electron
CCD	Charge-coupled device
CV	Cyclic voltammetry
DF	Dark-field
DLS	Dynamic light scattering
DP	Diffraction pattern
E-T	Everhart-Thornley
EDX	Energy dispersive X-ray spectroscopy
EELS	Electron energy-loss spectroscopy
ESEM	Environmental scanning electron microscopy
ETEM	Environmental transmission electron microscopy
FIB-SEM	..	Focused ion beam scanning electron microscopy
GIS	Gas injection system
LMIS	Liquid metal ion source
LPTEM	Liquid phase transmission electron microscopy
SE	Secondary electron
SEM	Scanning electron microscopy
STEM	Scanning transmission electron microscopy
TEM	Transmission electron microscopy
VPSEM	Variable pressure scanning electron microscopy

Materials

APTES	(3-amino-propyl) triethoxysilane
BCN	Bicyclo[6.1.0]non-4-yne
DI	Deionised
ETE	(2,5-bis(2,3-dihydrothieno[3,4-b][1,4]dioxin-5-yl)thiophene
ETE-PC	...	ETE functionalised with a phosphocoline side chain
ETE-S	ETE functionalised with a ethoxy-1-butanesulfonic acid side chain

HA	Hyaluronic acid
HRP	Horseradish peroxidase
PBS	Phosphate buffered saline
PEDOT	Poly(3,4-ethylenedioxythiophene)
PEG-Az4	..	4-arm polyethylene glycol with terminal azides
PSS	Polystyrene sulfonate

Organic electronics and other devices

DBS	Deep brain stimulation
EOECT	Evolvable organic electrochemical transistor
HOMO	Highest occupied molecular orbit
LUMO	Lowest unoccupied molecular orbit
MEMS	Micro-electromechanical system
MOSFET	..	Metal-oxide-semiconductor field-effect transistor
OECT	Organic electrochemical transistor
OFET	Organic field-effect transistor

1 Introduction

1.1 Background

Neurodegenerative diseases are a large group of diseases that pose great challenges to healthcare and can have severe effects on the life quality of the affected. Examples of diseases included in this group are Alzheimer's disease, Parkinson's disease, and amyotrophic lateral sclerosis (ALS). Neurodegenerative diseases typically have complex origins and are characterised by a disruption and degeneration of the central nervous system (CNS), consisting of the brain and the spinal cord. This degeneration typically involves the loss of function and eventually the death of neurons. This is often displayed as a disruption of electrical signals in the CNS. Oxidative stress, protein aggregation, and depletion of neurotransmitters have been identified as some of the main causes of cell deterioration and loss of cell connectivity associated with this group of diseases. [1,2]

Signalling in the CNS relies on information transmission between neurons through biochemical or electrical processes in synapses. Treatment methods have been developed for symptom suppression and palliative care, but no cure has yet been found for neurodegenerative diseases. Current therapeutics mainly focus on altering the biochemical processes in the CNS by drug administration. The drugs are typically designed to introduce antioxidants, control the amount of neurotransmitters, or mitigate the formation of amyloid fibrils. [1,2] These drugs are not always effective and often involve many unwanted side effects. Electrical therapies also exist. Among these, the most common treatment method is deep brain stimulation (DBS). This is an invasive electronics-based surgical procedure, where metal electrodes are implanted into certain areas of the brain to control abnormal brain activity via electrical impulses. [3] Although this method can be used for multiple neurological disorders, it carries substantial risks. These risks include stroke and infection related to open-skull surgery, accumulation of scar tissue, and low biocompatibility of the electrode material. Moreover, one of the major problems with this technique is that the electrodes are relatively large and rigid. The size of the electrodes limits the minimum volume of brain tissue that can be contacted to target individual neurons or bundles of neurons. The mechanical properties of the rigid electrodes also restrict them from fully integrating with the tissue and moving

with the surrounding material, which may cause damage to nearby tissue. [4]

An alternative approach to DBS is implementing electronic neuro-pharmaceuticals, which leverage the benefits of current electrical therapeutics for neurodegenerative diseases while minimising the adverse effects. The e-NeuroPharma project aims to develop organic electronics based on injectable small molecule precursors of conducting polymers. The monomer precursors can be *in vivo* polymerised directly in the brain to create functional electronic devices in a minimally invasive manner. By using self-assembled nanotechnology to manufacture these devices, they can target individual cells as opposed to large bundles of neurons responsible for many different physiological and cognitive processes. Organic electronic materials are promising to create interfaces between technology and biology thanks to their ability to transduce both ionic and electronic signals, their tissue-like mechanical properties, and their high biocompatibility. [5] In recent years, several research groups have utilised conducting polymer-based materials for *in vivo* formation of "soft" biocompatible electrodes in cells and tissue. Their work has led to the development of polymer-coated cell cultures for neural stimulation [6], neural prosthetics [7], conducting wire electrodes inside the vasculature of plants [8], and *in vivo* assembly of bioelectronics inside hydras [9] and zebrafish [10, 11].

Within e-NeuroPharma, organic electrochemical transistors (OECTs) with transistor channels grown from electropolymerised monomer solutions have been developed as a model system for neuromorphic devices and synthetic synaptic connections. [12–14] It has been shown that the surface chemistry of the substrate and the electric potential applied to the system govern film formation in these devices. [14] However, knowledge about the micro- and nanostructure of these devices and their effect on device properties is very limited. Conducting hydrogels have also been devised for local nerve stimulation [10], and to create three-dimensional scaffolding in cell cultures and bioink in tissue engineering [15]. The microstructure of such hydrogels has a large influence on the mechanical, electrical, and biocompatible properties of the system and should be investigated when optimising or developing new hydrogel systems.

Many of the materials and devices that have been established for organic electronics rely on the polymerisation of thiophene-based monomers in electrolyte solutions. Recent studies have shown that these monomers are not always fully dispersed but may form large aggregates in solution. [16] The size distribution of such monomer aggregates determines whether they can enter cells or pass the blood-brain barrier (BBB) to enter the CNS. The size of the aggregates is thus important to consider for a device designed to assemble in the brain. Aggregation also affects the formation of desired conducting pathways by altering the morphology of polymer films grown from these solutions. Understanding the agglomeration, nucleation,

and subsequent film evolution from monomers in solution is therefore essential to predict the physical and electrical properties of the pharmaceuticals and their function in the human body.

1.2 Scope of the Thesis

In this thesis, the micro- and nanostructure of materials and devices for electronic neuro-pharmaceuticals are investigated and correlated to important device properties. The structural characterisation is mostly carried out using electron microscopy techniques with high spatial resolution. This is complemented by other methods to analyse the surface topography, electrical and mechanical properties as well as biocompatibility of devices. This thesis aims to contribute to a better understanding of the material structures and how they can be tuned for functional bioelectronics.

2 Organic Electronics Used for Treatment of Neurodegenerative Diseases

Organic electronic materials implement conducting and semiconducting polymers and small molecules to attain both electronic and ionic conductivity. This unique combination makes organic electronics excellent for interfacing biological systems with electronics. [5] This thesis is focused on applying organic electronics to develop materials, devices and electronic systems that can be *in vivo* manufactured in tissue to target diseases affecting the neuronal system. This chapter presents background information about the materials used in organic electronics as well as information about some important device applications.

2.1 Conducting Polymers

2.1.1 The Building Blocks of Polymers

Polymers are a class of materials made up of very large molecules (macromolecules) comprised of a large amount of repeating structural units called monomers. The monomers are typically joined together by covalent bonds to form a polymer chain during a polymerisation reaction.

The polymer chain is often divided into the backbone and the side groups. These are shown for the polymer PEDOT-S [alkoxysulfonate-functionalised poly(3,4-ethylenedioxythiophene)] in Figure 2.1a). [8] Polymers are normally classified based on the characteristics of the backbone, which forms the main chain and determines many of the properties of the polymer such as the mechanical flexibility. The side chains can be modified to further functionalise the polymer and e.g. increase the solubility and processability. [17] Dopant ions can also be added to alter the mechanical, electrical and optical properties of the polymer. [18,19]

The molecular weight of a polymer is related to the average number of repeating monomer units in the polymer chain, also known as the degree of polymerisation.

Polymers consisting of the same base monomers may have different molecular weights, resulting in different properties. Short-chain polymers are also called oligomers. This group may be further divided into dimers, trimers, tetramers etc. for a chain with two, three or four monomer units.

The two most common polymerisation mechanisms are step-growth (condensation) and chain-growth (addition). Step-growth polymerisation is typically a succession of condensation reactions where a small molecule (often H_2O) is lost in each reaction. In chain-growth polymerisation, a catalyst such as a free radical or ionic initiator is often used to open the C-C double bonds of a monomer so that it can react with other monomers and form a growing polymer chain. [17]

2.1.2 Electronic Properties of Conducting Polymers

Polymers were long considered to only be insulators before the development of intrinsically conducting polymers. This new class of organic materials, often referred to as organic semiconductors, is now recognised as having similar electrical and optical properties as inorganic semiconductors and metals. Conducting polymers are normally conjugated molecules with sp^2 -hybridisation, where the polymer chain is bound by both saturated σ bonds and unsaturated π bonds. The optical and electrical properties of conjugated polymers come from the alternating single and double bonds which lead to overlap of the p-orbitals, giving rise to delocalised π electrons with high mobility between neighbouring atoms in the molecule. [20] Because the π bonds have small ionisation potentials, π electrons can relatively easily be removed or added to the polymer molecule without disrupting the σ bonds that give stability to the polymer. [21]

Conducting polymers and other organic semiconductors, just like their inorganic counterparts, exhibit a separation in energy between their highest occupied molecular orbital (HOMO) and their lowest unoccupied molecular orbital (LUMO). The band gap is the energy difference between HOMO and LUMO and can be tuned to a chosen level to allow the material to act as an insulator or conductor (assuming enough external energy is added to the system to allow the electrons to be excited across the energy gap). If an electron overcomes the energy gap, a positively charged quasi-particle called a hole is created in the electron's original state. The material can be designed to either preferentially use holes or electrons as charge carriers and is then commonly referred to as p-type (hole transporter) or n-type (electron transporter). [22] By oxidising or reducing the polymer backbone, depending on if the polymer is p-type or n-type, mobile charges are introduced in a process known as doping. It is often energetically favourable to spatially localise the charge in the polymer chain by distorting the lattice around the charge.

This shifts the HOMO energy upwards and the LOMO energy downwards, lowering the ionisation energy of the polymer. If the decrease in ionisation energy is larger than the energy needed for the distortion, charge localisation occurs and a so-called polaron is created. A polaron is a quasiparticle that describes the interactions between a spatially confined charge and the atoms in the lattice around it. Polarons are commonly found as charge carriers in many conducting polymers and may diffuse through the lattice. However, since they require charges to be spatially confined, they do not have the same mobility as free charges. [21]

A common way to increase the electrical conductivity of organic semiconductors is increasing the number of charge carriers in the polymer backbone by doping. Doping of organic semiconductors is performed by exposing the polymer to oxidising or reducing agents. A common doping method is to add dopant ions or molecules that react with the polymer to create charges in the polymer backbone. [23] Another approach is utilising self-doping, where the doping ions are covalently bound to the polymer backbone, acting as counterions to the charge on the backbone and making the polymer intrinsically conductive. [24] An example of a p-type self-doped polymer is PEDOT-S [8] shown in Figure 2.1a). In PEDOT-S, the sulfonate ion on the side chain acts as a counterion to the positively charged polaron induced in the polymer backbone, making the whole molecule charge neutral. Undoped polymers normally have electrical conductivities as low as $10^{-10} \text{ S cm}^{-1}$ or $10^{-6} \text{ S cm}^{-1}$. [25] Doping the polymer can increase the conductivity by several orders of magnitude to around $10^2 - 10^3 \text{ S cm}^{-1}$. [26, 27]

2.1.3 Charge Transport in Conducting Polymers

Efficient charge transport in conducting polymers and other organic semiconductors relies on the density of charge carriers, molecular ordering, molecular size and weight, impurities, the presence of electric fields, pressure and temperature. [22] Many polymers do not display any ordered structure because of the weak intramolecular van der Waals forces between the polymer chains. Instead, the individual polymer chains are often randomly oriented within the material making them amorphous. However, the π -orbitals in conjugated polymers may overlap between neighboring polymer chains. Because of this, conjugated polymers often tend to have so-called π - π stacking orthogonal to the conjugation direction (see Figure 2.1b)), giving rise to a more ordered structure. Cross-linking of polymer chains also increases the degree of order in the polymer. The formation of ordered domains existing at length scales ranging from atomic to microscopic or even mesoscopic levels typically occurs through molecule self-assembly but can also be induced e.g. by straining the material to align the polymer chains in a preferred direction during polymer film fabrication. [28, 29]

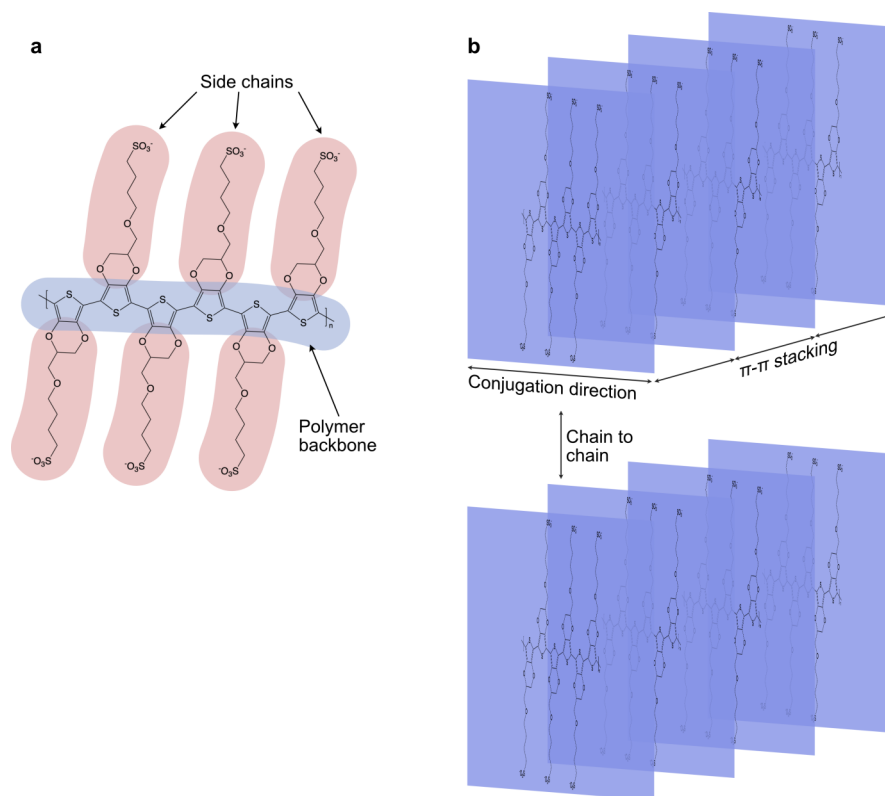


Figure 2.1: Illustration of a) the chemical structure of the conjugated polymer PEDOT-S, here shown with six repeating monomer units, and b) ordering in conjugated polymers due to π - π stacking.

The charge transport in conducting polymers is in the form of slow phonon-assisted hopping along percolative paths between carbon atoms in the material system. These paths occur along the polymer chain backbone or between adjacent π - π stacked chains. Transport of charge carriers along these paths is mainly dependent on the length of the polymer chains and the π - π stacking distance. [28–30] Transport along the polymer chain backbone is usually quickest since it only involves movement between delocalised π -orbitals extending along the same polymer chain. Chemical or physical defects along the chain can interrupt charge transport along this path. Charge transport along the π - π stacking direction is theoretically lower than along the backbone but still accounts for a large portion of charge transport in conjugated polymers. It is also possible to transfer charge carriers between polymer chains in the direction of the side chains shown in Figure 2.1b). Transport along this interchain direction is much more difficult though since the side chains may act as an insulating layer and the distance between chains can be large. [29]

2.1.4 Conducting Polymers in Organic Electronics

Conducting polymers are essential in the development of organic electronics. The high electrical conductivity achievable, high mechanical flexibility, biocompatibility and the potential of *in vivo* manufacturing through self-organisation in living tissue make conducting polymers very attractive in biological applications. Conducting polymers are today used extensively in biomedical fields such as bioengineering, regenerative medicine and biosensors. [20] The possibility to fabricate conducting polymer films from solution makes this group of materials especially useful for bioelectronics. It can however be challenging to control the resulting film morphology and molecular structure. Many factors affect the nano- and microstructure of polymer films such as the chemistry of the solvent used, the solubility of the monomers, properties of the substrate and environmental conditions. [29] The nanostructure, in turn, strongly affects the electrical conductivity of the material since it governs the formation of percolative paths discussed in the previous section.

2.2 Organic Electronics

The field of organic electronics emerged in the 1980's through the use of organic semiconductors to develop devices such as organic transistors, organic light-emitting diodes, and later on also organic solar cells. This thesis focuses on organic electronics which are used as interfaces to translate signals and functions between biological systems and electronic devices. Such organic electronics, often termed "organic bioelectronics" [31], can be used to modify the physiology and processes of everything from individual cells to entire organs. They can also be used as sensors that monitor different signals coming from the biological system because of their ability to conduct and process both electronic and ionic signals. Furthermore, since the conducting polymers or molecules in organic electronics are mostly developed via synthetic strategies, their physical and chemical properties can be tuned so the resulting device fits the requirements on mechanical flexibility, elasticity, morphology, conductivity, or surface chemistry set by the biological system in question. [5] Implementing organic electronics capable of communicating with neural cells and tissue can thus help us improve our understanding of complex biological functions and treat various neurodegenerative diseases.

2.2.1 Characteristics of Organic Electronics

When compared to inorganic electronics, such as silicon-based devices, organic electronics have certain characteristics that are especially useful in biological ap-

plications. A solvated ion in an electrolyte in a biological system is often relatively large compared to the network of covalently bound atoms in silicon. Conducting polymers and other organic semiconductors, on the other hand, are made up of macromolecular blocks held together by weak van der Waals forces or electrostatic interactions. The weak forces holding the molecules in organic semiconductors together make the space between molecules relatively large, which allows for efficient transport of ions through the material. The reliance on van der Waals interactions is also the reason why many organic materials are considered "soft" compared to their hard inorganic counterparts. [32] In contrast to the weak van der Waals interactions between polymer chains, organic semiconductors sometimes also implement cross-linked polymers, where the polymer chains are connected to each other by covalent or ionic bonds. Such cross-linking typically leads to an increase in the rigidity and mechanical strength of the material which can be tuned to fit the desired properties of the final device. [17] Furthermore, the opportunities for chemical modification are more easily available for organic materials compared to inorganic ones. Both the conjugated backbone and the side chains of the polymer can be altered to change the material properties. The polymers can be arranged to form anything from single-crystalline structures to amorphous structures of a single polymer species or a composite simply using a few fundamental monomer building blocks. Another important characteristic of many organic electronic materials is that their interfaces do not get covered by an oxide layer as easily as silicon-based electronics when contacted by e.g. aqueous electrolytes. This facilitates their use in bioelectronic interfaces. [32]

2.2.2 Signalling in Biological Systems

Typical signals in biological systems can be both electronic, ionic and molecular in nature. Signals can be carried by molecules ranging in size from small cations, such as Ca_2^+ with a radius of about 100 pm, to macromolecules such as proteins which can be up to a few nanometres in size. [5, 33] So-called action potentials carry the electrical signals containing information within neurons. The action potential in a biological neuron is triggered when the membrane potential is changed by a stimulus to reach above a threshold potential. The threshold is generally between -50 mV and -55 mV. The action potential triggers the release of neurotransmitters (small molecules) from the presynaptic nerve terminal to the postsynaptic terminal. At the postsynaptic terminal, the neurotransmitters bind to receptors which control the flow of cations such as Ca_2^+ across the cell membrane. This triggers a new electric signal in the form of an action potential that continues propagating in the nervous system. [34] The described neuronal signalling highlights the intricate interactions taking place between electrical stimuli, ions, neurotransmit-

ters, proteins and DNA in many biological systems. The ability to record or alter such signals is essential for translating information between biology and technology. In order to do so, the utilised electronics need to have high biocompatibility and be stable in common biological environments for long time periods. In many situations it is also favourable to have a minimally invasive device with geometry and mechanical properties that match those of the biological system. [5]

2.2.3 Electronic and Ionic Conductivity

In addition to the signal translation capabilities that come with the intrinsic electronic conductivity of conducting polymers described in Section 2.1, polymeric materials also offer a unique platform for ion migration through a solid given that the pore size and molecular dynamics of the material allows it. [5] Gel polymer electrolytes contain a large amount of liquid electrolyte solutions (often water-based) inside a polymer scaffold where ion conduction can occur throughout the bulk solid by the dissociation of electrolyte components. [35] Polyelectrolytes consist of ionisable polymers that both act as scaffolding medium and can dissociate into charged polymers and counterions which move in the presence of electric fields. Polyelectrolytes form either polycations or polyanions depending on the charge of the polymer and associated counterion [36]. They can be used in electrochemical devices or bipolar membranes for sensing charged biomolecules or in biomimetic devices where the polyelectrolyte counterion represents a relevant biological signal (e.g. a biological cation such as Ca_2^+ or Na^+). Perhaps the most commonly used device structure for organic electronics consists of a thin organic film, often made from a conducting polymer, in contact with one or more electrodes. The injection of electrons, holes or even ions into the polymer leads to charge transport in the film. [5]

2.2.4 Bioelectronic Interfaces with Cells

It has recently been shown that cells "feel" their environment and are affected by the mechanical, physical and chemical properties of their surroundings. In cell cultures, many cells are not viable upon suspension in a fluid but need to adhere to a solid. [37,38] In living cells, this adhesion is performed by receptors on the cell membrane that connect with extracellular proteins in the surroundings. [39] The ability for such proteins to organise on a cell culture surface depends on the hydrophobicity, surface chemistry and surface energy of the substrate, which in turn then affect the cell adhesion. [40] The cells also respond differently when grown in a stiff or soft matrix and ideally the stiffness of the two-dimensional substrate or three-dimensional scaffolding should match that of the natural environment

for the cells. Processes such as cell contraction, proliferation, organisation, and cell death are all dependent on the elasticity of the surrounding matrix. Tissue cells such as neurons, fibroblasts, myocytes, and osteocytes come from different microenvironments with varying elasticity. Brain tissue is amongst the softest, with elasticity of about 0.2-1 kPa, muscle tissue exhibits intermediate stiffness, and osteoid tissue found in bones is among the stiffest, with elasticities of 25-45 kPa. [37,38] Conducting polymer films and matrices can often be made softer and with a more pronounced three-dimensional structure than many metal or inorganic interfaces. They are therefore considered to be more biocompatible, giving them an advantage in the field of bioelectronics. [5] Conjugated polymers such as polyaniline (PANI), polypyrrole (PPy), polythiophene (PTh) and poly(3,4-ethylenedioxythiophene) (PEDOT) have been widely used in organic electronics, particularly those intended for neural devices and tissue engineering because of their high biocompatibility and electron-ion conductivity. [5,19,41] Moreover, some organic electronic devices made from conducting polymer films are deemed "evolvable", meaning that they can change mechanical or physiochemical properties as a response to some stimuli. This is of particular importance for the development of neural interfaces or neuromorphic devices since the brain exhibits a natural neural plasticity. [5,12,13]

Today, organic bioelectronics are used to create an ever growing collection of material systems and devices. They are used in applications ranging from conducting polymer electrodes to bioactive surfaces and three-dimensional scaffolds for cell cultures, to organic field-effect transistors (OFETs) and organic electrochemical transistors (OECTs) for biosensors and neural interfaces, ion pumps for drug delivery and even electronic skin. [5] In the following sections, OECT devices and three-dimensional scaffolds comprised of conducting hydrogels will be explained in more detail.

2.3 Organic Electrochemical Transistors (OECTs)

Since their invention in 1947, transistors made of semiconductors, dielectrics and metals allow the flow of electrons in a solid-state device to be controlled. Modern transistors typically rely on field-effect doping, where the number of charge carriers in a semiconductor is adjusted by applying a voltage to a metal electrode. The electrode is separated from the semiconductor by a thin insulating layer called the gate dielectric. These devices are known as MOSFETs (metal-oxide semiconductor field-effect transistors) and are the most widely used type of transistor. [42] An increased interest in the use of organic electronics led to the development of OFETs. OECTs were later developed by the group of Mark Wrighton in the mid-1980s. [43]

The typical structure of an OECT is shown in Figure 2.2. These devices consist of an organic semiconductor film (the transistor channel) that is in contact with an electrolyte. A gate electrode is immersed in the electrolyte. Metal electrodes called source and drain are in contact with the organic semiconductor film and together they define the channel through which holes or electrons flow (depending on the charge carriers) between the source and the drain terminal.

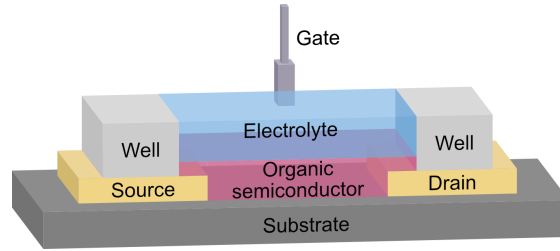


Figure 2.2: The typical structure of an organic electrochemical transistor showing the source, drain and gate electrodes with an organic semiconductor film in contact with an electrolyte.

Applications of OECTs

OECTs are especially attractive for use in medical diagnostics and bioelectronic implants since they have higher biological and mechanical compatibility with cells and tissue compared to traditional electronics relying on inorganic materials. The mechanical flexibility of the organic semiconductor transistor channel in OECTs is especially suitable for the nonplanar form factors typically required for implants. [31, 44, 45] OECTs have a wide range of applications, including chemical and biological sensors [46], controlling cell adhesion [47], measuring the cell activity in electrically active tissue [48], stimulating neurons locally [49], and in neuromorphic devices that can mimic the structure and function of the nervous system [12, 50, 51].

2.3.1 Structure, Physics and Electronic Properties of OECTs

OECTs rely on ion injection from the electrolyte into the semiconductor film to change the doping state of the organic semiconductor and thus also its conductivity. [52] The rate of ion injection is controlled by applying a voltage to the gate terminal. By applying a voltage to the drain electrode, a drain current, I_D , is induced in the semiconductor channel with amplitude proportional to the number of mobile charge carriers in the film. Both the gate voltage, V_G , and drain voltage, V_D , are defined with respect to the source electrode which is often grounded. [44]

Similar to both MOSFETs and OFETs, OECTs operate in a switch-like manner where the gate voltage controls the drain current by changing the level of doping in the organic semiconductor film. [48] When no gate voltage is applied, I_D is determined by the intrinsic conductance of the organic semiconductor channel. When a gate voltage is applied, I_D depends on the extent of doping. Much of the physics of OECTs can be described by the Bernards model. The model divides the OECT device into an electronic circuit and an ionic circuit. The electronic circuit is described by Ohm's law and consists of the organic semiconductor film where the electronic charge transport depends on the density and mobility of charge carriers. Electronic charges drift in response to the local potential. The ionic circuit consists of a resistor, which describes ionic charge transport in the electrolyte. It is assumed that reactions in the ionic circuit only occur at the electrolyte-semiconductor interface. No reactions occur at the gate electrode. Furthermore, devices are assumed to be governed by non-Faradaic processes, meaning that charge-transfer reactions do not take place in the electrodes or in the organic semiconductor. Instead, ionic charges accumulate at electrode surfaces, resulting in charging and discharging of an ionic double-layer. Ions can also be stored in the channel material to electrostatically compensate opposite charges present in the film via capacitive processes. [52]

OECTs typically operate in either accumulation mode or depletion mode. Accumulation mode devices generally have a low number of intrinsic charge carriers in the organic semiconductor channel. By applying a negative or positive gate voltage, anions or cations are transported into the channel and increase the number of holes or electrons, respectively, which increases the electronic conductivity. For depletion-mode devices, the number of intrinsic charge carriers is in general high and a high drain current can flow even at zero gate voltage. As the gate voltage becomes increasingly positive or negative, ions are injected into the channel and compensate the doping ions of the organic semiconductor. This leads to a de-doping of the material, which decreases the number of charge carriers. [44] The majority of published works is on depletion-mode OECTs. [52]

An important characteristic of OECTs is that changes in doping state occur throughout the entire bulk volume of the channel, not just the top surface layers (as in FETs) where a double layer of accumulated ions can be created. This means that low-gate voltages can lead to large changes in the drain current, making OECTs efficient switches and useful signal amplifiers in e.g. glucose sensors. [45]

The relationship between the drain current and gate voltage is described by a transfer curve. The slope of the transfer curve is known as the transconductance, g_m , an important performance metric for transistors. A steeper transfer curve indicates a larger change in drain current for a given gate voltage. [44] The transconductance

of an OECT device can be predicted by the Bernards model as

$$g_m = \frac{W}{L} \cdot d \cdot \mu \cdot C^* \cdot (V_T - V_G) \quad (2.1)$$

for devices operating in depletion mode and

$$g_m = \frac{W}{L} \cdot d \cdot \mu \cdot C^* \cdot (V_G - V_T) \quad (2.2)$$

for devices operating in accumulation mode where W , L and d are the width, length and thickness of the channel, respectively, μ is the mobility of the charge carriers, C^* is the channel capacitance per unit volume and V_T is a threshold voltage that does not depend on the geometry of the channel. [53] This model shows that the transconductance scales not only with the width and length of the channel, but also with the channel thickness. Moreover, there are indications that the volumetric capacitance, C^* , depends on the structure of the material in the channel. [53] The hydration of the channel material is important since it describes the ability to take up water and swell, yielding a loosely packed structure that facilitates ion transport. [54] On the other hand, electronic charge transport in the channel can also be improved by the presence of crystallites or dense polymer aggregates with good intergrain connectivity because of the strong $\pi - \pi$ interactions in such structures. [55]

2.3.2 Materials in OECTs

The transistor channel often consists of a conducting polymer, typically PPy or PEDOT doped with small anions or polyanions. In the case of PEDOT, the most commonly used dopant is poly(styrene sulfonate) (PSS) which makes PEDOT:PSS a doped p-type semiconductor operating in the depletion mode. [44, 45] In PEDOT:PSS, holes generated in the conjugated polymer backbone are compensated by the negatively charged PSS ions. By applying a positive gate voltage, V_G , cations from the electrolyte are injected into the organic semiconductor channel and compensate the charge on the PSS ions. This decreases the hole density in the PEDOT backbone, reducing the number of charge carriers in the conducting polymer and lowering the drain current. Similarly, a negative gate voltage can be applied to inject anions instead. In this manner, OECTs can be used to convert ionic currents common in biological systems to electronic currents. [56] It has been shown that using the right processing methods, the electronic conductivity of PEDOT:PSS thin films can reach values higher than 1000 S cm^{-1} . [57]

The conducting polymers used for OECTs are commonly synthesised via solution, vapour-phase or electrochemical polymerisation allowing for facile deposition of thin films. Vapour-phase polymerisation is often chosen over electropolymerisation since the latter requires a conducting surface for the initiation of film growth which can be difficult to implement. Vapour-phase polymerisation only requires the device substrate to be coated with an oxidant that polymerises monomers introduced in vapour form. [44] However, the most common deposition methods rely on solvent-based techniques such as spin-coating or printing with polymer inks. Such techniques are considered low-cost and allow for fast deposition of thin films. Spin-coating has been extensively used for fabrication of OECT channels and involves drop casting a polymer solution on a rotating substrate. The thickness and morphology of the final film depends on the properties of the solution (such as volatility, concentration and viscosity), the wettability and cleanliness of the substrate, and the spinning speed and time. [58]

Pre-patterned Au electrodes on a glass or SiO₂ substrate are commonly used for the source and drain electrodes. For the gate electrode, a non-polarisable material such as Ag/AgCl is typically used, but a polarisable electrode (such as Pt) can also be implemented. The electrolyte can be a liquid, gel or solid based on the intended application or fabrication limitations. Most commonly, aqueous solutions of NaCl or KCl are chosen as the electrolyte. [44]

2.4 Conducting Hydrogels for Cell Cultures and Neural Tissue Engineering

In living organisms, cells develop and act in complex three-dimensional environments that may be in the form of bone scaffolding, tissue, or the extracellular matrix (ECM). Hydrogels are three-dimensional porous, hydrophilic networks of cross-linked polymers that can hold large amounts of water (see illustration in Figure 2.3). [59] They can be made with similar mechanical and biochemical properties as different types of tissue, making them prime candidates for many medical devices. [60] Traditional hydrogels often display only low ionic conductivity and little to no electronic conductivity, leading to short signal conduction distances. This problem can be circumvented by incorporating electrically conducting polymers into the hydrogel. Conducting hydrogels are an invaluable tool for interfacing directly with electro-active cells or tissue since they can modulate cell responses like cell proliferation and differentiation. This makes conducting hydrogels attractive in applications such as scaffolding in *in vitro* cell cultures [60], neural probes and sensors, tissue engineering, artificial muscles, controlled drug delivery systems

and bioinks for 3D printing. [61, 62]

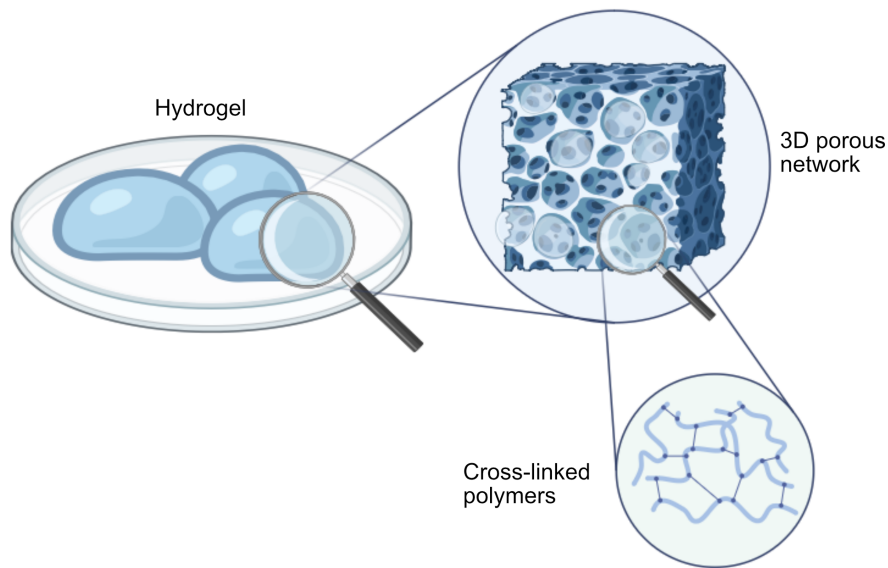


Figure 2.3: Illustration of a hydrogel consisting of a three-dimensional porous network of cross-linked polymers capable of holding large amounts of water. Image created with BioRender.com

2.4.1 The Importance of Porosity in Biological Scaffolding and Hydrogels

An important property of biological scaffolding, such as the ECM, is its porosity which plays a key role in the formation and function of the cells and tissue within it. For cells to distribute homogeneously throughout the ECM and connect, a significant amount of porosity is needed. [60] When designing artificial scaffolds such as hydrogels, it is important to replicate this porosity. The porous network of hydrogels in an implant increases the surface area that cells can adhere to which enhances tissue regeneration within the hydrogel matrix. [63] A system of interconnected pores also facilitates the diffusion of oxygen and nutrients to cells within the matrix, which is essential for cell proliferation, migration and survival. These functions are important to consider when developing hydrogel scaffolds as a representation of the ECM for neural tissue engineering. In addition to pore interconnectivity, the pore size also affects the growth and movement of cells within the hydrogel. Moreover, the pore size determines how well the hydrogel material can contract. The mechanical stiffness of the hydrogel typically decreases with increasing porosity. [60] When using hydrogel scaffolds in tissue

regeneration, the pore size should also be modified to match the type of tissue being treated. The optimum pore size can be as small as 5 μm for growth of new blood vessels but needs to be 100-350 μm for mammalian skin [60]. Brain neuronal tissue grows successfully in scaffolds with pore sizes around 100 μm , but neurons in the peripheral nervous system need pore lengths of 200-750 μm to grow their long axons. [64] Natural regeneration of neural tissue in the brain is limited, which is why treatment and not just symptom suppression of neurodegenerative diseases is so difficult to accomplish. Using conducting hydrogels as scaffolds to promote tissue regeneration and replacing defective cells is therefore of particular importance when treating neurodegenerative diseases. [64]

2.4.2 Materials in Conducting Hydrogels

A problem with many of the common conducting polymers is that they have poor water solubility, are non-degradable, are mechanically brittle because of rigid π -conjugation, or require aggressive polymerisation methods. This limits their use in bioelectronics. [65–67] A large majority of biomedical devices therefore use PEDOT:PSS which shows excellent chemical stability, electrical properties and biocompatibility. [61, 68] While PEDOT-based hydrogels show large potential for use in *in vitro* cell cultures with neural cells, its use in tissue engineering for *in vivo* applications is more limited due to difficulties in functionalising the polymer to make it biodegradable, increase the solubility and processability, and improve the biological response. [69, 70] PEDOT:PSS also has a considerably higher Young's modulus (on the order of 100 MPa [71]) than many types of biological tissue, such as mammalian brain tissue which has a Young's modulus on the order of 1 kPa [72], limiting its use for some bioelectronics. An alternative to using pre-polymerised conducting polymers in hydrogels for cell cultures or tissue engineering is to use water-soluble π -conjugated monomers that can be *in situ* polymerised within the hydrogel. Conducting polymers fabricated this way benefit from the improved solubility and processability, and offer more possibilities for material functionalisation while maintaining the electrical characteristics of pre-polymerised materials. [12–14] While polymers can exhibit a large variation in molecular size within the material due to the polymer chains all having slightly different lengths, pure monomers generally have a more defined size and structure. This enables more uniform interactions with cells and other materials. [73] Moreover, oligomers with up to ten monomer units have been shown to undergo material remodelling and degradation *in vivo* [70] and can be eliminated by macrophages - a type of white blood cell. [11] These functionalities are important to consider for *in vivo* applications such as treatment of diseases where removal of the bioelectronics with minimal tissue damage after disease relief is desired.

3 Experimental Techniques, Methods and Materials

This chapter describes the specific materials and devices studied in this thesis along with information about the experimental techniques implemented for the characterisation of the material microstructures. A description of the instruments that have been used in this thesis work and necessary sample preparation steps are also presented at the end of this chapter.

3.1 Material Systems

The majority of organic semiconductor materials studied in this thesis are based on a derivative of PEDOT formed by the conjugated monomer backbone 2,5-bis(2,3-dihydrothieno[3,4-b][1,4]dioxin-5-yl) thiophene (EDOT-thiophene-EDOT, abbreviated as ETE) which can be functionalised with different side chains on the central thiophene. The following sections describe the properties of these materials and their use in OECT devices and conducting hydrogels investigated in this thesis.

3.1.1 ETE-S and ETE-PC

ETE monomers are thiophene-based molecules comprised of two 3,4-ethylenedioxythiophene (EDOT) moieties on both sides of a thiophene ring modified with a functionalised side chain. For ETE-S, the central thiophene has a negatively charged 4-ethoxy-1-butanesulfonic acid side chain whereas for ETE-PC it is a zwitterionic phosphocoline side chain. The side chain acts as an intrinsic dopant for the monomer. [14] The chemical structures of ETE-S and ETE-PC are shown in Figure 3.1. The length of the thiophene backbone of a single monomer unit is approximately 10-11 Å. Protocols thoroughly describing the synthesis of ETE-S and ETE-PC can be found in the literature. [13, 14] Both ETE-S and ETE-PC are shown to have high biocompatibility and can form highly conducting polymers with electric conductivity on the order of 10 S cm^{-1} , making them suitable materials in many bioelectronic device applications. [8–11]

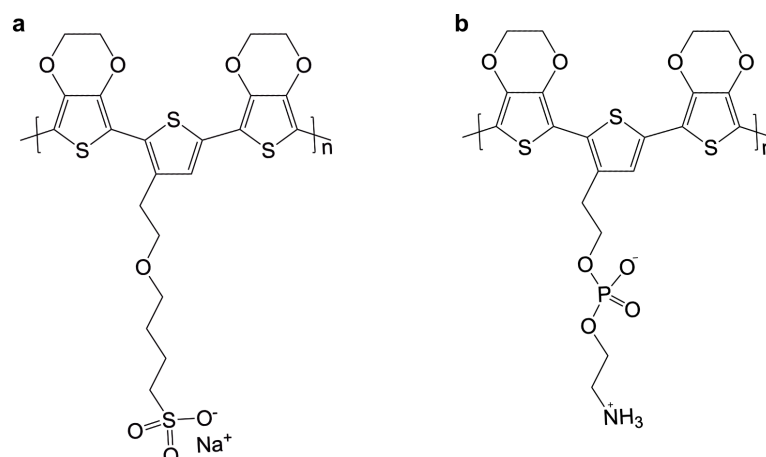


Figure 3.1: Chemical structure of the self-doped conducting polymers a) PETE-S in the reduced state where the sulfonate group on the side chain is compensated by a sodium ion and b) PETE-PC with its zwitterionic side chain. The trithiophenes represent one monomer unit of ETE-S and ETE-PC, respectively.

Electrochemical properties of ETE monomers and possible polymerisation routes

ETE-S and ETE-PC can both be oxidatively polymerised to form p-type conducting polymers. Holes induced during polymerisation create positively charged polarons and bipolarons in the central thiophene of the backbone as main charge carriers. [74] When polymerised, they typically form rather short chains with only two or three monomer units, a few nanometres in length, and could thus be considered as oligomers rather than polymers. [30] The two most frequently used polymerisation routes for ETE-S and ETE-PC include electrochemical polymerisation (often simply called electropolymerisation) and enzymatic polymerisation.

In order to electrochemically polymerise ETE monomers in an aqueous solution, a positive potential above the threshold oxidation potential of the monomers needs to be applied. Above the oxidation potential, the monomers get oxidised to a sufficient degree that polymerisation becomes tangible and insoluble conducting polymer molecules start to nucleate on the biased substrate. The oxidation potential of the monomer is therefore often taken as the onset potential of the electropolymerisation reaction and can be determined by cyclic voltammetry (CV). CV is a technique commonly used to study the electrochemical properties of an analyte in solution. The setup typically consists of a liquid cell with an analyte in an electrolyte solution in contact with a system of three electrodes: reference electrode, working electrode and counter electrode. The potential of the work-

ing electrode, measured against the reference electrode, is swept linearly in time in a cyclic manner between two vertices while the current between the working electrode and counter electrode is measured. The technique is commonly used to investigate redox processes. [75]

When determining the onset potential for ETE monomers with CV, the first oxidation peak of the first cycle during the anodic sweep (towards higher positive potentials) represents the oxidation of monomers and subsequent nucleation of conducting polymers on the working electrode. [14] The onset potential is determined as the start of the peak, which can be calculated by looking at the intersection of the tangent line of the peak and the tangent line of the flat region before the peak, as shown in Figure 3.2. [76]

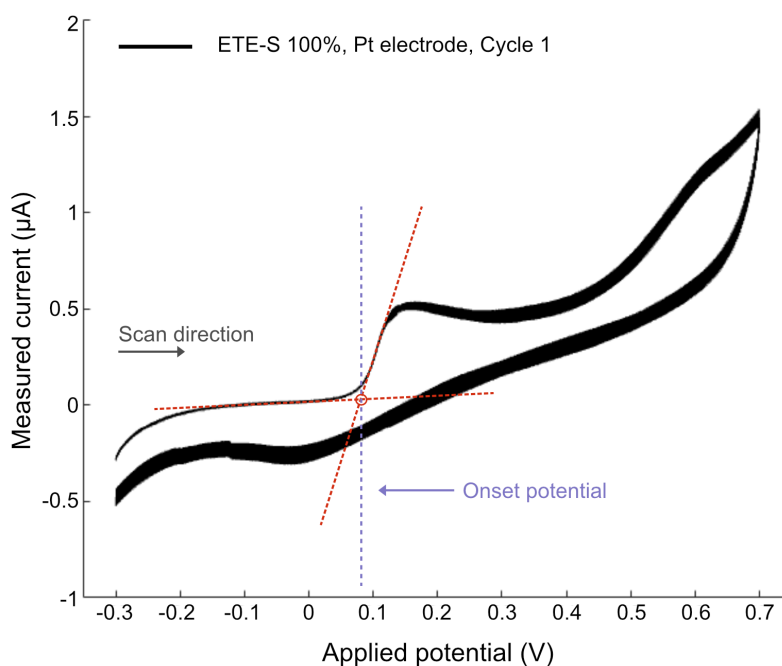


Figure 3.2: Determination of onset potential from a cyclic voltammogram of ETE-S using a biasing setup with Pt electrodes. Linear functions are fitted to the cyclic voltammogram before and at the slope of the first peak of the anodic (positive) sweep of the first cycle. This peak represents oxidation of the monomers. The onset potential is taken as the potential value at the intersection of the two lines. The corresponding onset potential for this sample is 0.08 V.

The onset potential depends on the monomer species, in particular on the charge of the side chain, and potentially also on the monomer concentration and the material of the electrodes. Electrostatic interactions can influence the distance between the monomer and the positively biased electrode but also the thermodynamics of the monomer oxidation. When CV of ETE monomers was carried out on fluorine-doped tin oxide electrodes, the measured onset potential was 0.30 V for the negatively charged ETE-S monomers and 0.47 V for zwitterionic ETE-PC monomers. [14]

The low oxidation potentials of ETE monomers are important for their high biocompatibility since it ensures low electric potentials are sufficient to electrochemically polymerise the material. This is specifically important in *in vivo* settings with sensitive tissue that could be damaged at higher potentials. Electropolymerisation of ETE-S and ETE-PC has been used in the development of evolvable OEECTs (EOECTs) for neuromorphic applications and synthetic synapses. [12–14] It has also been used in the development of bioresorbable electrodes in living zebrafish by injecting ETE-S or ETE-PC together with PEDOT-S in aqueous solution followed by electropolymerisation *in vivo* [11].

An alternative route to electropolymerisation is enzyme-assisted polymerisation, which is often more gentle to the surrounding material. It has been shown that ETE-S can be enzymatically polymerised by peroxidases in the presence of H_2O_2 . This has been applied to promote spontaneous polymerisation of ETE-S into conducting wires and supercapacitors in plants [8] and in invertebrate animals such as hydras [9] by the native environment in these biological systems.

Solubility and aggregation behaviour of ETE monomers

The ETE-S and ETE-PC monomers are reported to be soluble in aqueous media up to concentrations of at least 10 mg mL^{-1} because of their hydrophilic side chains. [14] However, it has been shown that ETE monomers tend to aggregate in solution as a result of π - π stacking interactions. [16] For ETE-S, π - π stacking of two to three oligomer chains leads to the formation of small crystallites. It only occurs for dimer or longer polymers where the stacking distance is $r_{\pi-\pi} = 3.5 \text{ \AA}$. Percolative paths do not exist for ETE-S monomers, only for dimers, trimers and longer polymers where charge carriers can travel between π - π stacked chains and along single polymer backbones that form electrical connections between stacked regions. [30]

For *in vivo* polymerisation and fabrication of bioelectronics based on networks of conducting polymers in brain tissue to be possible, the molecule precursors need to be small enough to pass the blood-brain barrier (BBB). The BBB is a microvas-

cular network that controls the transport of molecules between the central nervous system (CNS) and the circulatory system to maintain homeostasis in the CNS and protect the CNS from toxins and pathogens. The controlled environment in the CNS is necessary for the proper function of the neurons inside it. The physical wall of BBB is made up of endothelial cells. [77] Nanoparticles and other molecules with sizes below 200 nm can permeate through the BBB but the permeability decreases rapidly for larger molecules. [78, 79] Substantial aggregation of monomers into large clusters could thus limit their ability to pass through cell membranes or enter the CNS via the BBB.

Molecular dynamics simulations have demonstrated that ETE-S and ETE-PC monomers aggregate in water solutions at monomer concentrations above 0.3-0.4 mM. [16] The simulations also revealed that ETE-S and ETE-PC form different types of aggregates. More short-range ordering was found in ETE-S aggregates compared to ETE-PC aggregates as a consequence of the long, charged side chains of ETE-S. Moreover, ETE-S was shown to form more elongated aggregates than ETE-PC. However, these simulations were performed with a limited box volume of $7 \times 7 \times 7 \text{ nm}^3$. In comparison, the size of a single monomer unit is approximately 1 nm, so only a small number of monomers (20 monomer molecules) were included, which does not allow the simulations to fully capture the shape and size of large aggregates. The morphology of the aggregates is thus not completely known and needs to be studied further to understand the self-assembly processes and structure of the monomer solutions along with how they evolve when used in different devices. This thesis investigates the micro- and nanoscale structures of ETE-S and ETE-PC monomers in electrolyte solutions commonly used for device fabrication. The aggregation behaviour of each monomer type as well as mixed monomer solutions with equal parts ETE-S and ETE-PC are analysed using the structural characterisation techniques presented in Section 3.2.

3.1.2 OEET Devices

Most OEET devices rely on various pre-patterning techniques such as photolithography, printing, or spin-coating deposition of the organic semiconductor channels before device operation. However, EOECTs are becoming increasingly attractive because the channel can be grown *in operando* through electropolymerisation of conducting polymer films as a response to external stimuli. The attractiveness of EOECTs lies mainly in their ability to modulate the electrical transistor characteristics to mimic the function of a biological synapse. In the biological synapse analogy, the gate of the OEET acts as the presynaptic terminal, the drain acts as the postsynaptic terminal and the channel conductance represents the synaptic strength. The channel conductance of an EOECT can be increased by growing

more channel material or reduced by overoxidising the channel. This allows the device to mimic long-lasting potentiation and depression of the synaptic weight in a neuromorphic system of artificial synapses. The ability to modulate the channel conductance by changing the stimulus applied to the device is thus important to capture the dynamic neuroplasticity of biological systems where the formation of new electronic synapses is a stimulus-driven process. Transient behaviours can also be modelled by ionic doping or dedoping of the channel, modulated by the gate voltage. [12]

In this thesis work, electropolymerisation of ETE-S monomers dissolved in an aqueous solution with NaCl is utilised to form a conducting polymer transistor channel. This is an evolvable OECT that can operate in both accumulation and depletion mode, allowing the drain current to be modulated over a large range, both positively and negatively depending on the gate voltage. [12] The transistor channel is grown between a set of pre-patterned Au electrodes on a surface-modified SiO₂ substrate by applying an electropolymerising voltage of 0.50 V to the drain. The chosen value of the drain voltage, V_D , was assumed to be sufficient to effectively polymerise the ETE-S monomers. [14] A schematic of the OECT device is shown in Figure 3.3. The electronic properties of such OECT devices have been documented [12–14], but details about the micro- and nanostructure of the transistor film are not well known. It has been suggested that the electric potential applied to the system has an influence on the polymer film growth, yet the effects of the local electric potential have not been fully investigated. In this thesis work, the effect of the local potential of the substrate and electrolyte solution on the polymer film structures such as film area and surface roughness are analysed. The structures are correlated to associated device properties. The aggregation characteristics of the monomers in the electrolyte solution and their impact on the structure and properties of the polymerised film are also addressed.

Device fabrication

OECT devices were fabricated on insulating SiO₂ substrates with Cr-backed Au electrodes. The SiO₂ substrates were modified with partially positive (3-aminopropyl) triethoxysilane (APTES) to help pre-concentrate the monomers in solution close to the substrate before polymerisation, as has been previously described [14,80]. The metal source and drain electrodes were designed to consist of a 2 nm chromium sticking layer under a 50 nm gold layer. The channel length, corresponding to the distance between the electrodes, was set to 30 μm and the channel width was 1000 μm .

The electrolyte solution consisting of deionised (DI) water with 1 mg mL⁻¹ ETE-S

and 10 mM NaCl was contained in a 2 mm thick PDMS well placed around the electrodes as shown in Figure 3.3. The contact pads for the electrodes were outside the PDMS well. An Ag/AgCl pellet was dipped into the electrolyte solution. The pellet acted as gate electrode and counter-reaction for electropolymerisation by injecting chloride ions into the solution. The source and gate terminal were connected to a common ground while a working electrode was connected to the drain. Polymer film channels consisting of PETE-S were grown by applying a constant voltage of 0.50 V to the drain for 2 s, 30 s, 60 s, or 120 s using a Keithley 2612B Source Meter. The drain current was monitored during channel growth to assess the electric behaviour of the device. The drain voltage was chosen to be 0.20 V higher than the documented oxidation onset potential for ETE-S monomers to ensure efficient polymerisation. [14] A voltage of 0 V was applied after the set time for channel growth until the drain current stabilised. The channels were then washed with DI water to remove excess electrolyte solution and dried under ambient conditions.

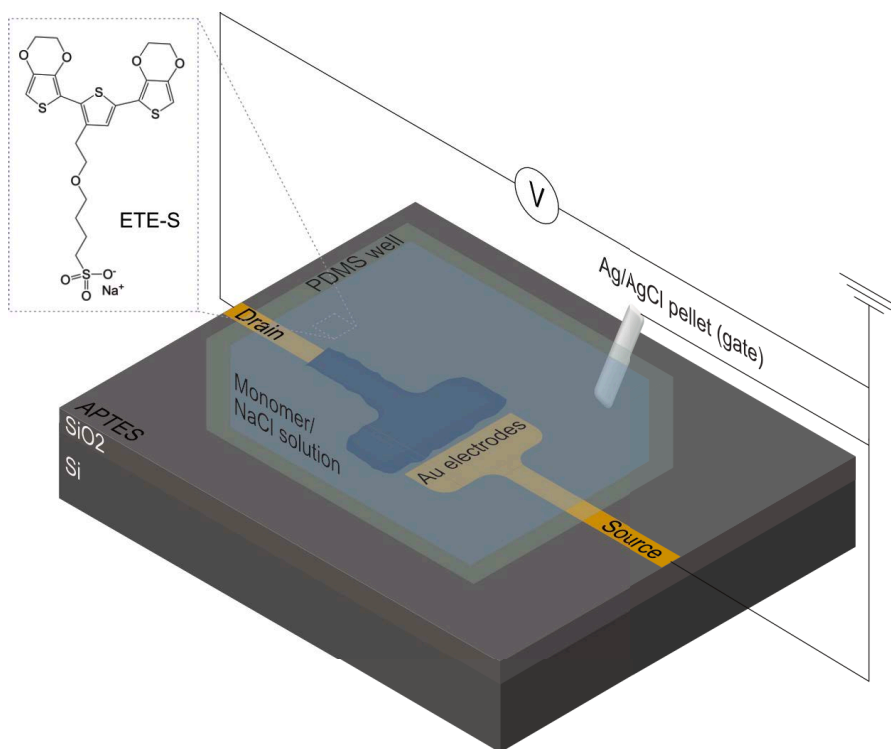


Figure 3.3: Schematic of the OEET device consisting of a pair of Au source and drain electrodes patterned on an APTES-modified SiO₂ substrate. A voltage is applied to the drain electrode for a given amount of time to oxidatively electropolymerise the ETE-S monomers in the electrolyte solution.

3.1.3 Electrically Conducting Hyaluronan Hydrogels

Conducting hyaluronan-based hydrogels with enzymatically polymerised ETE-S to be used as a bioink for printing of cell-compatible structures have been developed at the Laboratory of Organic Electronics and Laboratory of Molecular Materials at Linköping University (Paper III). The integration of conducting nanoscale networks of PETE-S in the hyaluronan (HA) hydrogel is intended to mimic the conductive networks existing in neural tissue. The water-soluble monomers can be polymerised *in situ* which opens up new possibilities of device formation inside tissue that is otherwise difficult to achieve for pre-polymerised materials. The enzymatic polymerisation route of PETE-S also bypasses the need for suitable electrochemistry or strong redox chemistry which is typically needed for other conducting polymers used in tissue engineering. [8] Naturally occurring metabolites in common physiological environments can be used to control the enzymatic polymerisation, making the PETE-S loaded hydrogel attractive for use with PC12 cells and for growing conducting wires inside plants [81] or animal tissue [10].

Fabrication of hydrogel samples

HA is a polysaccharide that can be found abundantly in the ECM as well as in connective tissue and neural tissue. It has an important role in cell proliferation and migration, as binding sites for anchoring to cell surfaces, tissue lubrication, and the growth of new blood vessels or skin cells. [82] Here, HA is modified with bicyclo[6.1.0]nonyne (BCN) to form HA-BCN which is cross-linked with 4-arm polyethylene glycol with terminal azides (PEG-Az4) by bioorthogonal click chemistry to form a robust hydrogel abbreviated as HA-BCN/PEG. The ratio between azides and BCN in the hydrogel controls the amount of cross-linking and can be tuned to achieve a desired elasticity. This type of hyaluronan hydrogels have previously been shown to be useful in three-dimensional neuronal cell cultures. [15]

To make the HA-BCN/PEG hydrogels electrically conductive, ETE-S monomers together with the enzyme horseradish peroxidase (HRP) at equal concentrations of 0, 5, 10, and 20 mg mL⁻¹ were added to the aqueous solutions of HA-BCN and PEG-Az4 in phosphate buffered saline (PBS). After cross-linking of the hydrogels, a 1 mL solution of H₂O₂ was added to initiate the enzymatic polymerisation of ETE-S inside the hydrogels. The polymerisation could be observed as a change in colour of the solution from very light brown to dark blue. A majority of the conducting hydrogels were kept in a PBS solution while measurements were carried out to assess their mechanical and electrical properties as well as cytocompatibility. A set of hydrogels were freeze-dried to preserve the native material structures for structural characterisation.

Freeze drying

Freeze drying, or lyophilisation, is a dehydration process often applied to preserve foods, pharmaceuticals and biological material. The process works by removing water and other solvents from the material through freezing at ambient pressure followed by sublimation of ice at low pressure. The process is often divided into three steps: freezing, primary drying and secondary drying.

During the freezing step, a phase separation is induced by thermodynamic instabilities which causes the solvent to separate from the solutes as the solvent freezes and, in the case of water, forms ice crystals around the solutes. This step is typically carried out at ambient pressures and at temperatures necessary to completely freeze the solvent in question by cooling it below its triple point. The rate of freezing will affect the size of the ice crystals that form, with larger crystals forming at lower freezing rates. Avoiding the formation of large ice crystals is very important for preserving the native structure of the material, especially for structurally sensitive materials such as cells.

After the material is completely frozen, primary drying takes place by lowering the pressure of the chamber surrounding the sample below the vapour pressure of the type of ice in the material (often a few millibars) and applying heat to make the ice sublime. The driving force for the sublimation is the pressure gradient between the sublimation interface and the surrounding chamber. This means that sublimation starts at the surfaces of a bulk sample and the sublimation interface continues inwards as material gets transported away. At the end of the primary drying process there is typically still some unfrozen water adsorbed to the surface of the sample which can be removed in the secondary drying. The temperature is then increased and the pressure of the chamber reduced further to induce desorption. [83]

Pore formation in hydrogels

As discussed in Section 2.4, the porosity of hydrogels is of great importance for their properties and performance in applications such as scaffolding in cell cultures and for tissue engineering. The overall porosity of a hydrogel can be controlled by solvent casting/particle leaching, freeze drying, gas foaming, and electrospinning.

Solvent casting and particle leaching involves dispersing a porogen (often salt particles, sugars, paraffin or gelatin) with known particle size into a hydrogel-forming polymer solution which is later solidified to form a network of polymers around the porogens. The material is then immersed in a solvent to leach away the porogens, leaving only the porous polymer network. The porogen particle size and geometry

can be tuned to yield a desired pore size and interconnectivity. [60]

Freeze drying is one of the most commonly used techniques for forming porous hydrogels. Voids form in the regions that contained solvent before it was removed from the material. Parameters such as the temperature and cooling rate during the initial freezing of the material has a large influence on the final architecture of the hydrogel since the kinetics of the quenching process affects the pore formation. These parameters should be tuned to control the resulting pore size. [60, 84, 85]

The gas foaming method introduces gas bubbles that nucleate and grow throughout the polymer to create a porous structure. The gas can be introduced either by a foaming or blowing agent that is mixed into the polymer solution and generates a gas upon decomposition, or the gas can be released from presaturated gas-polymer mixtures. Most foaming and blowing agents produce CO_2 and/or NH_3 , are widely available and inexpensive while also having high cytocompatibility making this technique well suited for inducing porosity in hydrogels for tissue engineering.

Electrospinning utilises the application of an external electric field to draw a charged polymer solution into long thin fibers in the nano- and micrometre range. The diameter, porosity and morphology of the polymer fibers can be controlled by parameters such as the voltage applied to generate the electric field, the viscosity, conductivity and temperature of the polymer solution. [60]

It has also been shown that the cross-linking step during hydrogel formation also affects the porosity of the material. [63, 86, 87] The pore wall thickness can be expected to increase while the average pore size decreases as the level of cross-linking increases. Cross-linking and freeze drying are the main pore forming processes in the hydrogels studied in this thesis.

Effect of incorporated PETE-S

This thesis investigates the effect of the concentration of the incorporated polymer PETE-S on the structure of the hydrogel. The porosity of the hydrogels is especially important since it affects not only the mechanical properties but also the cell migration and proliferation in the hydrogel scaffold. Both the pore size and interconnectivity of pores have been assessed in this thesis work by looking at surface structures and internal structures in the bulk of the materials.

3.2 Structural Characterisation

Identifying and describing functional material structures on the micro- and nano-scale require techniques with high spatial resolution. Electron microscopy techniques are prime candidates for performing this characterisation due to their ability to resolve fine features. The high-resolution capability of electron microscopy stems from the implementation of a focused beam of high-energy electrons which is used to investigate a sample. Paired with the ability to analyse both surface and bulk structures, such characterisation techniques are necessary to understand how the material structures relate to physical properties such as electrical conductivity.

This section describes the principles of electron microscopy and other structural characterisation techniques used in this thesis. It also highlights the importance of implementing multiple complementary techniques in order to fully describe the structure of a material.

3.2.1 Scanning Electron Microscopy (SEM)

Scanning electron microscopy (SEM) can be used to observe and characterise the micro- and nanoscale structures of a wide range of materials. It is especially useful for characterising bulk samples because of its ability to image three-dimensional surface structures due to its large depth of field. [88] SEM is applicable to many materials, including both organic and inorganic samples. One of the main requirements placed on samples for SEM is that they should have a conducting surface to avoid charge buildup when the electron beam is interacting with the sample. Non-conducting samples can be sputter-coated with a thin layer of gold, palladium or chromium to form a conducting surface layer. The thickness of this layer is usually kept to a few nanometers to avoid obscuring the topography of the sample surface. The samples should also be stable under the vacuum conditions of the microscope. The chamber pressure in an SEM under normal operation is typically on the order of 10^{-4} Pa. Alternatively, the SEM instrument can be operated at higher pressures by introducing a gas into the sample chamber. This technique is known as variable pressure SEM (VPSEM) or environmental SEM (ESEM) and allows for imaging of hydrated samples in their native state. Using these techniques, insulating samples can also be imaged without needing to apply a conductive coating. When the electron beam interacts with atoms in the surrounding gas, they become ionised and form cations that help neutralise negative charge build-up on the sample surface. The gas can also reduce charging by absorbing some of the electrons that are emitted from the sample. However, the achievable resolution in VPSEM and ESEM is typically lower than that of high vacuum SEM due to the interactions between the beam and the gas. [88]

A schematic of the typical components of an SEM is shown in Figure 3.4. Electrons are emitted from a thermionic, Schottky or field-emission cathode acting as the electron source. The electrons are then accelerated in the electric field generated by a voltage difference between the source cathode and an anode. The voltage difference determines the kinetic energy the electrons reach and typically ranges from 0.1 keV up to 30 keV. [89] The electron beam is focused into a fine probe which is scanned over a sample surface to form an image using signals generated from the sample. The use of a high-energy electron beam allows SEM imaging to reach spatial resolutions down to the order of 1 nm. [90] In contrast to optical microscopy, the resolution in SEM is not diffraction-limited but instead depends on the shape and size of the electron beam limited by diffraction and spherical aberration, the specimen interaction volume, and the Poisson statistics of the detected signal. [90]

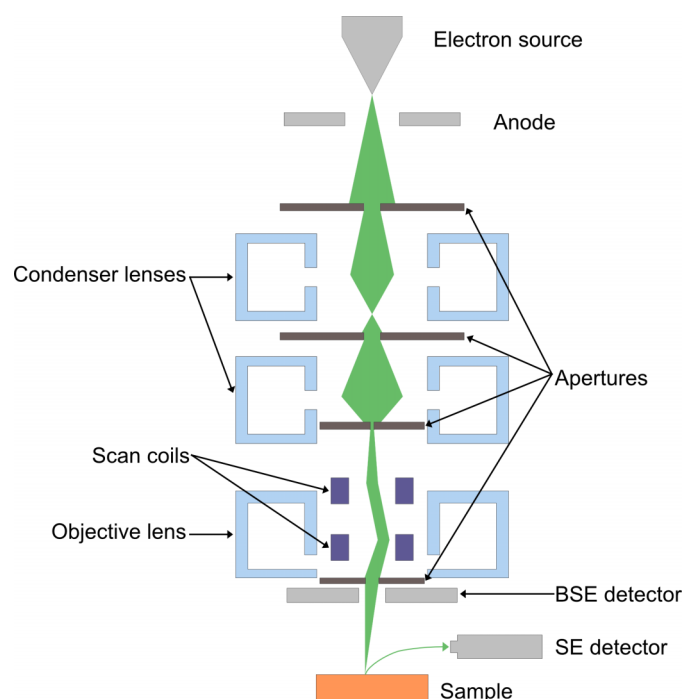


Figure 3.4: Schematic of the key components of an SEM. Electrons are emitted by the electron source and accelerated to high velocities by an electric field between the electron source (cathode) and the anode. A set of electromagnetic lenses and apertures are used to control the beam diameter. The scan coils deflect the small diameter beam and raster scan it across the sample surface. Signals are generated at the different positions where the beam interacts with the sample and collected, pixel-by-pixel in synchronisation with the beam by a set of detectors to form an image of the analysed area.

Image formation and signals in the SEM

To form an image of a sample, the focused electron beam is raster scanned in an x-y pattern across an area of interest, stopping at discrete positions for a given amount of time, usually on the order of a few μs . [88] At each position, elastic and inelastic scattering events give rise to a set of signals that can be collected by detectors and used to build a digital image pixel by pixel. The brightness of each pixel represents the signal strength from the corresponding position on the sample.

The three main signals commonly used in SEM analysis are backscattered electrons (BSEs), secondary electrons (SEs) and characteristic X-rays. The first two signals are mostly used for imaging purposes, whereas the last signal can be used for chemical analysis of a sample. Other signals that can be detected and analysed in an SEM are photons emitted via cathodoluminescence and Auger electrons.

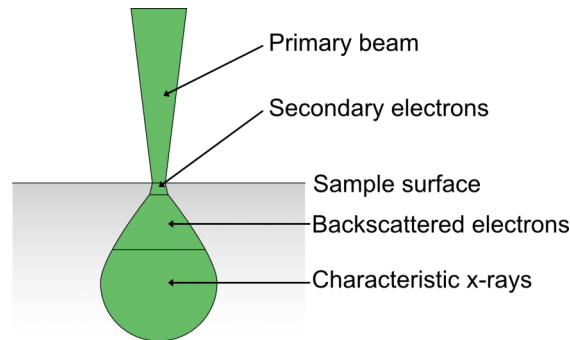


Figure 3.5: Qualitative illustration of the effective interaction volume in SEM. The volume from which secondary electrons, backscattered electrons and characteristic X-rays can escape and be detected is different for each signal type. This volume can be seen as the information depth and is smallest for secondary electrons.

The interaction volume from which signals are generated depends on the penetration depth of the electron beam. This is determined by the mean free path of electrons in the material and is influenced by the energy of the incident electrons, the atomic number and density of the sample material. In general, higher beam energies and lighter elements in the sample lead to a larger penetration depth. [88] In order to be detected, the signals need to escape the sample. The possible escape volumes vary for the different signal types and therefore also their effective interaction volumes. A qualitative illustration of the effective interaction volumes for the three main signals is shown in Figure 3.5. As the electron beam interacts with atoms in the sample, the beam is broadened. Because of beam broadening,

signals that can be generated and escape from a larger depth in the material have reduced spatial resolution due to the larger interaction volume.

Backscattered electrons

BSEs are electrons that originate from the primary beam and may have undergone multiple elastic and inelastic scattering from atomic nuclei in the sample. Elastic scattering occurs when an incoming electron is deflected by the Coulomb field of an atomic nucleus in the sample. Inelastic scattering occurs in Coulomb interactions between incoming electrons and electrons in the sample atoms where the incoming electrons lose part of their energy to the sample atoms. The trajectory of the BSEs may change in each scattering event until they eventually escape the sample almost anti-parallel to the incident beam. The kinetic energy of BSEs leaving the sample ranges from approximately 50 eV to the energy of the incident electrons [89]. Since a fairly large fraction of the BSEs retain high kinetic energies, signals generated at large depths in the sample are able to escape and be detected, giving this signal type a large interaction volume. The main contrast mechanism for BSEs comes from compositional contrast since the probability of backscattering depends strongly on the atomic number, Z , of the elements in the sample. Heavier elements yield a higher BSE signal than lighter elements, making this signal type useful for compositional studies. [88]

Secondary electrons

SEs are generated from the sample when the high-energy electrons in the primary beam undergo inelastic scattering and eject weakly bound electrons from atoms in the sample. These SEs are ejected with significantly lower kinetic energies, <50 eV, than the incident primary electrons, which have incident energies of 1-30 keV. The SEs can thus easily be reabsorbed by atoms in the sample as they propagate within the material and undergo further inelastic scattering, reducing their kinetic energy. The yield of SEs emitted relative to the number of incident electrons in the primary beam increases as the energy of the primary beam decreases. [88] SEs are generated throughout the whole interaction volume of the primary beam, but only SEs created within a few nanometers from the sample surface maintain enough energy to surpass the energy barrier of the surface and escape to the detector. The effective interaction volume is therefore small (see Figure 3.5) and the spatial resolution of the SE signal is high (comparable to the beam diameter). The small SE escape volume also makes the SE signal especially useful for studying the surface topography of a sample. [88]

In addition to the SEs created by the primary beam, SEs can also be created from BSEs that undergo inelastic scattering in the sample. This second class of SEs

have the same energies and angular distributions as the first class, but have a spatial resolution more comparable to that of BSEs and their signal strength scales with the backscattered signal strength.

Characteristic X-rays

Characteristic X-rays are produced from atoms that have inner shell vacancies caused by the ejection of inner shell electrons during inelastic scattering events, such as scattering events producing secondary electrons. The ionised atoms are at a raised energy state that can be lowered by filling the empty inner states with outer shell electrons. The energy difference between the shells involved is quantised and unique for each electronic transition in each element. The transition energy is used to create a characteristic X-ray photon with the same specific energy, which acts as a fingerprint of the atomic species and shells involved in the transition. This makes characteristic X-rays useful for performing elemental analysis by collecting the photons and measuring their energies using energy dispersive X-ray spectroscopy (EDX).

The energy made available through the inter-shell transition does not always result in the creation of a photon but can also be used to eject an Auger electron from the atom. The probability of X-ray emission or emission of Auger electrons is not the same for all elements. Lighter elements are more likely to emit Auger electrons and the probability of emitting characteristic X-rays increases rapidly with atomic number. [88]

Characteristic X-rays are created within the whole interaction volume of the primary electron beam. They have a lower probability of reabsorption than BSEs and SEs since the photons are massless, allowing the signal to escape from larger depths in the sample. However, not all X-rays generated within the sample manage to escape. Some are absorbed by other atoms in the sample through the photoelectric effect if the energy of the X-ray photon matches the critical ionisation energy of another atom. This makes the detection of X-rays from light elements particularly difficult. Finally, it should be noted that X-rays with lower energies are more likely to be reabsorbed than high-energy X-rays. X-rays are not only produced by the primary electrons but can also be created from BSEs. [88]

Detectors used for imaging

Most SEMs are equipped with Everhart-Thornley (E-T) detectors to collect the SE and BSE signals. The detector is usually placed above the sample, on the

wall of the specimen chamber. The E-T detector is most commonly subject to a positive bias with a potential of a few hundred volts, causing the low-energy SEs to be deflected towards the detector. Even SEs emitted in a direction away from the detector will change trajectory and get drawn into the detector. The potential is not high enough to affect the trajectories of high-energy primary electrons or BSEs, but BSEs already directed toward the E-T detector will still be detected. This makes the total signal collected by the detector a mixture of SEs generated by the primary beam, SEs generated by BSEs and small amounts of direct BSEs. Because the majority of the signal comes from SEs, the image generated by this detector is often described as the secondary electron image and the contrast mechanism is mostly originating from the sample topography. [88]

The off-axis placement of the E-T detector is often inefficient for picking up sufficient BSE signal to form a BSE image due to its small solid angle of detection. An additional BSE detector is often introduced, placed directly below the final objective aperture as shown in Figure 3.4. This detector is typically a scintillator or semiconductor type detector with a larger solid angle of signal collection. The BSE detector efficiently collects the signal from the high-energy electrons, generating an image with atomic number contrast.

Interpreting the topography in SEM images

Interpreting the topography in an SEM image of a three-dimensional sample is fairly easy because of the similarities between the SE signal intensity and the patterns of highlights and shading human eyes detect in everyday life.

The amount of secondary electrons emitted from a surface and detected is strongly dependent on the surface inclination and orientation. Surfaces at a high inclination with respect to the primary electron beam give rise to a larger number of SEs since the effective volume from which the electrons can escape increases. Edges and small objects also tend to appear bright in images generated from SEs due to lower relative volume that would absorb the generated SE signal. [88] Flat surfaces and valleys have smaller effective interaction volumes from which SEs can escape and give rise to weaker SE signals. This is illustrated in Figure 3.6.

The placement of the detector relative to the sample orientation also has an effect. If the sample surface is tilted towards the E-T detector it will appear brighter than if it is tilted away from the detector because of the direct contribution of BSEs. Regions on the sample which the electron beam does not interact with, e.g. regions underneath an overhanging piece of sample, do not generate any signal and will appear black. Figure 3.7 shows the effect of the detector placement using the light-optical analogy to the SEM image.

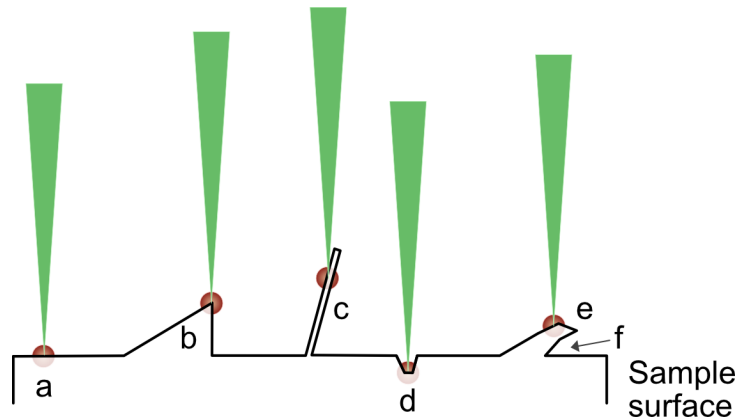


Figure 3.6: Illustration of the effect of surface topography on the SE signal strength. The red circles show the fraction of SEs that can escape from the sample for different surface features including a flat surface (a), a sharp edge (b), a thin structure (c), a valley (d), a thick overhang (e) and an area underneath an overhang (f). The SE yield is highest for edges, tilted surfaces and thin protruding structures.

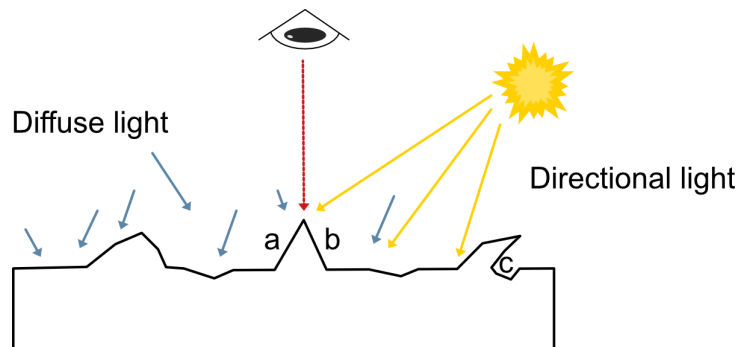


Figure 3.7: Light-optical analogy to an SEM image generated with a positively biased E-T detector. A viewer sees a landscape from above, lit with directional light from the Sun and diffuse light scattered from an atmosphere or objects in the landscape. The viewer's line of sight corresponds to the incident electron beam in the SEM. The position of the source of directional light represents the positively biased E-T detector which collects the direct signals from BSEs and SEs. The diffuse light corresponds to SE signals and can be seen even in places not struck by the directional light. For this reason, some signal is detected from side (a) on the triangular feature but the signal is weaker than from side (b) which is facing the E-T detector (Sun). Site (c) is completely dark since it can not be reached by the electron beam (line of sight).

The BSE signal can also give topographic contrast since it depends on the surface tilt. BSEs tend to move in straight trajectories and has a strong directionality towards the normal of the sample surface [89]. As the surface tilt angle increases away from the direction of the incident beam, the BSEs tend to follow the direction of the incident beam. Higher tilt angles yield a larger number of BSEs. [88]

3.2.2 Transmission Electron Microscopy (TEM)

In transmission electron microscopy (TEM), the high-energy electron beam is transmitted through the sample and analysed beneath the sample. Because the electron beam needs to be able to pass through the sample without too much interaction, the sample needs to be very thin, usually around 100 nm or less in thickness [91]. This makes TEM less suitable for analysing bulk samples without thinning them down or extracting small volumes. On the other hand, the resolution achievable in TEM can reach below 0.1 nm [91], with modern aberration-corrected microscopes able to achieve resolutions down to 50 pm [92]. The atomic resolution capability of TEM offers a unique opportunity to investigate the atomic structure of materials.

Figure 3.8 illustrates the general components of a TEM. As in SEM, the electrons are generated from an electron source and accelerated to high velocities by an electric field. The acceleration voltage used in TEM is typically in the range of 60-300 keV. [91] The illumination system comprised of the condenser lenses and condenser apertures control the shape and size of the beam from the electron source. In conventional TEM, the condenser lenses form a broad, parallel beam which can be several micrometers in diameter when it encounters the sample. In scanning TEM (STEM), the beam is instead focused into a small probe that converges at the sample and is scanned across the sample area, similar to SEM. The electron beam interacts with the sample as it passes through it, giving rise to multiple different signals. The objective lens system then forms the image and diffraction patterns (DPs) of the sample that are then magnified and projected onto a fluorescent screen or CCD camera that allows the signals to be viewed and recorded. [91] Many modern TEMs include scintillator cameras based on complementary metal oxide semiconductors (CMOS), or direct electron detectors for fast, high efficiency electron detection. As in SEM, the sample and all image forming components of the TEM are normally kept under high vacuum conditions to minimise undesired scattering from particles in the surrounding environment and sample contamination.

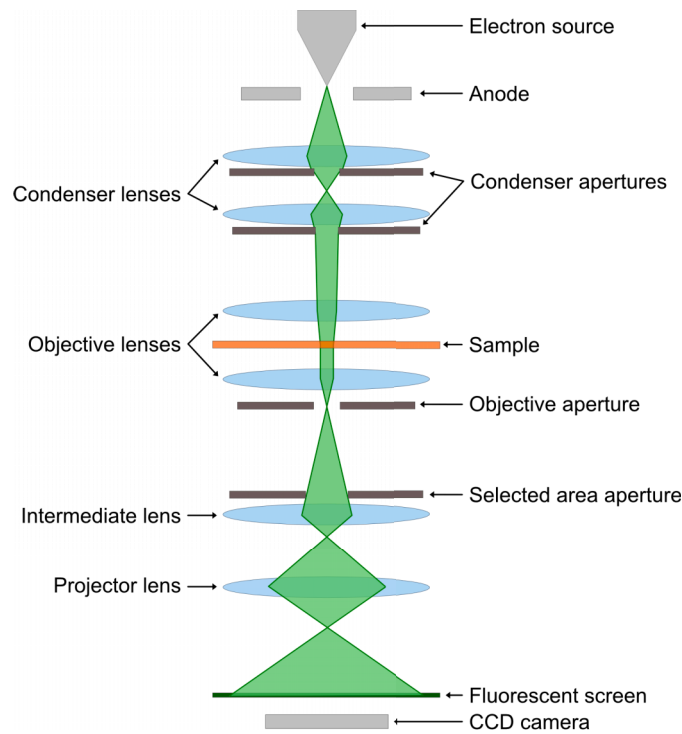


Figure 3.8: Simplified schematic of the typical components of a TEM. Electrons are emitted at the top of the instrument and accelerated by an electric field. The beam is focused using electromagnetic lenses into a broad beam, parallel to the optical axis, or focused beam that illuminates the sample. Objective lenses form an image of the sample and the diffraction pattern which is further magnified and projected onto the fluorescent screen or CCD camera. Note that different microscopes can have different amounts of lenses and apertures.

Signals in the TEM

When the electron beam interacts with the sample, SEs, BSEs, and characteristic X-rays are produced and can be analysed also in TEM. The most commonly used signals, however, are those belonging to electrons that have been transmitted through the sample. A part of the electrons will pass through the sample without being scattered or only scattered to small angles. This is often considered the direct beam. Electrons can also be elastically scattered to higher angles in interactions with the sample atoms. In crystalline samples, the atoms are ordered in a periodic lattice which leads to scattering at specific angles that fulfil Bragg's law. This type of scattering is often referred to as electron diffraction and is very useful in determining the crystal structure of a material. [91] Finally, some electrons have undergone inelastic scattering and lost part of their energy to the sample.

The remaining energy of the transmitted electrons can be measured in a technique called electron energy-loss spectroscopy (EELS) which can give information about the elemental composition and chemical state of the elements in the sample. [93]

The electrons in the unscattered, direct beam can be collected at the fluorescent screen or CCD camera below the sample to form a bright-field (BF) image of the sample. Such an image is bright in places where little scattering occurs and dark in places where the electrons have been scattered to high angles, following the diffraction contrast mechanism. Electrons scattered to high angles can be used to form a dark-field (DF) image. [91]

An image of the sample is formed in the image plane of the objective lens below the sample. A so-called diffraction pattern (DP) is formed in the back focal plane of the objective lens. Electrons that undergo diffraction from the same set of parallel atomic planes in the sample are scattered in the same direction and get focused into one spot in the back focal plane. The unscattered (direct) part of the beam always forms the central spot in the DP. The distance from the central spot to a diffraction spot is inversely proportional to the distance between the corresponding atomic planes in real life. Randomly oriented crystalline regions in a sample will produce a pattern of concentric bright rings around the central spot rather than discrete bright spots. [94] The strength of the intermediate lens can be adjusted to choose whether an image or DP should be projected onto the fluorescent screen or CCD camera.

By placing an objective aperture of adjustable size and position in the back focal plane of the objective lens where the DP is formed, it is possible to select only the unscattered part of the beam, corresponding to the central spot, for BF imaging or one or more diffracted beams for DF imaging. DF imaging is especially suitable for identifying lattice defects in crystalline samples or analysing polycrystalline samples since it allows the user to select the signal coming from a specific set of atomic planes as main contributors to the intensity in the image, leaving regions with atomic planes scattering to other angles dark. [91]

Imaging in the TEM relies on three main types of contrast mechanisms: phase-contrast, mass-thickness contrast and diffraction contrast. Phase contrast arises from interference between the transmitted, unscattered part of the beam and one or more scattered beam parts. Scattering of the electrons passing through the sample will give rise to small phase differences within different parts of the beam. The analysed sample needs to be very thin so that the electrons are not significantly absorbed in the material but only undergo phase change and a single scattering event. By adjusting the focal length of the objective lens, also known as the Scherzer defocus, the relative phase difference between the scattered and unscat-

tered electron beam can be modified and converted into a change in amplitude in the image. The amplitude variations produce an image contrast based on the interference between the different parts of the beam. The defocus can be selected to maximise the contrast intensity in the image. [91] Phase contrast imaging is commonly used in the BF mode and high-resolution TEM (HRTEM).

Mass-thickness contrast is produced by incoherent (Rutherford) elastic scattering of the electron beam. The elastic scattering increases rapidly with atomic number, density and thickness of the sample, giving rise to intensity differences in an image of the sample. A region of higher atomic number or thickness will appear darker in a BF image than a region with lower mass or thickness. The mass-thickness contrast can be modified by changing the size of the objective aperture to change the ratio of scattered to unscattered electrons that pass through the aperture. Smaller objective apertures block out more scattered electrons and increase the mass-thickness contrast. Decreasing the acceleration voltage also increases contrast between high-mass and low-mass regions. Mass-thickness contrast is especially important for noncrystalline materials such as polymers and biological samples. These are often stained with heavy metals to increase mass contrast. [91]

It should be kept in mind that TEM imaging can give detailed information about the internal structure of a sample but projects three-dimensional structures onto a two-dimensional view. Hence, thicker samples can lead to multiple overlapping features along the same line of sight. [91] Hence, it can be beneficial to compare results from the two different electron microscopy techniques.

3.2.3 Electron Beam Damage

Electron beam-sample interactions play a fundamental role in all electron microscopy experiments and the beam effects need to be understood to accurately interpret any results. Electron microscopes are capable of achieving astonishingly high resolutions through the use of a high-energy beam of electrons. In addition to providing useful information, the electron beam can also cause unwanted radiation damage which changes the structure of a material from its true state. Beam damage can occur as a result of both elastic and inelastic scattering of electrons. Here, the most common damage mechanisms and ways to mitigate them will be listed, with a focus on the main types of beam damage occurring in soft materials such as polymers.

Damage induced by elastic scattering

Elastic scattering of incoming primary electrons with sample atoms does not alter the total amount of energy of the particles involved in the collision. However, energy from the incoming electrons can be transferred to the atomic nucleus as the electron is deflected at an angle due to conservation of momentum and energy. For high-angle scattering, such as that involved in the production of BSEs, or head-on collisions with the nucleus, the energy transfer can be several eV. If the transferred energy exceeds the displacement energy of the material, the sample atoms can be displaced from their original positions. This damage process is also known as "knock-on damage". The displacement energy of a material depends on the atomic weight, bond strength to surrounding atoms, and location within the sample. The atomic displacement effect is more prominent for atoms of lower atomic weight and at higher beam energies since the transferred energy needs to exceed the displacement energy. Knock-on damage can thereby be mitigated by lowering the beam energy beneath the displacement threshold for the studied material. [95]

The displacement effect also depends on the position within the sample. An atom at the surface is more easily displaced than an atom in the bulk of the sample. The removal of surface atoms by this process is called "sputtering" and occurs more commonly on the exit side of the beam than the entrance side. Depositing a protective layer of high atomic number on the exit surface can minimise mass loss from the sample. [95]

Knock-on damage is the dominant damage mechanism for conducting materials like metals and some semiconductors. In a crystalline sample, atomic displacement will degrade the level of crystallinity. [96]

Damage induced by inelastic scattering

Inelastic scattering can lead to a large transfer of energy from the incoming electrons to the sample atoms. This energy, which can range from a few eV to hundreds of eV, may cause heating or radiolysis of the sample, including excitation of conduction or valence electrons and ionisation of inner shell electrons. The ejection of secondary electrons from the sample also leads to electrostatic charging in poorly conducting samples. These damage mechanisms are negligible in conducting specimens such as metals but are the major sources of damage in insulators and some semiconductors. They are especially important to consider for organic materials. [95]

Radiolysis (ionisation damage) originates from the creation of vacancies in the

valence band or inner electron shells of sample atoms, resulting in an excited electronic state. If these excitations are long-lived, the atoms may move while still in the excited state. This causes permanent changes in the atomic or molecular structure as a result of the breaking of chemical bonds or cross-linking within organic compounds. C-H bonds common in organic samples are prone to breakage by radiolysis. The hydrogen atom can easily diffuse away, thus hindering the bond from reforming and causing mass-loss of the sample. C-C bonds are not as easily broken and aromatic compounds tend to be less radiation sensitive than aliphatic compounds due to the stability of the conjugated π -electrons. [96] The resonancy between π -electrons allows the energy from inelastic scattering to be distributed between many electrons, leading to less bond breakage. [95] Although knock-on damage also takes place in organic compounds, radiolysis is responsible for most of the damage. Unlike knock-on damage, there is no energy threshold at which radiolysis decreases considerably until the effect becomes essentially unimportant. Instead, there is a gradual reduction in damage effects from radiolysis as the energy of the incident electrons increases. So for organic materials, it can be beneficial to operate the TEM at a higher acceleration voltage to minimise the beam damage effects. [96]

Lowering the temperature of the sample is another way to reduce the damage sensitivity and mass loss in organic compounds since it reduces atomic mobility. Coating the surfaces of the sample with a metal or carbon layer also reduces mass loss since it creates a diffusion barrier which prevents light elements from escaping. [95]

Heating of the sample material is another effect of inelastic scattering which can be especially problematic in many polymer samples since they tend to have low thermal conductivity as well as low softening temperatures. This can lead to a disruption in the specimen caused by the temperature rise not only in the part of the sample directly irradiated by the beam but also in neighbouring areas because of the radial heat conduction. Heating effects can be reduced by reducing the beam current. [96] Similarly, electrostatic charge build-up in poorly conducting materials can cause structural changes or mass transport in the sample as a result of ion drift in the electrostatic field that forms. If the surface potential becomes high enough, it can lead to dielectric breakdown. Large electrostatic forces may even cause mechanical breaking of the sample. [96] Inserting an objective aperture can reduce charging effects in a sample because the secondary electrons generated by the primary electrons hitting the aperture help neutralise the positive charge accumulating in the sample. [97] Adjusting the beam energy so that the number of incoming electrons is the same as the number of emitted electrons (SEs and BSEs) is another way to mitigate charging and is particularly useful in the SEM. [88]

Damage dependency on dose or dose rate

Beam sensitive materials are often divided into two classes based on whether the dominating damage mechanisms are dependent on the electron dose or the dose rate. [98] Dose sensitive materials depend on the total accumulated electron dose, which is the product of the beam-current density, J , and the irradiation time, Δt . [99] A high beam-current density combined with a short recording time could produce similar beam damage as a low current density acting over a long time. There is often a critical dose threshold, D_c , beyond which material structures starts to degrade considerably. The rate of damage can be considered in terms of the fraction of undamaged material along the beam path. Suppose the initial strength of some useful signal (e.g. image contrast) from the complete undamaged sample is S_0 . The remaining signal from undamaged material, S_D , after beam damage at dose D , is given in terms of D_c by $S_D = S_0 \exp(-D/D_c)$. The time, t_c , it takes for the studied signal to reach $1/e$ of its initial value can be used to determine the critical dose according to $D_c = t_c/J$. The critical dose is also material dependent. For polyethylene it is $6.0 \text{ e}/\text{\AA}^2$ while for polycarbonate it is $300 \text{ e}/\text{\AA}^2$, both measured at room temperature, at an acceleration voltage of 100 keV. [99] Radiolysis and knock-on damage are both dose dependent damage mechanisms. [95] Polymers and many other organic materials are often dose dependent. For materials that are dose dependent, the rate at which beam damage occurs is often much larger than the rate of structural recovery. [98]

Dose rate dependent materials, on the other hand, do not depend on the total electron dose but on the energy deposited per unit time. Such materials often suffer damage because of poor conductivity leading to local charging and heating. Better conductive properties would allow the material to recover as these effects can be dissipated. Moreover, this class of materials can be further divided into two groups based on whether the damage increases or decreases with the dose rate. Heating and charging effects are dominant in materials with a direct dose rate effect, such as poorly conducting materials, where the damage per unit dose increases with the dose rate. There is often an associated dose rate threshold beyond which beam damage effects overwhelm relaxation effects, similar to the critical dose discussed for dose dependent materials. Reducing the dose rate below this threshold can make the damage from these effects negligible. Slow diffusion-limited mass loss and precipitation are dominant in materials with inverse dose rate effect, where the damage per unit dose decreases with increasing dose rate. For the second type of materials, it is often beneficial to image the sample with a focused electron probe of higher dose rate, such as in STEM mode, to minimise structural damage. This would not be as beneficial for materials with direct dose rate dependency. [98]

It was recently reported that the critical dose for some conjugated polymers first increases with the dose rate and then decreases. This trend is attributed to diffusion-limited processes. At low dose rates, radiolysis may break off species of free radicals from the side chains that start to diffuse slowly and react with surrounding material. Such slow damage processes show an inverse dose rate dependency and could be outrun by increasing the dose rate. However, as the dose rate increases beyond some threshold value, the damage effects start to follow a direct dose rate dependency. Sample heating leads to a rise in temperature which causes increased diffusion rates that lead to faster damage propagation. By incorporating antioxidants in the sample, the effect of beam damage can be minimised. [100]

3.2.4 Liquid Phase Transmission Electron Microscopy (LPTEM)

Electron microscopy is generally only performed on solid samples because of the difficulties with handling gasses or liquids such as water inside the microscope vacuum. [101] The vacuum levels at the specimen stage in a typical TEM is $\sim 10^{-5}$ Pa while the electron gun area should be kept at $\sim 10^{-5}$ Pa for a LaB6 source down to $\sim 10^{-8}$ Pa for a FEG to ensure good operation of the electron source. [102] Liquid phase transmission electron microscopy (LPTEM) enables the study of liquid samples in the TEM by using a specialised open-cell system with differential pumping or a closed-cell system, such as the ones shown in Figure 3.9, to seal the liquid from the vacuum environment. [101] Open-cell systems require special environmental TEM (ETEM) instruments fitted with a series of pumps and apertures to keep the specimen chamber at a higher pressure than the rest of the instrument. Even though pressures up to 2 kPa can be achieved [103], this is still too low for many common high-vapour-pressure liquids such as water which evaporates at 2.3 kPa - 4.2 kPa at temperatures in the range of 20 °C to 30 °C [104]. Closed-cell systems encapsulates the sample between two electron-transparent windows, bypassing the limitations on the vacuum pressure. This makes the LPTEM technique available for a wider range of liquids. Using liquid cells fitted to standard TEM holders or special TEM holders, the closed-cell approach can be applied to any conventional TEM. [101]

The two most common liquid cell systems are based on silicon (Si) microchips (Figure 3.9a) or graphene microencapsulation (Figure 3.9b). In the Si microchip system, a thin layer of the sample liquid with typical thickness between tens of nanometres up to a few micrometres is confined between two Si microchips separated by spacers and sealed with O-rings. A thin membrane of amorphous silicon nitride (SiN) forms the electron-transparent window. Graphene liquid cells consist

of enclosing a small volume, less than 0.01 pL, of sample liquid between sheets of graphene or amorphous carbon films of a few nanometres. Microfabrication on the Si microchip system allows for liquid flow to study kinematic processes and replenishing the available reactants in the solution, controlling the temperature of the sample via heating or cooling, and applying electrical bias to patterned electrodes on the Si chips. These types of microfabrication opportunities are currently not compatible with graphene liquid cells. [105]

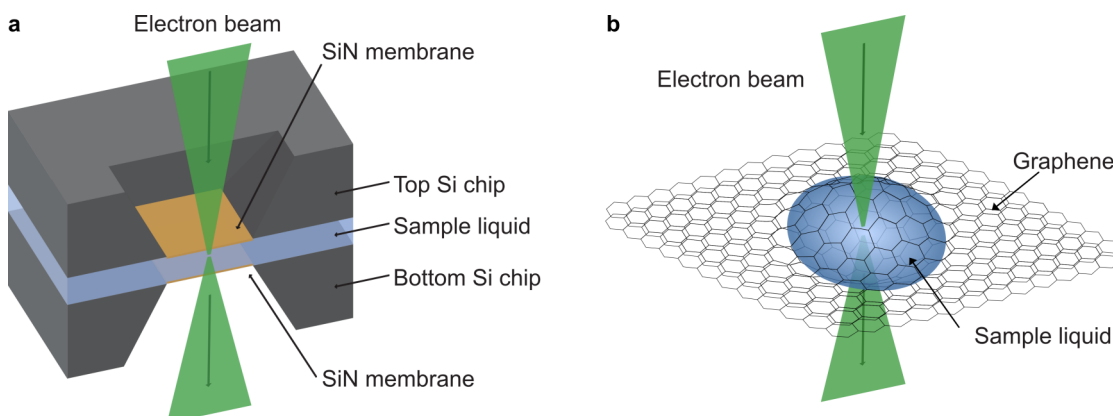


Figure 3.9: Schematic of two types of closed liquid cells for TEM. a) Cross section of a silicon microchip system where a liquid sample is placed between two silicon chips with electron beam transparent silicon nitride windows. b) Graphene liquid cell where the liquid sample is encapsulated between two thin sheets of graphene.

The *in-situ* imaging capabilities of the LPTEM method can provide important insights into the dynamic processes occurring in liquids and allows observation of phenomena such as nanomaterial synthesis [106–109] and corrosion [110], imaging of biological cells [111–114], solid-liquid interfaces in battery electrolytes [115–117] and assembly of hydrated soft matter and polymeric materials [118–121]. This thesis work focuses on using LPTEM to study the morphology of polymeric materials in solutions and the growth of organic nanostructures. Soft matter such as liquids, polymers, gels and biological materials have until recently been particularly challenging to analyse using normal electron microscopy at high vacuum conditions because of the complex interactions between the materials and their surroundings [122]. Cryo-electron microscopy has been used extensively to safely image the structure of these materials, but the technique requires taking the materials out of their native state. The technique also requires freezing of the sample which can introduce damage to the sample or other unwanted artefacts. [105] LPTEM, on the other hand, allows both preservation of the native state and *in-situ* observation of reactions in the materials with high spatial and temporal resolution. [101]

Challenges

There are three main challenges to consider when performing LPTEM experiments: resolution, electron beam-induced effects and damage, and representativeness.

Resolution

LPTEM often suffers from poorer resolution than TEM of solids because of the thick samples used. The electron beam needs to pass through two layers of protective membranes as well as the liquid sample itself. Chromatic aberration of the objective lens caused by inelastic scattering of electrons in the sample is the main limiting factor for the resolution. A thinner liquid layer and thinner SiN windows improves the achievable resolution since scattering is minimised. However, when the liquid cell is placed in a vacuum environment, the pressure difference between the inside and outside of the liquid cell makes the thin windows bulge outwards in the center of the window, increasing the thickness of the liquid layer. Thinner windows are typically less stiff and tend to bulge more. Reducing the size of the window is a more effective way of reducing bulging than changing the thickness of the window material even if it means the viewable area of the sample becomes smaller. [123] Graphene cells can typically achieve better resolution than microchip cells because there is less scattering from the window membrane which can be made thinner, and the liquid thickness is often smaller. However, the liquid volume that can be analysed in a graphene cell is much smaller and the cells are not compatible with functions like electric biasing or liquid flow. [105]

The placement of an object of interest, e.g. nanoparticles, within the liquid also plays a role when it comes to resolution. In TEM, the highest resolution is achieved if the object is placed in the part of the sample where the beam exits the liquid cell. Then the beam will not broaden much more in elastic scattering after interacting with the object. [123]

Beam damage

LPTEM experiments suffer from the same beam damage effects as other TEM experiments, as described in Section 3.2.3, including effects from elastic and inelastic electron scattering in the sample. The most critical beam damage mechanism in LPTEM is radiolysis which can lead to bubble formation and undesired reactions in the sample. Liquids are particularly sensitive to radiolysis which decomposes sample molecules into new radiolytic products that continue to interact with the sample itself or the sample environment in a cascade of reactions. [101] In the case of water, within the first 10 ps of exposure to ionising radiation, the water molecules decompose into solvated electrons (e_h^-), hydrogen radicals (H^\bullet), hydroxyl radicals (OH^\bullet) and hydrogen gas (H_2). Within 1 μ s, these initial species

have participated in further reactions to also produce hydrogen peroxide (H_2O_2), hydronium (H_3O^+) and hydroperoxyl (HO_2^\bullet) [124–127]. This can lead to further changes in the chemistry and structure of the sample and variations in the local pH. [101]

It is often challenging to completely remove the influence of the electron beam on the electrochemistry of the analysed sample, making a desired chemical reactions more difficult to control. At the same time, electron-beam induced radiolysis could be actively used to drive certain chemical reactions. This method has commonly been exploited to study the nucleation and growth of nanoparticles. [101]

The total accumulated electron dose is important in LPTEM since it determines how large a dose the sample can withstand before the sample degradation becomes so large that no reliable structure information can be extracted. The dose rate is also of high significance since it influences the local formation of reactive species through radiolysis. The concentration of radiolytic products increases with dose rate until a steady state is reached. [128]

Beam-induced heating effects are relatively small in LPTEM, but electrostatic charging may occur, especially at the insulating SiN membranes. The charge build-up at the membranes can cause attraction or repulsion of charged species in the sample, inducing particle movement within in the sample liquid. [105]

Since inelastic scattering is the dominant source of beam damage in LPTEM experiments, it is a good idea to operate the microscope at high beam energies in combination with a low dose rate to increase the mean free path in the sample material and reduce scattering. [105]

Representativeness

As previously mentioned, a common issue in LPTEM is the formation of gas bubbles in the liquid layer. This can be caused by interactions with the electron beam at high beam dose or by electrochemical reactions taking place at the electrodes in a biasing experiment. Bubbles can be detrimental since they cause the liquid cell to fill with gas, changing physical surroundings of the sample of interest and alters diffusion pathways. They can also be beneficial since the liquid gets pushed away in regions, leaving only a thin wetting layer on the two membranes which allows for higher resolution imaging. [101] Bubbles can be removed by displacing them away from the viewing area in a system that allows for liquid flow or dissolving the bubbles by increasing the pressure inside the liquid [129]. Bubble formation can also be alleviated by allowing liquid flow which removes free electrons, radicals and excessive heat formed by the electron beam. [130]

Finally, the use of a small, confined volume of solution sets some constraints on

the representativeness of LPTEM measurements. The limited solution volume leads to a limited availability of reactants, in particular in cases where a static volume is used. This can cause the outcome of *in situ* chemical reactions to be quite different from their large-scale counterparts. [105] The physical confinement constraints set by the electron transparent membranes also has an influence since it limits particle growth and maximal sizes achievable compared to particles growing in free space. It can hinder the diffusion of liquid and particles inside the liquid cell. Build-up of surface charge on the inside of the membranes may produce an ordered liquid layer capable increasing the viscosity of the liquid. This can slow down nanoparticle diffusion to nine orders slower than diffusion rates expected in bulk solutions. [131]

3.2.5 Focused Ion Beam - Scanning Electron Microscopy (FIB-SEM)

A focused ion beam (FIB)-SEM is an instrument that can be used to reveal and image the internal structure of materials. It is a dual beam instrument implementing both an electron beam column and an ion beam column focused separately. The typical components of a FIB-SEM instrument are shown in Figure 3.10.

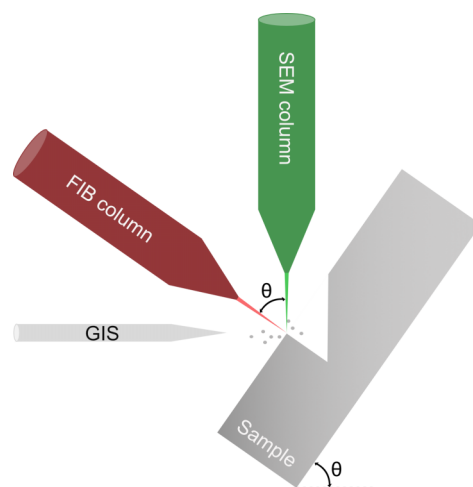


Figure 3.10: Schematic illustration of the typical components in a FIB-SEM. The sample stage is tilted to an angle $\theta \approx 50^\circ - 55^\circ$ so that the ion beam has normal incidence to the sample surface. The FIB column and SEM column are also placed at angle θ relative to each other. This allows the ion beam to perform milling simultaneous to imaging with the electron beam without having to tilt the sample in between operations. A GIS consisting of needles can be used to inject a gas into the specimen chamber.

Electromagnetic lenses are implemented to shape both the ion beam and the electron beam into fine probes that can be scanned across a sample. The ion beam typically consists of heavy ions accelerated to high energies, often using an acceleration voltage of ~ 30 keV. If the ions have sufficient kinetic energy to overcome the surface binding energy of sample atoms they can be used to sputter away, or "mill", atoms from the sample. This allows unwanted material to be removed from the sample to reveal internal structures by cross-sectioning, preparing thin lamellae for TEM analysis, or perform patterning at the nanoscale. A liquid metal ion source (LMIS), commonly consisting of gallium (Ga), is used to generate the focused ion beam. The LMIS can produce an ion beam ~ 5 nm in diameter enabling site specific operation of the FIB with very high spatial resolution. [132] As the ions interact with the sample, they produce secondary electrons that can be detected to form an image of the sample. This image can be compared to the one generated by the electron beam. The FIB and SEM columns are typically tilted at an angle $\sim 50^\circ - 55^\circ$ with respect to each other, as illustrated in Figure 3.10. The precise angle depends on the instrument used. The geometry allows for operating the ion beam and the electron beam simultaneously so that SEM imaging can be performed during FIB milling. [133]

Most FIB-SEM instruments also have a gas injection system (GIS). A precursor gas often consisting of tungsten, platinum, carbon or water vapour is injected via capillary needles placed ~ 100 μm from the sample surface to perform site specific deposition of metals or insulators. The gas molecules are adsorbed on the sample surface everywhere in the vicinity of the GIS needle inlet but the molecules only decompose where the ion beam or electron beam strike the sample. This results in the build-up of material in the region scanned by either the ion beam or electron beam, depending on which one is chosen for deposition. In ion beam assisted chemical vapour deposition, the ion beam current needs to be set carefully to a relatively low value so that sputtering processes do not overtake deposition. Beam currents of 50-100 pA are often sufficient to allow effective deposition without sputtering. [132]

Artefacts and beam damage in the FIB-SEM

Ion-solid interactions are responsible for sputtering, redeposition, ion-induced deposition, resolution and contrast in imaging. These interactions need to be understood to optimise the FIB-SEM operation for each unique sample. The ion beam may introduce artefacts during milling. Common artefacts include curtaining, redeposition of removed material still in the chamber, and charging. Curtaining occurs when a material exhibits different hardness or thickness leading to variations in the ion milling rate. This can be seen as vertical lines in a cross-section

surface. Another common issue is that Ga^+ ions from the beam are implanted in the sample and can generate defects such as amorphisation of crystalline samples. [132] In biological and polymeric sample, the radiolysis and heating caused by the ion beam can lead to changes in phase, chemical composition, morphology and mechanical strength of the sample material including melt-like damage or stiffening of some polymers. Reducing the ion beam current (from 1 nA down to 300 pA) can help minimise these effects. [134–136] However, a lower current means slower milling, so the ion beam current should be chosen to allow for effective milling while avoiding the introduction of artefacts. A common approach to making cross-sections in soft materials is to first perform rapid milling using a high beam current and voltage (up to about 7 nA and 30 keV, respectively) followed by polishing milling at low beam current (~ 0.5 nA) and/or low beam voltage (500 eV to 5 keV) to remove any damaged layer. [134, 136, 137] Heating can be minimised by reducing the beam overlap to avoid cascade collisions. [137]

Deposition of a 1–2 μm thick protective layer of platinum on the surface of the sample prior to FIB milling can also be used to reduce curtaining effects, ion implantation and charging [134, 136, 138]. Often, a thin protective layer (up to ~ 500 nm thick) is first deposited using the electron beam prior to ion beam deposition since the former process is less harsh and does not induce ion implantation. Non-conducting samples may also benefit from sputter coating with 10–20 nm of gold before introduction to the FIB-SEM to avoid sample charging during imaging. [137]

3.2.6 Atomic Force Microscopy (AFM)

Atomic force microscopy (AFM) is a type of scanning probe microscopy that gathers information about the surface of a sample by scanning over it with a mechanical probe. The probe is equipped with a sharp tip often made from Si or Si_3N_4 , approximately 10–20 nm in diameter, attached to a cantilever (see Figure 3.11). The tip traces the surface contour of a sample to image the topography. This makes the AFM a very useful high-resolution profilometer. AFM can also be used to measure properties such as adhesion strength, mechanical strength and stiffness, magnetic and electric force gradients, surface potentials, or the conductivity of a sample. In addition, AFM can be used for nanomanipulation by changing sample properties in a controlled way. AFM can be used to image most types of materials, including metals, semiconductors, polymers, ceramics, glass, and biological samples. [139, 140]

The working principle of an AFM is that the nanometer sharp tip is raster scanned over the surface of a sample. Alternatively, the sample can also be moved under

a stationary tip. At close proximity to the surface, the tip will be affected by forces from the sample which deflect the cantilever a certain distance from its equilibrium position given by Hooke's law $F = -kz$, where F is the force, k is the stiffness of the cantilever and z is the distance the probe is deflected. The force between sample and tip can therefore be calculated by measuring the deflection of the cantilever. Attractive forces cause a deflection towards the sample whereas repulsive forces deflect the probe away from the sample. Note that if the probe is too far away, the force from the sample becomes negligible. The movement of the cantilever is measured by reflecting a laser beam on the back of the cantilever and collecting the reflected beam with a photodetector as shown in Figure 3.11.

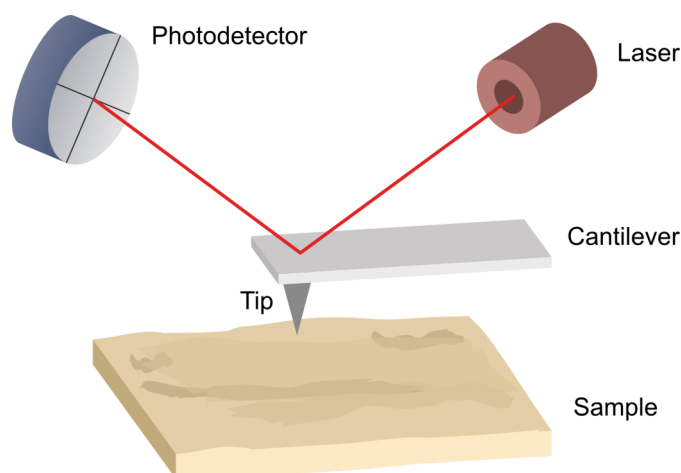


Figure 3.11: Schematic illustration of an AFM. The tip and cantilever is scanned over the surface of a sample. Forces between the sample and tip deflects the cantilever in the vertical direction. A laser is reflected off the back of the cantilever into a photodetector to measure the amplitude of the deflection.

Operation modes of AFM

There are two main modes of operation for AFM: contact mode and dynamic mode. In contact mode, the AFM tip is in contact with the sample surface and "dragged" across it during scanning. The deflection of the cantilever is kept constant (corresponding to constant force) by adjusting the relative height between tip and sample in a feedback loop. The measured deflection of the cantilever as a result of a change in topographic height in the sample is compensated by adjusting the tip-sample distance so that contact is maintained. Soft materials may easily be damaged as the tip is dragged across the surface, so contact mode is mostly used for hard materials. Dynamic mode uses a vibrating cantilever oscillating at a certain frequency close to resonance, placed just above the sample surface. The

sample topography produces changes in the oscillation frequency or amplitude of the cantilever, which is used to adjust the distance between tip and sample. Dynamic mode is further divided into non-contact mode and dynamic force mode. In non-contact mode, the tip never touches the sample. In dynamic force mode, also known as "tapping mode", the tip intermittently touches the sample at the lowest point in the oscillation. Changes in the amplitude, frequency and phase of the oscillation give information about sample topography and material properties causing phase shifts. Tapping mode minimises the friction and force applied between the tip and the sample and is often preferred for soft, fragile materials or samples weakly adsorbed to a substrate, especially if the surface roughness is high. [140, 141]

Resolution and comparison to other techniques

The resolution in AFM is usually defined in the vertical and lateral direction separately. Resolution along the vertical axis can be as high as 100 pm and is determined by the AFM noise floor measured as the motion of the probe when the AFM is not scanning. The resolution along the lateral axis can reach approximately 1 nm and is mainly limited by the diameter of the tip. [140]

Unlike electron microscopes, AFM provides direct information about the three-dimensional profile of a sample surface. It is also able to analyse non-conducting samples without the need for a conducting metal coating that may alter the sample and does not need to operate under high vacuum. However, AFM is more limited than SEM when it comes to the area and height variations that can be imaged. The maximum heights that can be imaged in AFM is on the order of micrometers whereas SEM has a millimetre sized depth of field. SEM can also image areas of square millimetres in size but the maximum scanning area of an AFM is roughly 150 μm by 150 μm . [142]

3.2.7 Sample Preparation for Electron Microscopy

OECTs

OECTs were prepared for SEM imaging of the surface morphology by placing silicon chips with fabricated devices onto aluminium SEM stubs with double-sided conducting carbon tape. Conducting copper tape was placed between the contact pads on the chips and the aluminium stub to ensure proper conductive pathways from the sample to ground.

OECT samples that would be used for cross-sectioning with a FIB-SEM instrument

to reveal the internal microstructure were sputter-coated with 30 nm of gold to increase the conductivity and minimise damage to the surface of the polymer film during milling. The gold layer was deposited with a Leica EM ACE600 sputter coater.

Monomer solutions

To study the aggregation behaviour of ETE monomers, three sets of ETE monomer solutions consisting of pure ETE-S (ETE-S 100%), pure ETE-PC (ETE-PC 100%), or ETE-S and ETE-PC mixed at equal ratios (ETE-S:PC 50:50) at a concentration of 5 mM were prepared by dissolving dry monomer powders into DI water with 10 mM NaCl.

The electrochemical properties of the prepared solutions were analysed with CV to ensure the representativeness of the samples. For structural characterisation with LPTEM, a static volume of each solution was introduced into the TEM instrument by dropcasting 0.6 μL of the solution into the Nano-Cell of a DENSsolutions Stream Liquid Biasing holder.

After TEM experiments, the Nano-Cell with the studied monomer solution - ETE-S 100%, ETE-PC 100% or ETE-S:PC 50:50 - was removed from the TEM holder and opened, allowing the water to evaporate at ambient conditions. The bottom chips of the Nano-Cells with the dried monomer solutions were then secured to an SEM holder for SEM imaging of the dried solutions.

Hydrogels

Freeze dried HA-BCN/PEG hydrogel samples with 0, 5, 10, and 20 mg mL^{-1} PETE-S were placed on conducting double-sided copper tape on aluminium stubs for SEM imaging. The non-conductive HA-BCN/PEG hydrogel with no PETE-S was sputter coated with a 5 nm thick gold film to prevent charging during imaging with secondary electrons in the SEM. The hydrogels with added PETE-S polymer were intrinsically conductive and did not require sputter coating for SEM imaging of surface structures.

After SEM imaging, an additional 200 nm thick sputter-coated gold layer was deposited on all hydrogel samples to enhance the conductivity of the surface before introduction to the FIB-SEM instrument that was used to reveal the internal microstructure.

3.2.8 Detailed Information About the Instruments and Techniques Applied in This Thesis

All structural characterisation was performed at the Chalmers Materials Analysis Laboratory and Myfab LIMS - Nanofabrication Laboratory at Chalmers.

SEM

Structural characterisation with SEM of dried monomer solutions, OECTs and hydrogels was performed using a JEOL JSM 7800F Prime operating at acceleration voltages in the range 1-20 keV at high vacuum conditions. The SEM is equipped with a Schottky type field-emission gun as electron source.

TEM

LPTEM imaging of ETE monomers in solution was performed on an aberration corrected FEI Titan 80-300 operating at 300 keV equipped with a Schottky field-emission gun. TEM analysis was carried out primarily using BF imaging complemented by inspection of DPs to identify the presence of crystalline regions in a sample.

A DENSsolutions Stream Liquid Biasing holder for FEI instruments was used for all LPTEM studies. The holder uses a Si microchip system consisting of a pair of Si chips called the "Nano-Cell" to hold liquid samples. The holder supports pressure-driven flow of liquid into the Nano-Cell which allows the user to control the thickness of the liquid layer as well as drop-casting a static volume into the Nano-Cell prior to assembly. The drop-casting method was used for all LPTEM work in this thesis. The bottom chip of the Nano-Cell is patterned with Pt electrodes for biasing in a three-electrode configuration to mimic a typical electrochemical cell. The thickness of each amorphous SiN membrane in the window region is 50 nm. The thickness was chosen to maximise the achievable resolution, down to nanometre-scale resolution, by minimising scattering from the membranes while also maintaining good stiffness to reduce window bulging and thereby minimising the liquid thickness. At 1 bar pressure, the liquid thickness contribution owing to bulging of the windows is expected to be maximum 300 nm. [129]

Alignment of the microscope was carried out using a standard TEM holder with a sample of dried ETE-PC monomer solution on a TEM grid with holey carbon. After proper alignment, the holder was switched to the DENSsolutions holder with the liquid sample of interest. This was performed for each analysed sample to minimise electron beam exposure on the liquid sample.

CV

CV measurements on monomer solutions were carried out by drop-casting 0.6 μL of the relevant solution onto a micro-electromechanical system (MEMS) device consisting of a SiO_2 chip fabricated to have the same dimensions as the bottom chip of a DENSsolutions Nano-Cell with Pt electrodes in the same geometry. This MEMS chip could be fitted in the tip of the DENSsolutions Stream Liquid Biasing holder and contacted with the electrical probes of the holder.

CV measurements were carried out in the voltage range from -0.3 V to +0.7 V using a potential step size of 0.2 mV and a scan rate of 100 mV s^{-1} for a total of five cycles. The parameters of the CV measurements were controlled and data acquired using the software IviumSoft.

FIB-SEM

FIB cross-sectioning of OECTs and hydrogels to reveal the internal microstructures and information about sample thickness was carried out using FEI Versa3D and Tescan GAIA3 FIB-SEM instruments. The ion current and voltage was selected for efficient milling while also minimising the damage to the sample material as described in Section 3.2.5.

Prior to FIB milling of OECT transistor channels, a 2 μm thick protective strip ($45 \mu\text{m} \times 2 \mu\text{m}$) of platinum was deposited on top of the gold layer at the selected milling site. The Pt layer was deposited by electron beam deposition followed by ion beam assisted chemical vapour deposition using the GIS of the FIB-SEM instrument. The Pt layer was deposited in multiple shorter steps to minimise damage to the sample and avoid drift effects during long depositions. A first thin ($\sim 200 \text{ nm}$) Pt layer was deposited by the electron beam operating at 1 kV, 1.9 nA. Another 500 nm of Pt was deposited after changing the electron beam conditions to 1 kV, 4.0 nA. Finally, $\sim 300 \text{ nm}$ of Pt was deposited with an electron beam at 2 kV, 4.0 nA. This was followed by approximately 1 μm of Pt deposited with an ion beam operating at 30 kV, 50 pA, yielding a final Pt thickness of roughly 2 μm . This layer is deemed sufficient to protect the surface structure as previously discussed in Section 3.2.5. Cross-sectioning of OECTs was carried out by milling an initial trench 42 μm long and 10 μm wide along the length of the transistor channel. The length of the cross-section was chosen to contain both Au electrodes and the gap between the electrodes. Rough milling was carried out with an ion beam operating at 30 kV, 3.0 nA. This was followed by cleaning cross sections at 30 kV, 0.5 nA and 16 kV, 0.5 nA. Final polishing was carried out at 10 kV, 0.5 nA.

Hydrogel samples were also protected by 2 μm thick strips of Pt, analogous to the

OECT samples, before FIB milling. Cross-sectioning of freeze-dried hydrogels was performed by milling an initial trench, ca 500 μm long using rough milling at 30 kV and 7 nA. This was followed by milling at successively lower beam energies, at 15 kV, 10 kV and 5 kV and decreasing beam currents from 4.0 nA down to 0.5 nA to obtain a final polished cross-section with minimal artefacts.

AFM

AFM measurements on OECT surfaces were performed on a Bruker Dimension Icon AFM operating in tapping mode. Image data was acquired using the latest NanoScope software and analysed with Gwyddion 2.66.

4 Results and Discussion

In this chapter, the results from the structural characterisation with electron microscopy and AFM of organic electronics for neuro-pharmaceuticals are presented and discussed. The structures of these materials and devices are shown and correlated to relevant device properties along with implications for their use in *in vivo* manufacturing of bioelectronics in brain tissue. Three principal systems have been studied, each one represented in a separate research paper included in this thesis. Section 4.1 investigates the nanostructure evolution of electropolymerised transistor channels in OECTs. Section 4.2 investigates the aggregation behaviour of ETE monomers in electrolyte solutions used in the fabrication of OECT devices and conducting hydrogels. Finally, the microstructure of the conducting hydrogels is discussed in Section 4.4.

4.1 Structural Evolution of Conducting Polymer Films in OECTs

The micro- and nanoscale structures of thin polymer films acting as transistor channels in OECTs have been investigated in this thesis. Conducting polymer films grown from 1 mM ETE-S solutions via electrochemical polymerisation were characterised using SEM secondary electron imaging and AFM techniques. An electric voltage of 0.50 V was applied to the drain electrode for different amounts of time (2 s, 30 s, 60 s or 120 s) to polymerise the monomers in the NaCl electrolyte solutions during film fabrication. The voltage was chosen to be approximately 0.20 V above the reported oxidation threshold for ETE-S monomers [14] to ensure efficient polymerisation. The structure and properties of these devices are reported in Paper I and presented here.

4.1.1 Nucleation of the Polymer Film

SEM imaging of the surface morphology of the PETE-S films in the OECT devices reveals that nucleation of material starts at the positively biased drain electrode (white arrows in Figure 4.1). In contrast, no nucleation is found on the grounded source electrode.

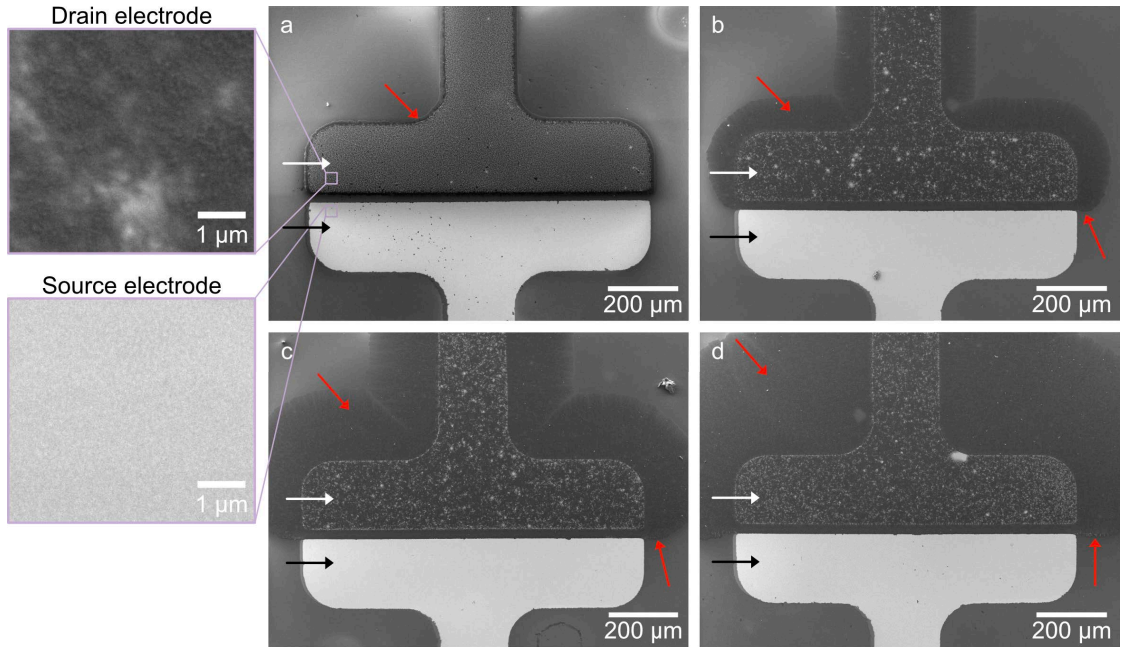


Figure 4.1: Spreading behaviour of PETE-S films for OECT transistor channels. SEM images recorded at 2 kV of PETE-S films polymerised by a drain voltage of 0.50 V applied to the top electrode in each image for a) 2 s, b) 30 s, c) 60 s, d) 120 s. Nucleation of the polymer film starts on top of the drain electrode (white arrows). The polymer film extends laterally (red arrows) from the drain with time. The source electrode (black arrow) was kept grounded. No polymer film growth is found on the source electrode. The insets on the left show the morphology on top of the drain electrode and source electrode at a higher magnification.

When the ETE-S monomers at the drain electrode surface in the electrolyte solution are subjected to a polymerising electric voltage of 0.50 V they get oxidised and start to form polymer chains. The negatively charged polymer chains adhere to the positively biased electrode surface. Monomers in the surrounding solution are also subject to a polymerising bias given that they are close enough to the biased electrode. The distance above the electrode surface where the local potential is high enough to oxidise the monomers is influenced by the Ohmic drop in the electrolyte. After the initial nucleation of the first layer of polymer film, monomers

in the electrolyte solution above this layer also undergo oxidation. As the polymer chains in the solution get longer, they eventually become insoluble and adhere to the already deposited polymer film. This results in a both lateral and vertical film growth.

4.1.2 Film Evolution

Lateral spreading of the film

Figure 4.1 demonstrates how the film evolves after the initial nucleation stages. Growth of the polymer film starts at the drain electrode (white arrows), spreads out laterally (red arrows) and continues towards the grounded source electrode (black arrows) as the growing channel closes the gap. This behaviour of film growth extending from the positively biased electrode towards a grounded electrode has previously been reported for PETE-S films grown by electropolymerisation on APTES treated substrates. [14] The relative area covered by the PETE-S polymer film increases with time, as shown in Figure 4.2. The polymer film areas are calculated from the SEM images in the same figure.

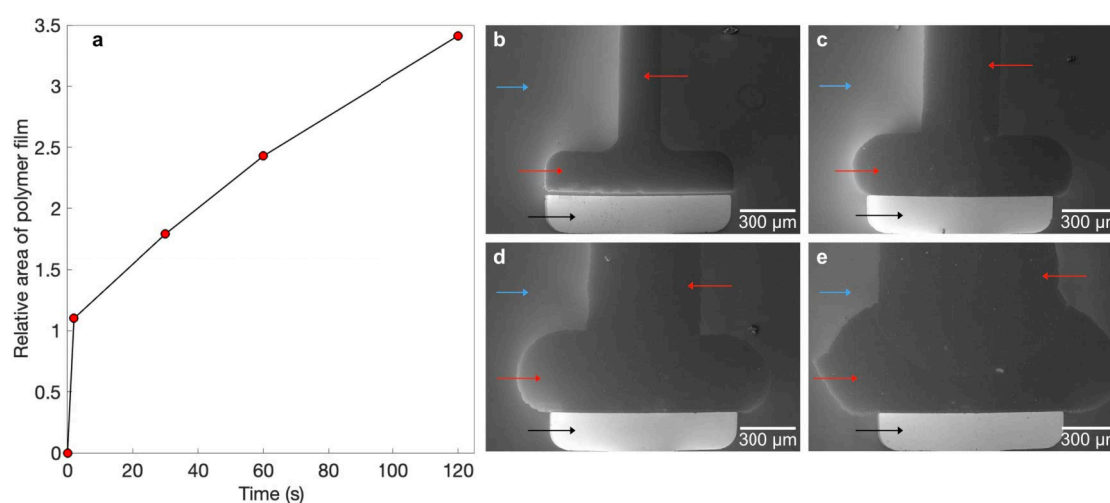


Figure 4.2: Area covered by the PETE-S film. a) Relative film area as a function of time. The relative areas in the graph are the ratio between the areas covered by the polymer film and the area of the drain electrode. At time zero there is no film growth yet. The area covered by the polymer film for each time was calculated from the SEM images on the right. b)-e) SEM images recorded at 1kV of PETE-S film at b) 2 s, c) 30 s, d) 60 s, e) 120 s. Each image shows a 1600 μm x 1100 μm region containing the source electrode (black arrows), drain electrode with grown polymer film (red arrows) and surrounding substrate (blue arrows).

The increase in polymer film area mainly comes from lateral spreading on top of the APTES treated SiO_2 substrate. Minimal film formation takes place on the grounded source electrode, as can be inferred from the SEM images in Figure 4.1 and Figure 4.3 that shows a higher magnification view of the gap region.

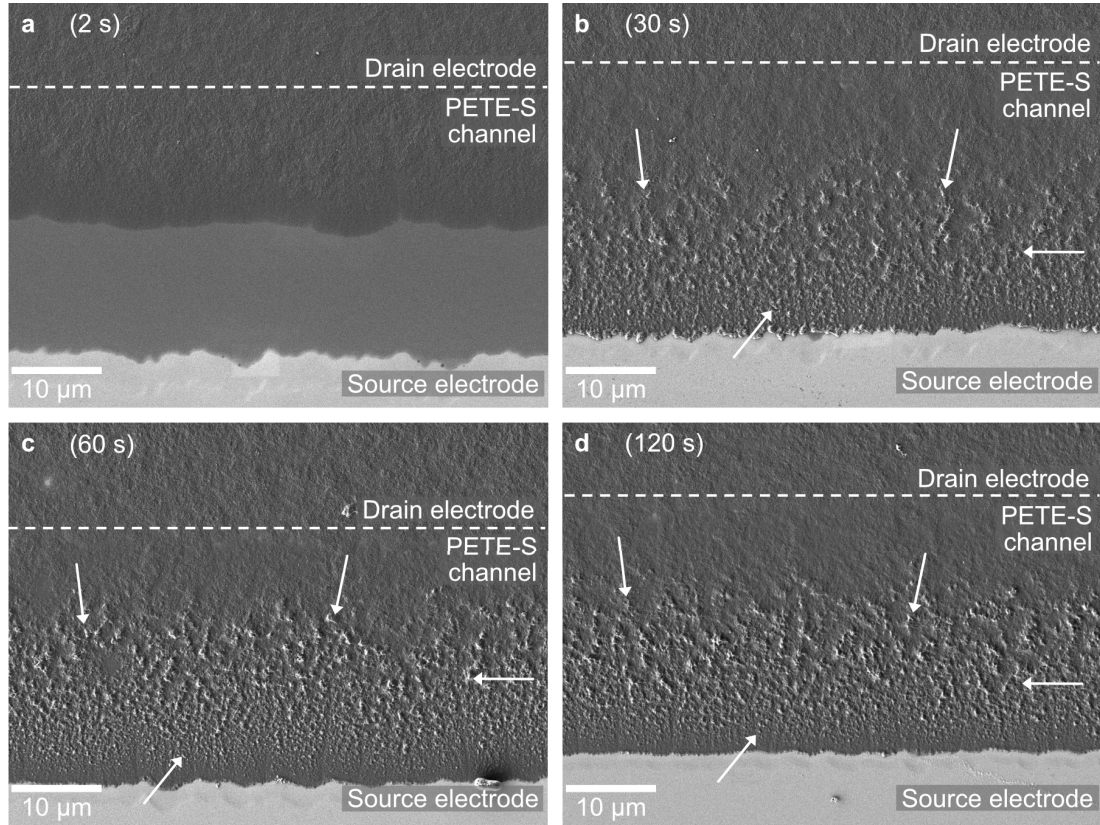


Figure 4.3: Time evolution of the PETE-S film in the OECT transistor channel. SEM images at 1 kV showing the surface morphology of the film in the gap between the two electrodes. The images show the film after a) 2 s, b) 30 s, c) 60 s, and d) 120 s. The approximate position of the drain edge is marked by the dashed line in each image. The source electrode is grounded. Two distinct surface morphologies can be observed: a smooth surface in the upper half of the film by the drain electrode and a rough surface in the lower half of the film, closer to the source electrode. Areas of bright contrast (white arrows) in the rough part of the film originate from clusters of particles at or near the film surface.

The APTES surface modification of the SiO_2 substrate plays an important role in the lateral spreading of the polymer film along the substrate. The APTES treatment yields a slightly positively charged surface that promotes accumulation

of negatively charged ETE-S monomers near the substrate surface in the electrolyte solution. This has previously been demonstrated by molecular dynamics simulations. [14] A dense layer of higher local monomer concentration likely forms in proximity to the modified substrate. The concentration of monomers near the surface facilitates mass transfer and lateral film growth. Polymer spreading on untreated SiO_2 surfaces or plasma cleaned negatively charged surfaces, on the other hand, is minimal. This is likely due to electrostatic repulsion between the negatively charged substrate surface and the negatively charged side chains of the monomers.

After polymerising the monomer solution for 2 s, the PETE-S film has grown approximately halfway across the 30 μm long channel (Figure 4.3a). At this time the conducting polymer film has not yet created electric contact between the two electrodes. At 30 s, the film has spread all the way to the ground electrode, which can be seen in Figure 4.3b. These observations are in line with the drain currents, I_D , measured at the four different film growth times during device fabrication (see Figure 4.4).

Since $V_G = 0$ V during the fabrication of the polymer films, I_D is determined by the intrinsic conductance of the transistor channel. The drain current begins to increase significantly after approximately 4-7 s. The rise in drain current at this time signifies that the polymer film has created a conductive pathway between the source and drain. Namely, electrical contact between the two electrodes is first established at a time between the 2 s and 30 s film morphologies shown in Figure 4.3. The exact time when the current starts to increase varies a bit between different devices with the same fabrication parameters. This is a result of the reproducibility problem for these OEECT devices caused by both the unpredictable nature of the electropolymerisation reaction and the quality of the APTES surface treatment. It can also be noted that I_D is not initially zero (at $t = 0$ s) which indicates that the substrate is not completely insulating. Moreover, there is a sharp drop in the I_D at the end of the allotted time for polymerising bias. This change in current is a result of a capacitive negative current caused by the sharp change in potential of the drain electrode when the drain voltage is switched from $V_D = 0.50$ V to $V_D = 0$ V.

After 4-7 s (red arrows in Figure 4.4), the drain current increases with time in a logarithmic manner until the polymerising bias is turned off. In comparison, the increase in the area covered by the film during the same time is more linear in nature. The percentage increase of the two properties relative to their values at time $t = 2$ s is shown in Figure 4.5. The mean drain current is approximately 25 times higher at $t = 120$ s compared to the current at $t = 2$ s, whereas the area covered by the polymer film has only increased by a factor of three. The

discrepancy between these results suggests that the growing area of the polymer film is not the only contributor to the rising drain current. The drain current is also influenced by the contact area between the polymer film and the source electrode, the film thickness and surface roughness, and the density of charge carriers in the film.

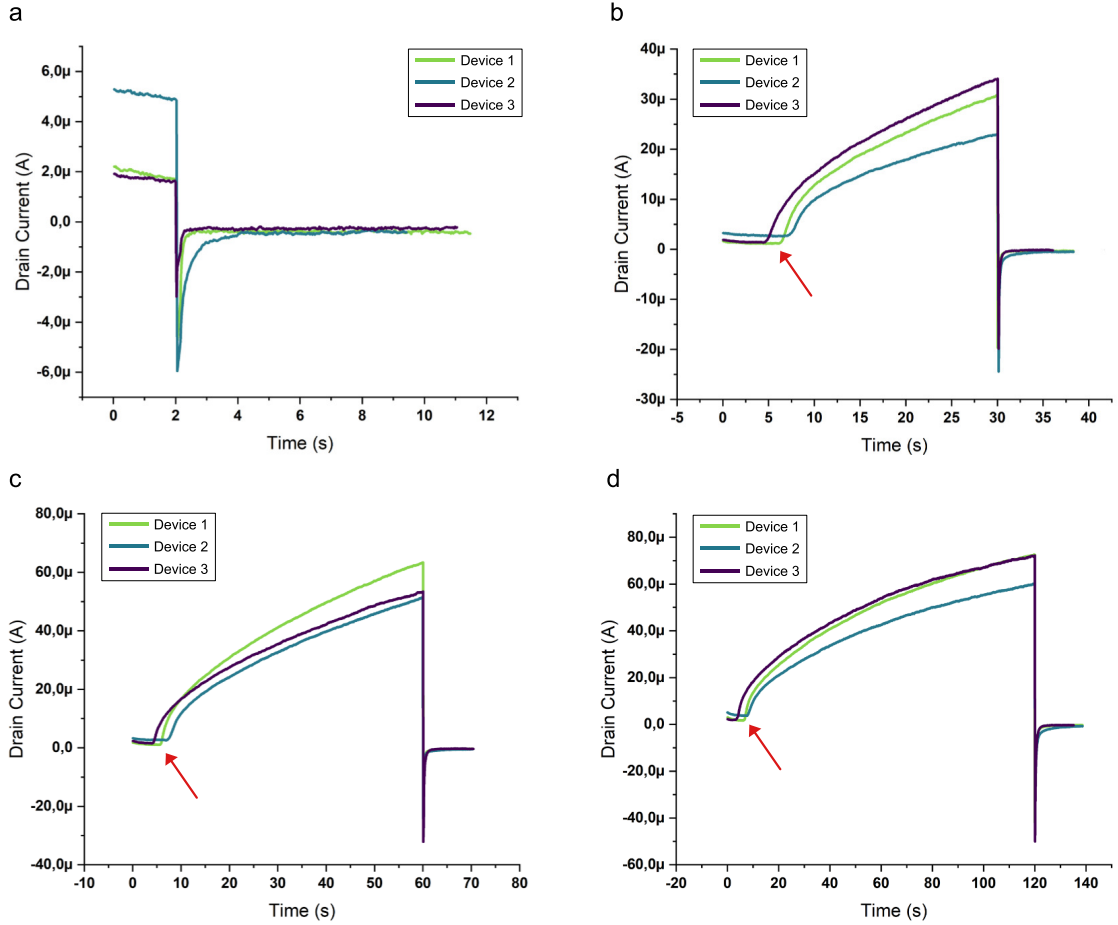


Figure 4.4: Electrical characterisation of OECT devices. Measured drain current, I_D , as a function of time during device fabrication. In the graphs, a drain voltage $V_D = 0.50$ V is applied for a total time of a) 2 s, b) 30 s, c) 60 s and d) 120 s. This was followed by $V_D = 0$ V until the current stabilised. The drain current starts to increase significantly after approximately 4-7 s, marked by red arrows. This indicates the point where the conducting polymer film makes electrical contact with the grounded electrode. Triplicates of each sample were fabricated to investigate the reproducibility.

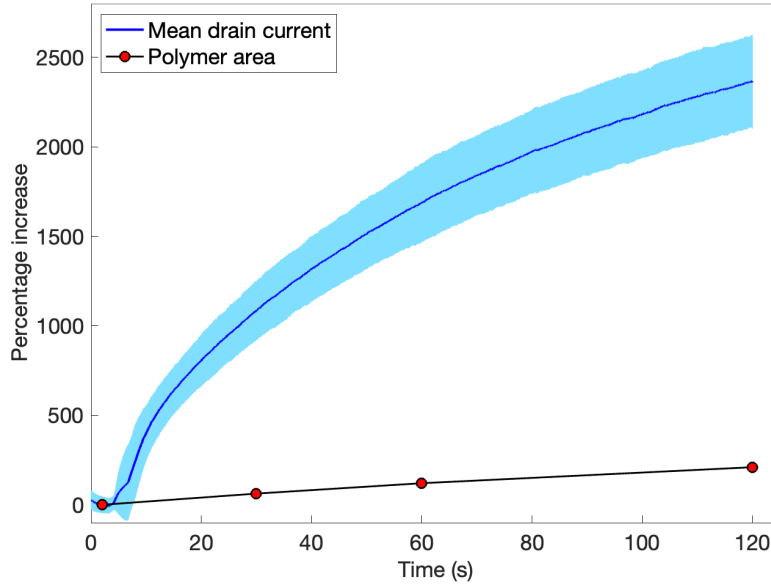


Figure 4.5: Percentage increase of drain current and polymer area as a function of time. The percentages are calculated relative to the values at the time 2 s. The mean (blue line) and standard deviation (shaded area) of the drain current measured for three devices are shown. The drain current increases much more rapidly than the area covered by the polymer film.

To gather more information on the film thickness and the contact area between the polymer film and the source electrode, cross sections of the polymer films were prepared using a FIB-SEM instrument. These cross sections were cut along the length of the transistor channel to observe variations in film thickness along the channel and to determine how far the polymer film extends onto the source electrode. After 30 s of growth, the film extends roughly 300 nm beyond the electrode edge before terminating abruptly, see Figure 4.6. Even after 60 and 120 s, the polymer film still only reaches about 300 nm over the electrode edge. This means that the contact area between the PETE-S film and the source electrode remains constant over the studied growth periods.

Thickness and surface roughness of the polymer film

As described in Section 2.3.1, the electrical properties of the OECT device depend not only on the surface area of the transistor channel, but also on the thickness and uniformity of the polymer film in the channel since all the material can participate in ionic and electronic conduction. The cross-sectional view of the 30 s channel

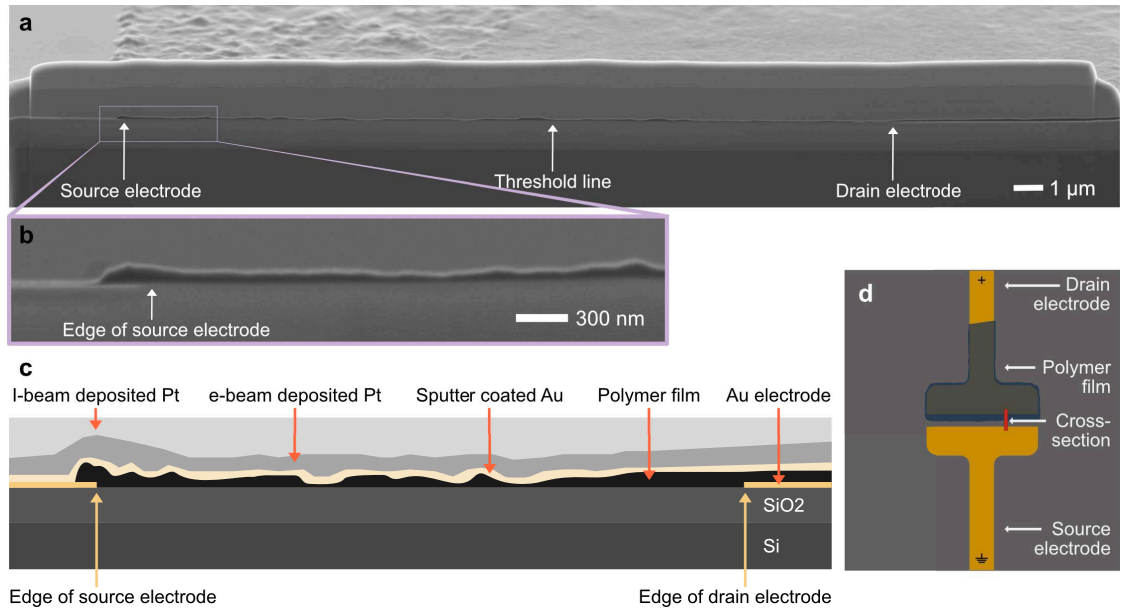


Figure 4.6: Cross sectional view of the polymer film grown for 30 s. a) SEM image recorded at 1 kV showing a FIB cross section. The thin, dark layer in the middle of the image is the polymer film. The film thickness varies along the length of the gap. The average film thickness is estimated to be 80 nm and the maximum thickness is measured as 210 nm in the gap region. The edge of the ground electrode (left arrow), positive electrode edge (right arrow), and approximate position of the threshold line (middle arrow) where the surface morphology starts to show a significant increase in roughness are all marked. b) Higher magnification image of the polymer film by the source electrode edge. c) Schematic illustration of the different regions of the FIB cross section (not to scale) identifiable by changes in contrast in the SEM image. d) Schematic showing the placement of the cross section in the OECT device.

in Figure 4.6 can be used to determine the thickness and surface roughness of the polymer film. It is evident that the thickness of the polymer film is not uniform but varies along the length of the transistor gap due to a high surface roughness. The polymer films grown for 60 s and 120 s showed similar features. The surface of the polymer film grown for 2 s, on the other hand, was much more smooth and the thickness of the film decreased with distance from the drain electrode. A more uniform film was observed on top of the drain electrode compared to the film in the gap region for all samples. A uniform film thickness on the biased drain electrode can be expected since the electric potential in this region should be uniform at 0.50 V. The film thickness reached its highest values in the gap region, with a maximum thickness of approximately 200 nm after 120 s of growth. This

maximum thickness of the film is small in comparison to the lateral extension of the film. After 120 s, the film had spread several hundred micrometers horizontally beyond the drain electrode edge. This preferential lateral growth is attributed to the APTES treatment of the surface.

It should be noted that the FIB cross sections only provide single line profiles of the polymer film along the length of the channel. To extract information about the two-dimensional surface topography of the whole polymer channels, AFM imaging was performed. The AFM images are presented in Figure 4.7.

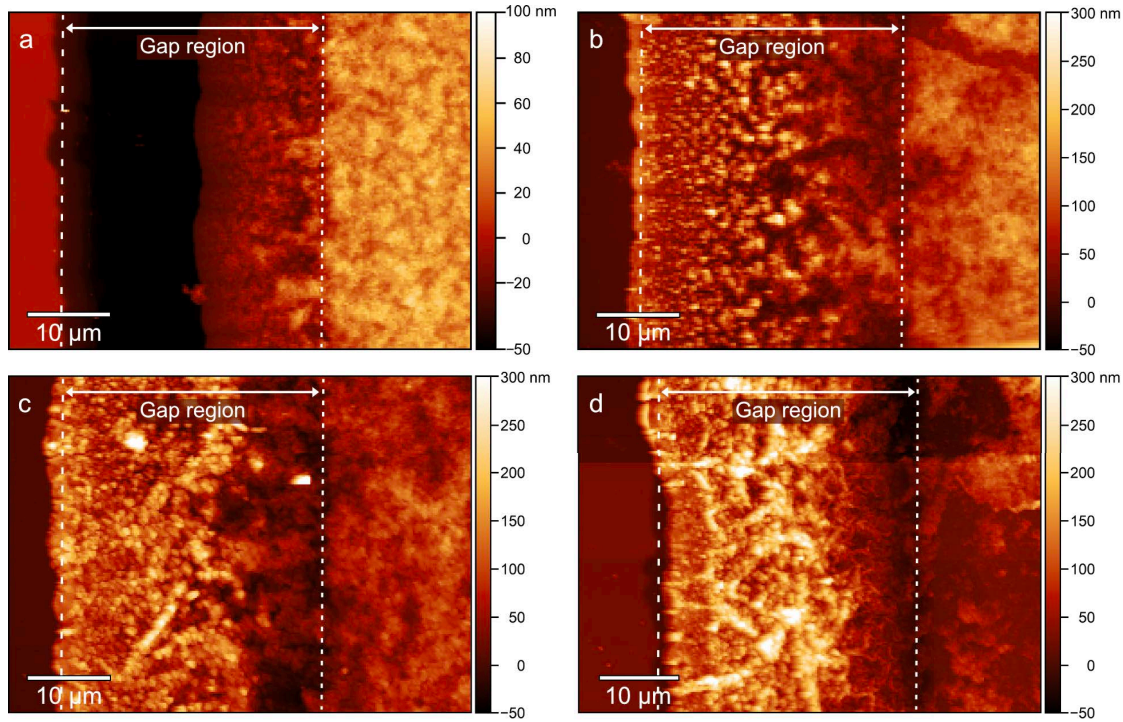


Figure 4.7: AFM images of the PETE-S channels grown for a) 2, b) 30, c) 60, and d) 120 s. The images show height information. The scan size is $55\ \mu\text{m} \times 40\ \mu\text{m}$. The gap region is marked between the two dashed lines at the electrode edges. The height of the source electrode (furthest left part in each image) is set to 0 nm through data levelling by mean plane subtraction on the electrode and setting the plane to zero. The same colour scale bar is applied to all images except a).

The film thicknesses can be extrapolated from the results in Figure 4.8. The graph shows the sample heights measured by AFM, with the zero-level set at the SiO_2 substrate. The sample height is reported as the height of the top surface layer relative to the zero-level. For the film growing directly on the SiO_2 substrate, the

film thickness and reported sample height are thus exactly the same. For the film growing on top of the electrodes, the height of the electrode needs to be subtracted to find the absolute film thickness.

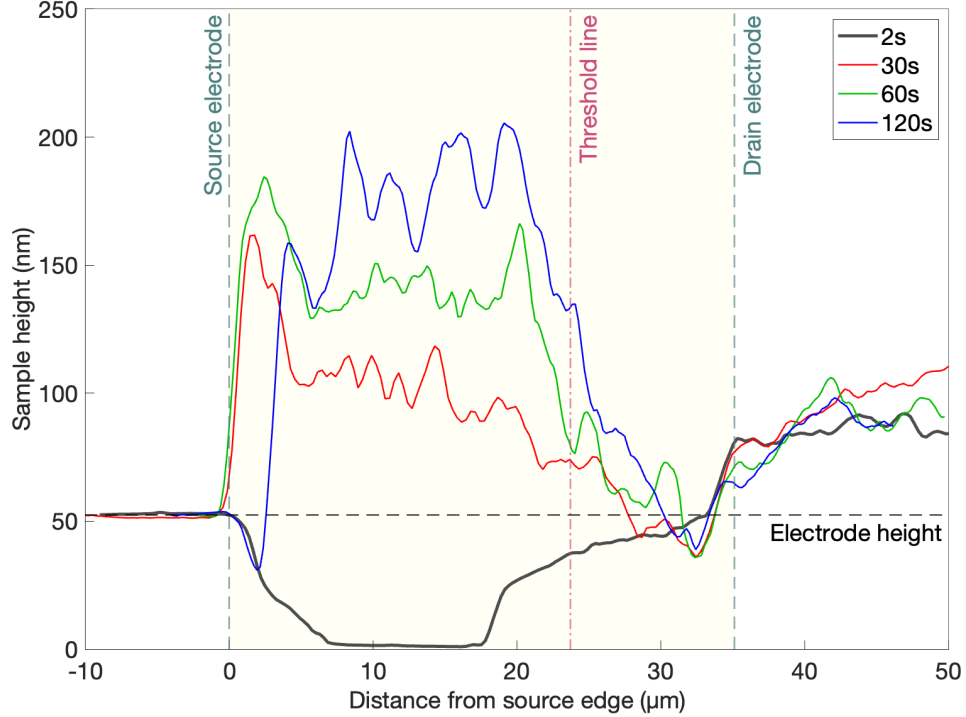


Figure 4.8: Average sample height measured by AFM as a function of distance from the edge of the source electrode for OECT channels at four different times. Large variations in polymer film thickness are found in the gap region between the electrodes, highlighted in yellow. The zero-level is set at the height of the SiO_2 substrate. The edges of the source and drain electrodes are marked with dashed lines. The threshold line marks the position where the surface morphology changes from smooth to rough, similarly to Figure 4.10.

The thickness of the electrodes can be determined from the topographic information of the 2 s channel by the source electrode edge in Figure 4.8. In this region, the sample height decreases from 51.5 nm to 0 nm with a plateau at 20 nm suggesting that the electrode is comprised of two layers with thickness 20 nm and 31.5 nm, respectively. The two levels of the source electrode can also be seen in the SEM images of Figure 4.3 and are assumed to originate from imperfect alignment of the evaporation mask used during the metal electrode fabrication. In Figure 4.8, the edge of the source electrode is set at the edge of the top layer. Both the source electrode and the drain electrode are assumed to have the same

thickness of approximately 50 nm. Based on this assumption, the thickness of the polymer film on top of the positively biased drain electrode is found to be in the range of 20 nm to 60 nm at all four times. The film thickness in this region does not change substantially with time. The RMS roughness measured by AFM (see Figure 4.9) of the film on the drain electrode is 10 nm after 2 s of film growth and increases to approximately 30 nm after 30 s and longer growth times. The variations in film thickness show that the sample surface is not entirely smooth despite the application of a uniform electric potential. In general, the film thickness values measured by AFM (Figure 4.8) are in accordance with the ones measured in the FIB cross section in Figure 4.6, indicating that the FIB has not introduced artefacts or damaged the top layer of the material.

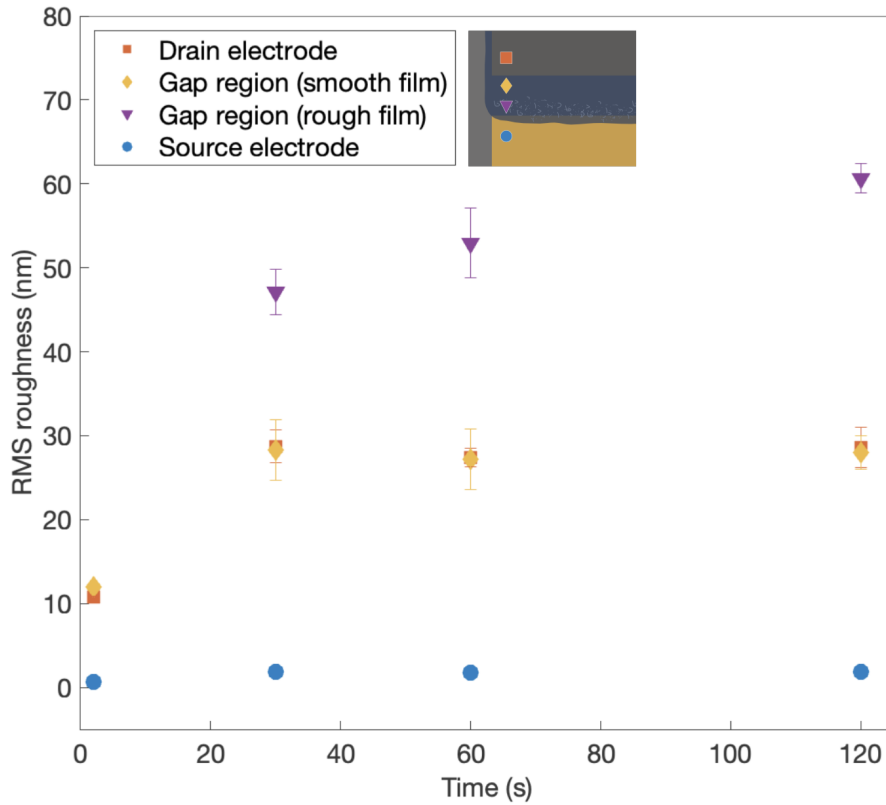


Figure 4.9: RMS roughness determined by AFM as a function of time and location. The mean value of the surface roughness are displayed for the source electrode, the polymer film in the smooth and rough part of the gap region and the polymer film on the drain electrode. The error bars represent the standard deviation of the value.

Thickness of the polymer film in the gap region and the shape of the electric field

The film thickness in the gap region between the electrodes (yellow highlight in Figure 4.8) show more pronounced variations compared to the film on the drain electrode. The film thickness changes with distance from the drain electrode and increases with time at each position. At short biasing times (2 s), when the polymer film has not grown all the way across the gap, the film thickness decreases with distance from the drain edge.

Two types of surface morphologies can be identified in the gap region. Firstly, a film with smooth surface morphology adjacent to the drain electrode. This part of the film has a similar RMS roughness as the film on the drain electrode. Secondly, at a distance of about 10 μm from the drain electrode edge, the film has a rough surface morphology. The RMS roughness in this part of the film reaches up to 60 nm after 120 s. The two surface morphologies are obvious in the SEM images in Figure 4.3b-d and Figure 4.10. Note that the rough surface morphology is observed for films grown for at least 30 s.

The conducting polymer film functions as an extension of the biased drain electrode. As the film spreads laterally towards the grounded source electrode, the effective position of the drain electrode edge shifts closer to the grounded source electrode. This movement alters the electric field distribution in the device channel as the film advances. While the film is growing towards the grounded electrode, the electric potential within the conducting polymer remains equal to that of the drain electrode. However, once the film spans the entire channel and contacts the source electrode, an electric current will flow through the film. This causes the potential to vary within the film, ranging from 0.50 V at the drain electrode to 0 V at the source electrode.

At a certain distance from the drain electrode, the local potential within the film drops below the 0.30 V threshold required to polymerise the ETE-S monomers. This threshold potential is associated to the observed change in surface morphology approximately 10 μm from the drain edge. In areas where the local potential falls below 0.30 V (to the left of the threshold line in Figure 4.8) the channels at 30, 60, and 120 s all exhibit large variations in film thickness. The rough surface morphology in this region is likely due to the local potential falling below the oxidation threshold.

In the region where the local potential is presumed to be below the threshold, the polymer film is speckled with aggregates that range in size from a few hundred nanometres to a few microns. These aggregates can be seen in Figure 4.3b-d and Figure 4.10 where they are indicated by white arrows.

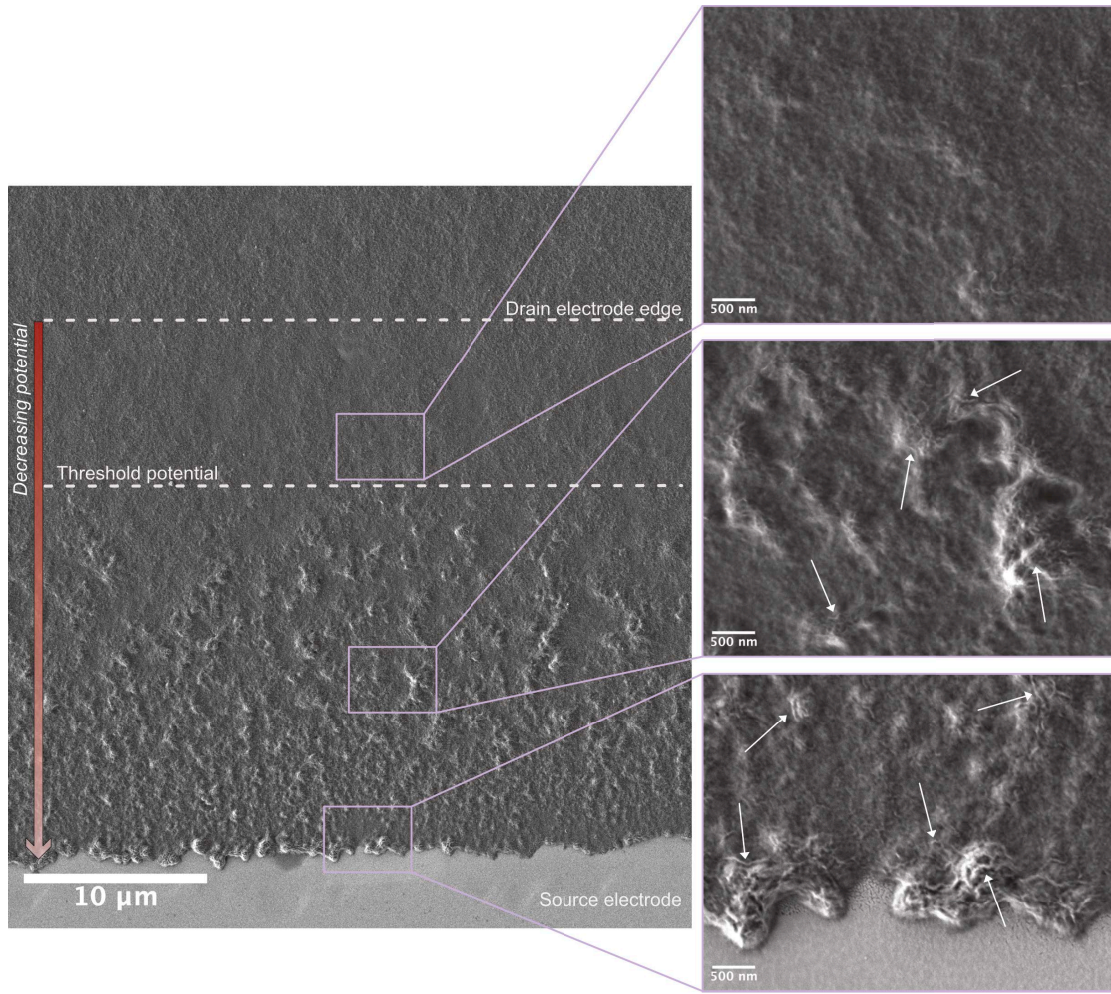


Figure 4.10: Surface morphology in different parts of the PETE-S channel. SEM images at 1kV of the PETE-S channel grown between source and drain electrodes for 30 s. The inset images to the right show different regions of the polymer film at a higher magnification. Dashed lines mark the position of the drain edge and the approximate distance from the drain electrode where the film morphology starts to change. White arrows point to fibrous structures within the clusters of material in the film.

4.1.3 A Layered Structure of the Polymer Film

After 2 s of growth, two types of film structures can be discerned in the PETE-S film in the region between the electrodes. First, a smooth film growing in direct contact with the substrate, as can be seen near the leading edge of the polymer film in Figure 4.11 (white arrow). Secondly, a more coarse film (marked by the

red arrow) growing on top of the smooth film. AFM measurements showed that the thickness of the first, smooth film is approximately 25-35 nm with an RMS roughness of about 3 nm. The total film thickness in the course region (red arrow) is roughly 35-45 nm, with an RMS roughness of about 10 nm, similarly to the film on top of the drain electrode after 2 s.

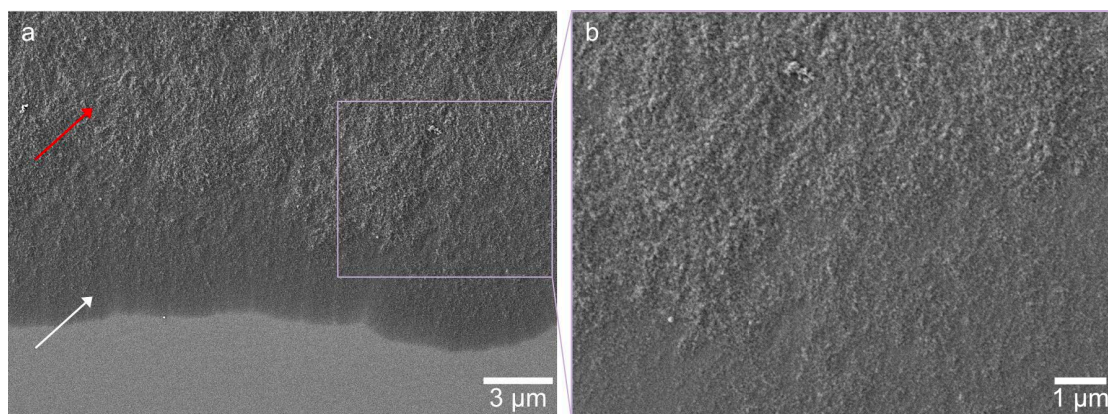


Figure 4.11: Higher magnification images of the PETE-S film after 2 s of polymerising bias. SEM images recorded at 1 kV of the leading edge of the polymer film. The polymer film consists of two parts: a smooth film growing in direct contact with the substrate (white arrow) and a more course film on top (red arrow). b) shows a higher magnification image of the course film in the dashed region in Figure a).

The observations from the 2 s film, which only partially covers the channel, combined with observations from the films grown for longer durations, suggest that a smooth film initially forms during the nucleation and early growth stages on the biased drain electrode and modified SiO_2 substrate. This is followed by film growth that leads to a more rough surface morphology. Both the smooth and rough films are clearly visible in the 2 s film in Figure 4.11. As growth time increases, the surface roughness becomes more pronounced, particularly in areas where the local potential is expected to be low and aggregates of fibrous structures are present.

4.1.4 Origin of the Aggregates in the Rough Surface Morphology of the Film

The micrometer-sized aggregates that were found in the rough parts of the films can be observed in detail in the insets of Figure 4.10. The aggregates are made up

of elongated features roughly 20 nm in thickness and a few hundred nanometres in length.

We hypothesise that these aggregates are formed in the electrolyte solution surrounding the polymer film before or during polymerisation. The solution acts as the reservoir for the ETE-S monomers that partake in the formation of the polymer film. Previous studies using molecular dynamics simulations have shown that ETE monomers in aqueous solutions are not always fully dispersed but may aggregate into clusters. [16] The morphology of such clusters, however, is not well known. Therefore, a dedicated study was performed to determine the aggregation characteristics of ETE monomers. The results of the study are presented in the following section.

4.2 Monomer Aggregation in Solution

In this thesis, ETE monomer solutions have been analysed using LPTEM and SEM to characterise the aggregation behaviour of pure ETE-S, pure ETE-PC and a mixture of equal parts ETE-S and ETE-PC (ETE-S:PC 50:50) in aqueous NaCl solutions. LPTEM imaging of the monomer solutions (Figure 4.12a-c) and complementary SEM imaging of dried solutions (Figure 4.12d-f and Figure 4.13) show the presence of aggregated monomers distributed in the solutions. The results are published in Paper II.

4.2.1 Morphology of ETE Monomer Clusters

The morphology of the ETE-S clusters can be described as thin platelets. These platelets are 15-30 nm in thickness and 50-300 nm in diameter. The platelets which are oriented edge-on with respect to the substrate (red arrows in Figure 4.12a and 4.12d) are more easily distinguished in the LPTEM images because there is more material in the beam path scattering the electrons compared to the platelets lying down (blue arrows). The ETE-PC 100% monomer solution contains both round clusters with average diameters of 30-70 nm and elongated fiber-like clusters with widths of 15-30 nm and lengths of 50-150 nm. On closer inspection, these fiber-like clusters resemble a line of round clusters, like pearls on a string. The ETE-S:PC 50:50 solution contains a mixture of round clusters, 30-50 nm in diameter, and elongated structures, 15-30 nm in width and 50-150 nm in length which are similar to the fiber-like clusters in the ETE-PC 100% solution. SEM images of the clusters in ETE-S:PC 50:50 show that they are more similar in size and shape to the clusters in ETE-PC 100% than ETE-S 100%. The observed cluster sizes for all three monomer solutions fall in the permeable range of the

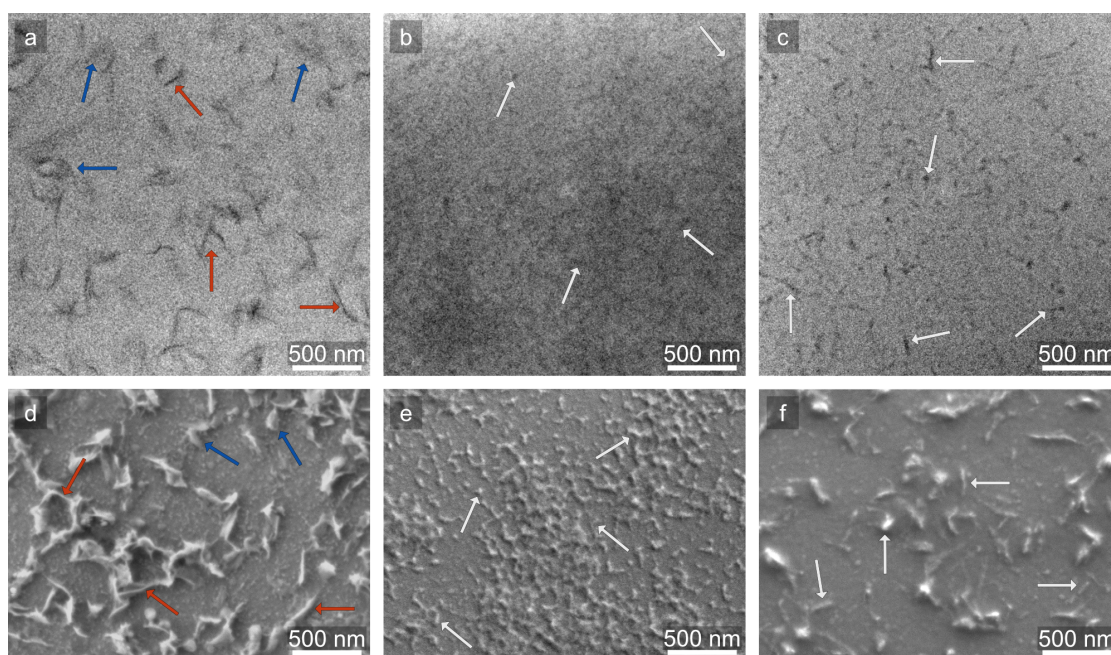


Figure 4.12: Morphology of ETE monomer clusters. Top row: Bright field LPTEM images recorded at 300 kV. Bottom row: SEM secondary electron (SE) images recorded at 1 kV of the same solutions after drying. a) and d) 5 mM ETE-S 100%, b) and e) 5 mM ETE-S:PC 50:50 and c) and f) 5 mM ETE-PC 100% in DI water with 10 mM NaCl. The dark features in the LPTEM images and bright features in the SEM images correspond to monomers aggregated into clusters (arrowed), which are present in all three solutions. Red arrows in figure a) and d) mark ETE-S platelet clusters which are seen edge-on. Blue arrows mark platelet clusters that are more parallel to the substrate.

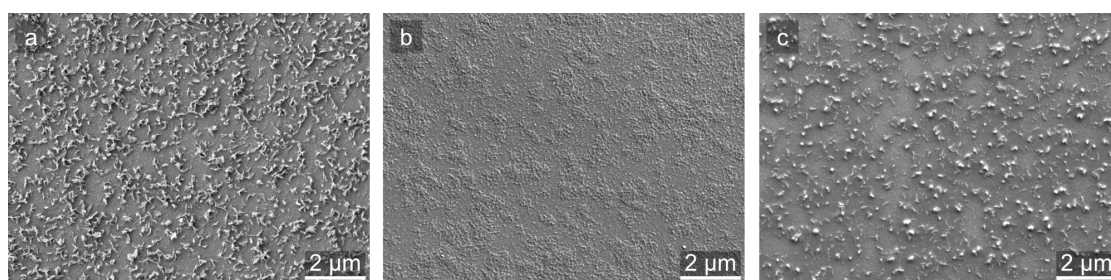


Figure 4.13: Overview of cluster distributions. SEM SE images recorded at 1 kV taken at a low magnification of dried solutions of DI water with 0.01 M NaCl and 5mM a) ETE-S 100%, b) ETE-S:PC 50:50 mix and c) ETE-PC 100%.

BBB, with the exception of the largest ETE-S clusters. This suggests that despite the aggregation tendencies, the material in all three monomer solutions still shows promise for use in *in vivo* device fabrication in the brain.

Moreover, the SEM images of ETE-S:PC 50:50 indicate that there is a cluster density variation within the solution (see Figures 4.12e and 4.13b). The regions with higher cluster density are about 0.5-3 μm in size. The ETE-S 100% and ETE-PC 100% show more homogeneous distributions of clusters in their respective solutions. The morphology of the monomer aggregates and their distribution may undergo slight changes during the drying process. Nonetheless, the morphologies observed in the LPTEM and SEM images for each sample are similar.

4.2.2 Polymerisation Properties and Aggregation Behaviour

CV measurements were carried out on the monomer solutions to ensure the samples were still pristine and had not undergone oxidation or degradation prior to imaging with LPTEM. The cyclic voltammograms shown in Figure 4.14 all reveal the presence of a distinct oxidation peak that can be expected in an intact ETE monomer solution sample. Moreover, it can be seen that the oxidation peak is shifted to higher potentials for ETE-PC compared to pure ETE-S, which has previously been reported and is due to the difference in charge density given by the side chains. [14] Of note is that the oxidation peak of the ETE-S:PC 50:50 solution is positioned between the peaks of the pure solutions. Moreover, two separate peaks can be distinguished in the mixed ETE-S:PC 50:50 solution rather than a smooth transition. This indicates a phase separation between the ETE-S and ETE-PC monomers in the clusters. Homogeneous aggregates consisting of molecules with only one of the side chains (i.e. either only ETE-S or only ETE-PC) exist along with uniformly distributed ETE-S and ETE-PC within individual clusters.

In Paper II it was again reported that π - π stacking is more prominent in ETE-S, producing linear aggregates, whereas ETE-PC develops more amorphous aggregates. The presence of ETE-PC in a solution of both monomer types repeatedly disrupts the structure of ETE-S aggregates. This explains why the morphology of the clusters found in the ETE-S:PC 50:50 solution in Figure 4.12b and 4.12e do not seem to be a direct mix of the morphologies found in the ETE-S 100% and ETE-PC 100% solutions, since no large clusters resembling those in Figure 4.12a and 4.12d of ETE-S could be found. This important finding strengthens the theory that when the two types of monomer are mixed, they do not maintain their individual properties such as monomer cluster morphology or oxidation potential. Instead, these properties take on a value corresponding more closely to the

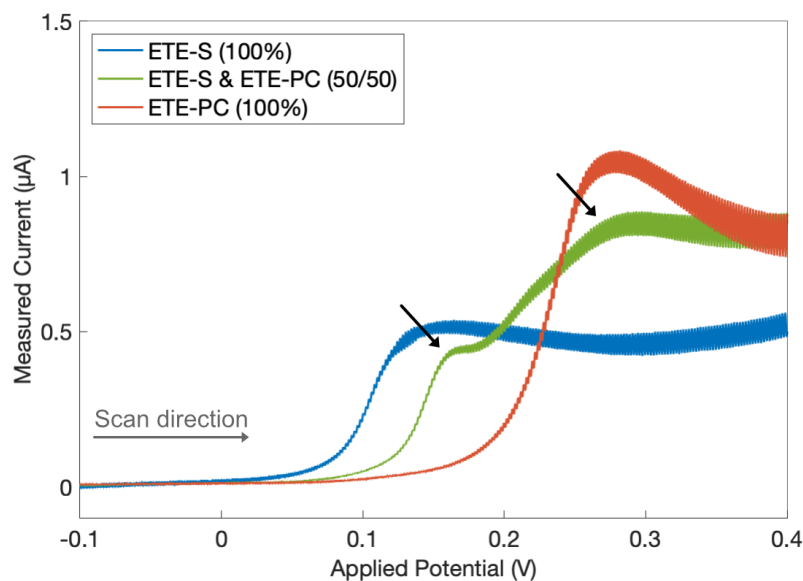


Figure 4.14: Cyclic voltammograms showing the oxidation peak in the first part of the anodic trace in the first scan cycle for the three monomer solutions. The position and shape of the oxidation peak is different for all three samples. The ETE-S:PC 50:50 sample shows evidence of two separate oxidation peaks (black arrows). Scan rate: 0.1 V s^{-1} . The working electrode, counter electrode and reference electrode are all Pt.

weighted average of the two components. This can be used to tune the intrinsic doping level, polymer film growth and properties of OECT channels as discussed in Paper II. Adding ETE-PC monomers to the ETE-S electrolyte solution used for electropolymerisation of transistor channels in OECTs could also help mitigate the incorporation of aggregates in the polymer film.

4.2.3 Monomer Aggregates in Solution and in OECT Films

The size and morphology of the elongated features inside the aggregates in the OECT films (see e.g. Figure 4.10) are in accordance with the structure of the ETE-S aggregates found in the aqueous NaCl solution in Figure 4.12. Aggregated monomers are therefore believed to be the origin of the clusters observed in the OECT channels.

4.2.4 Comparison Between Electron Microscopy Characterisation and Alternative Techniques

Dynamic light scattering (DLS) is another technique that has been used in attempts to determine the size distribution of individual monomers or monomer aggregates in solution. [16] While analysis of DLS data can give a qualitative estimation of particle sizes, it is not suitable for quantitative descriptions of the aggregation behaviour. Multiple scattering events, orientation effects and the choice of detector angle are all factors that make DLS measurements difficult to set up and interpret. Furthermore, the size of a scattering particle calculated from DLS measurements will be the hydrodynamic radius of a sphere moving in the same way as the scatterer. Assuming that the particle size given by DLS measurements is the actual size of the particle can therefore be misleading, especially for non-spherical objects. The results in Figure 4.12 and Figure 4.13 clearly show the anisotropic geometry of the monomer clusters, motivating the importance of treating them as non-spherical objects. In Paper II the cluster sizes determined from electron microscopy imaging are compared to average particle size distributions from DLS. Evaluation of the DLS measurements revealed a bimodal distribution of particles with the hydrodynamic radius of one population in the range of 3-4 nm and the other population in the range of 190-225 nm. Similar distributions were found for all three monomer solutions at two different concentrations (1 mM and 5 mM). Interestingly, no population of particles was found in the size range from 10-100 nm for any of the monomers, which is where many of the clusters are found in the LPTEM and SEM images. The explanation for this is that the DLS sizes do not correspond to the dimensions of the individual monomers or clusters but rather their rotational and translational diffusion constants. Thus, reliable quantitative information about the size and shape of the aggregates is here recommended to be obtained from structural characterisation techniques such as TEM rather than DLS.

4.3 Correlation Between the Structure of OECT Polymer Films and Their Electronic Properties

The drain current is limited by the weakest link in the polymer channel between the electrodes. Key factors influencing the conduction include the contact area between the polymer film and the electrodes on both sides, as well as the smallest cross-sectional area of the polymer film within the channel. While the lateral spreading of the film increases its total area, it did not enlarge the contact area with the biased drain electrode. Additionally, lateral spreading did not increase

the contact area with the source electrode, as the film extended only about 300 nm past the edge of the source electrode, even after 120 s of film growth. The increase in drain current over time is instead a result of an increase in cross-sectional area of the polymer film in the gap between the electrodes as more material is added to the film.

The aggregates found in the polymer channel can also impact the conductivity of the device. If these aggregates contain unpolymerised monomers, they may act as defects, disrupting the formation of continuous conductive pathways across the channel and thereby reducing the conductivity.

4.4 Structure of Conducting Hydrogels

This thesis work also explores the complex architecture of electroactive HA-BCN/PEG hydrogel scaffolds with incorporated PETE-S. The surface microstructure of HA-BCN/PEG hydrogels functionalised with 0, 5, 10, and 20 mg mL⁻¹ PETE-S has been investigated using SEM. The results are published in Paper III. SEM imaging of the pure, non-conductive HA-BCN/PEG hydrogel shown in Figure 4.15 reveals a porous film. Hereafter the abbreviation Gel refers to the pure HA-BCN/PEG hydrogel and e.g. 5 mg/ml PETE-S Gel refers to a HA-BCN/PEG hydrogel functionalised by *in situ* enzymatic polymerisation in a solution of 5 mg mL⁻¹ ETE-S.

4.4.1 Structure of Hydrogel Surfaces - Description and Origin of Porous Morphologies

The structure of the investigated hydrogels in Figure 4.15 can be described as pores separated by fibrous walls. The porosity of these hydrogels is dependent on the ratio between the cross-linking agent PEG-Az4 and BCN since the level of cross-linking affects the initial porous structures formed in the hydrogel. The porosity seen in the SEM images of the freeze-dried hydrogels is likely also affected by freeze drying process. Hydrogels typically have a very high water content in their native state, reaching values above 90%, and tend to shrink when dried. This suggests that the drying process can have a significant impact on the structure of the hydrogel network. Freeze drying, however, has been shown to induce less shrinkage than other drying methods [87] and the porous structures shown in Figure 4.15 can still be indicative of differences in material properties.

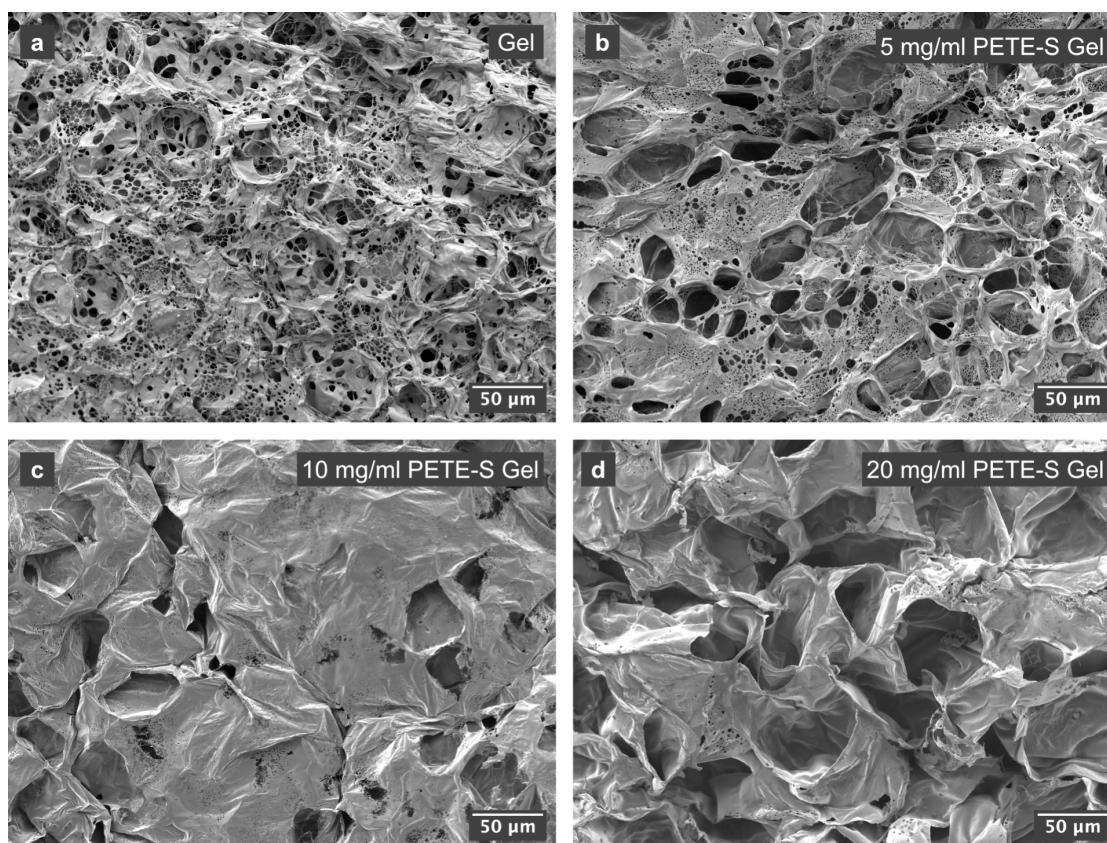


Figure 4.15: Surface morphology of freeze-dried hydrogels. SEM SE images at 1 kV of hydrogel samples showing the morphology of a) Gel sample, b) 5 mg/ml PETE-S Gel sample, c) 10 mg/ml PETE-S Gel sample, and d) 20 mg/ml PETE-S Gel sample. The structure consists of pores separated by walls. The walls become more continuous as the PETE-S concentration increases.

The pore sizes range from 1-50 μm in the pure Gel without polymer. There is a trend of increasing pore size from 1-50 μm in the Gel sample up to 20-100 μm in the 20 mg/ml PETE-S Gel, suggesting that the pore sizes become better optimised for large neural cells and tissue at higher polymer concentrations. Previous studies on similar HA hydrogel systems have shown that pores in the 50 - 100 μm size range are well suited to facilitate cell migration, contact between cells, as well as diffusion of oxygen and nutrients which are critical for cell survival and proliferation if the pores are interconnected. [15] The SEM images of the surface structures show that the pore walls in the hydrogels with incorporated PETE-S polymer are more continuous with less fibrillar structures than the pure Gel sample. As the polymer concentration increases from 5 mg/ml PETE-S to 20 mg/ml PETE-S (Figure 4.15b-d) the fibrillar structure transforms into a more and more continuous

morphology. However, as can be seen in Figure 4.15d, the 20 mg/ml PETE-S Gel still has small holes that are 0.5-5 μm in size in the pore walls. The amount of small holes decreases with increasing concentration of PETE-S in the 5-20 mg/ml range, suggesting that the interconnectivity and mass transport between pores also decreases. This could limit the ability of cells to grow, move and connect to form tissue.

SEM imaging of the hydrogel surfaces at higher magnifications reveals more information about the morphology. In the 10 mg/ml PETE-S Gel, there are still regions where the tendency of the hydrogel to form long filaments in web-like structures acting as scaffolding for the PETE-S film can be seen (Figure 4.16a). The presence of a rough surface morphology can also be seen in both Figure 4.16a and 4.16b, although there is no evidence of large monomer aggregates in the material, which could be seen for the electropolymerised OECT samples. These results suggests that this method of enzymatic polymerisation is effective at completely polymerising the potentially aggregated ETE-S monomer solutions.

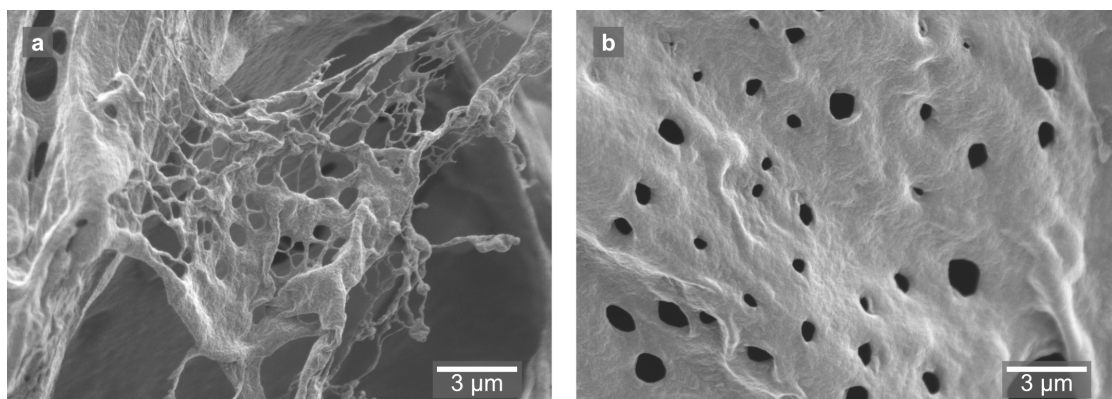


Figure 4.16: Higher magnification images of surface structures in freeze-dried hydrogels. SEM SE images at 1 kV of hydrogel samples showing a) the web-like network of the HA-BCN/PEG hydrogel acting as scaffolding for the 10 mg/ml PETE-S polymer and b) the rough surface texture of a 20 mg/ml PETE-S Gel sample.

4.4.2 Internal Structure of the Hydrogels

The analysis of surface structures was complemented by an analysis of bulk structures in the hydrogels. The internal microstructures were revealed by milling away material to create cross-sections in the hydrogel samples with a focused ion beam, as shown in Figure 4.17.

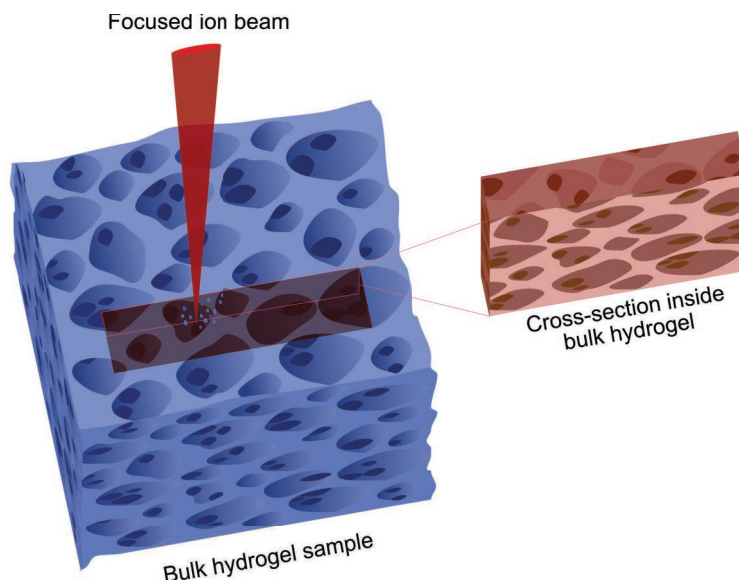


Figure 4.17: Illustration of how the internal structure of a hydrogel sample is revealed. A focused ion beam is used to mill away material from the bulk hydrogel sample which exposes a cross-section inside the hydrogel.

SEM imaging of the prepared cross-sections shows that the network of pores extends into the bulk structure (Figure 4.18). The pore wall thickness increases with increasing concentration of PETE-S incorporated in the hydrogels. The pore wall thicknesses were 0.5-1.5 μm , 0.5-2.0 μm , 0.7-3.0 μm , and 1.0-10 μm for the 0, 5, 10, and 20 mg/ml PETE-S Gels respectively.

The microstructure inside the hydrogel also changes with distance from the surface. The hydrogel material is more compact at increasing distance from the top surface. The wall thickness increases and the walls are more continuous, as can be seen in Figure 4.18. The increasingly compact walls with decreasing number of holes connecting the pores and creating pathways from the surface of the hydrogel can pose a challenge for oxygen and nutrient transport to deeper compartments of the hydrogel. In turn, this puts a limit on the maximal useful thickness of the hydrogel if cells cannot survive in the deeper sections of the structure. These

findings highlights the importance of also assessing the microstructure inside the bulk of a material since this may differ from the structures close to the surface.

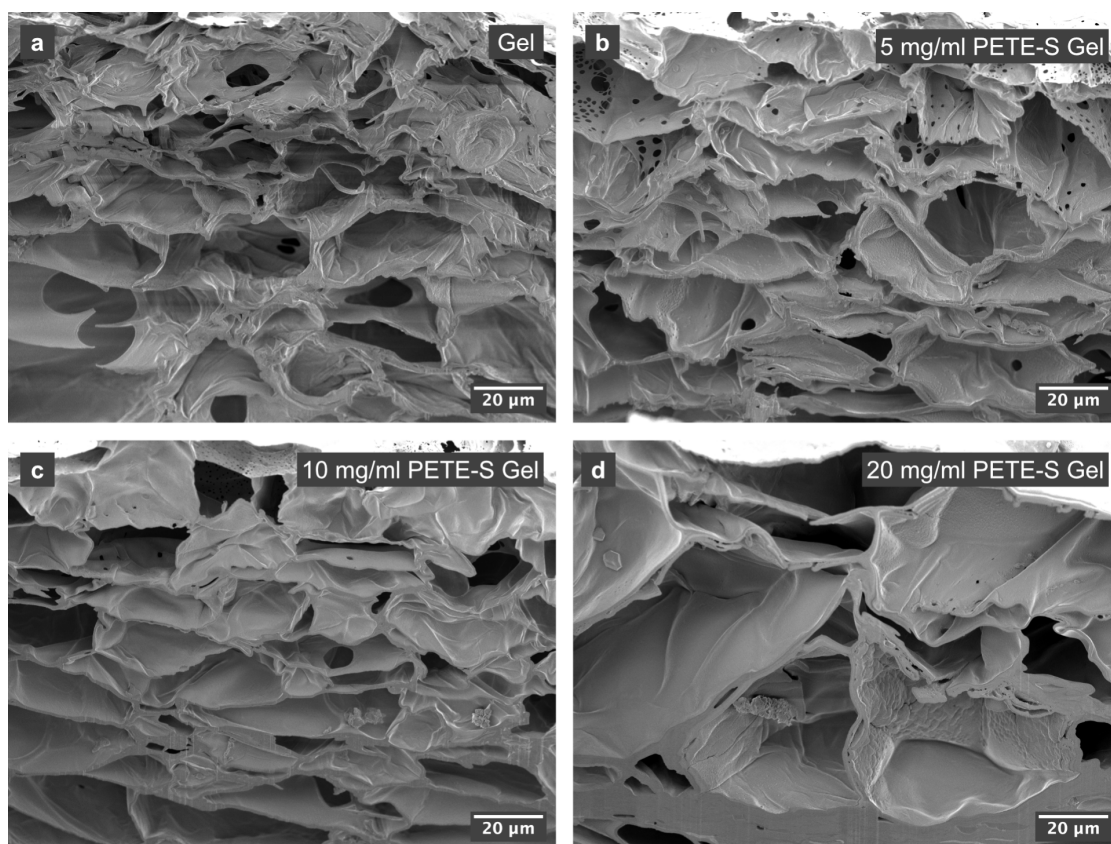


Figure 4.18: Internal structure of freeze-dried hydrogels. SEM SE images at 1 kV of cross-sectioned freeze-dried hydrogel samples showing the internal microstructure of a) Gel sample, b) 5 mg/ml PETE-S Gel sample, c) 10 mg/ml PETE-S Gel sample, and d) 20 mg/ml PETE-S Gel sample. The images show the pore structure within the bulk materials. The wall thickness of the pores increases as the amount of PETE-S increases. The walls become more continuous with increasing distance from the sample surface (top part of the images) when PETE-S is incorporated in the hydrogel.

It should be pointed out that the cross-sections in Figure 4.18 show two-dimensional slices of three-dimensional structures inside the bulk material. It is assumed that the slicing direction relative to the orientation of the pores is such that the pore walls are sliced orthogonally. Non-orthogonal slicing of the walls would result in a larger apparent wall thickness in the cross-sections. The two-dimensional imaging provides a qualitative measurement of the difference in wall thickness between

samples with different polymer concentrations. A quantitative evaluation of the thickness of the pore walls requires three-dimensional imaging that can be achieved by different tomography and reconstruction techniques. This would also reveal further information about the interconnectivity of the pores throughout hydrogel network, as has previously been described for similar materials. [138,143,144]

4.4.3 The Influence of the Material Structures on the Mechanical and Electrical Properties of the Hydrogels and Their Biocompatibility

The rheological properties of hydrogels are often evaluated in terms of their dynamic complex modulus. This modulus is divided into the storage modulus, G' , which describes the ability of the material to store energy under elastic stress when an oscillating force is applied, and the loss modulus, G'' , which describes the ability to dissipate stress through heat. The storage modulus is often equated to the Young's modulus as a measure of stiffness, although the two are not exactly the same. A higher storage modulus typically means that the material cannot undergo swelling or contraction as easily as a material with lower storage modulus. This is often influenced by the degree of cross-linking in the material since this will restrict swelling or compression. [145] The storage modulus of neural tissue is $G' \approx 100 - 1000$ Pa. [146,147] Rheological assessment of HA-BCN/PEG hydrogels with 0, 5, 10, and 20 mg mL⁻¹ PETE-S showed that the storage modulus for all four polymer concentrations were in the range of 500 to 1000 Pa, which is similar to that of neural tissue with minimal variation between the samples. This indicates that the amount of polymer in the material and the size or interconnectivity of pores in the hydrogel matrix do not have a considerable impact on the storage modulus. Alternatively, the contributions from the pore size and wall morphology cancel out each other. Only when the amount of PETE-S in the hydrogel reached 40 mg mL⁻¹ did the storage modulus increase significantly to $G' \approx 1500 - 1800$ Pa, implying a drastic increase in stiffness. Structural characterisation with SEM has not been carried out for this polymer concentration, but it is expected that the structure evolution follows the same trend of increasingly compact structure with increasing concentration of PETE-S.

The electrical properties of the hydrogels were also investigated and shown to be affected by the amount of PETE-S in the hydrogel. Both the conductivity and capacitance increased with the PETE-S content up to 20 mg mL⁻¹. This can be linked to the higher content of electrically conducting material in the hydrogel as well as longer continuous conductive pathways throughout the network with less holes. Moreover, the cytocompatibility of the hydrogels was assessed by adding

PC12 cells in the HA-BCN solution during cross-linking and polymerization of ETE-S monomers. The relative cell proliferation of the embedded cells was found to have improved for 1, 5 and 10 mg/ml PETE-S Gels compared to pure Gels after seven days. Higher PETE-S concentrations were less favourable, which can be explained by the increasingly compact structure of the hydrogels as the polymer concentration increases. This compact structure may hinder nutrients from reaching the cells inside the hydrogel matrix making it difficult for the cells to grow or even survive.

5 Conclusions and Outlook

In this thesis work, electron microscopy was used to study the micro- and nanostructure of polymeric systems for electronic neuro-pharmaceuticals. The material systems in this thesis are developed as model systems for pharmaceuticals intended to target neurodegenerative diseases, as devices to study signalling in cells, or as scaffolding in three-dimensional cell cultures. The material systems are all based on different varieties of the ETE monomer functionalised with two different side chains to form conducting conjugated polymers.

This work sheds light on the structure evolution of transistor channels in OEECTs formed by electropolymerisation of ETE-S monomers. It was discovered that a smooth polymer film forms during the initial stages of film growth on an APTES treated SiO_2 substrate and drain electrode kept at a polymerising potential. Subsequent polymer film formation on top of the first polymer film leads to an increasingly rough surface morphology. The time evolution of the surface morphology is thus important to consider when choosing a film growth time during fabrication of OEECT devices. The influence of the local electric potential on the formation and structure of the polymer channel in OEECTs is also discussed in this work. Micrometer sized aggregates with nanometer sized features were observed in parts of the polymer film where the local potential is expected to be below the threshold value for polymerisation, something that has not been reported before. LPTEM imaging of electrolyte solutions containing ETE-S monomers showed that the monomers in solution are not always fully dispersed but tend to form aggregates. The size and morphology of the aggregates observed in solution are in accordance with the size of the aggregates observed in the OEECT polymer films. Monomer aggregation in solution is therefore believed to be responsible for the aggregates observed in the electropolymerised films.

The aggregation characteristics depend on the type of monomer. Therefore, the aggregation behaviour of ETE-S is compared to that of ETE-PC monomers. LPTEM imaging of ETE-S and ETE-PC monomer solutions in their native liquid state combined with SEM imaging of dried monomer solutions showed that the typical sizes of ETE monomer clusters are in the range from approximately 15 nm to 300 nm. It was discovered that ETE-S forms larger clusters than ETE-PC. In solutions where both monomer species are present, ETE-PC continuously breaks

up the cluster structure of ETE-S so that mainly smaller clusters form. This is an indication that mixing in small amounts of ETE-PC in ETE-S solutions prior to electropolymerisation could mitigate the formation of large cluster defects in OEECT transistor channels. The presence of unpolymerised material in the film is expected to reduce the electrical performance of the device, limiting its usefulness in bioelectronics applications. In addition to influencing the morphology of the monomer clusters, the ratio between the different monomer species in monomer blend solutions was also found to affect the onset potential for electropolymerisation. Monomer blends thus opens up new ways of tuning the device properties of electropolymerised films, for example in OEECTs.

There is still no complete picture of what happens to the monomer clusters during polymerisation and why the clusters sometimes occur in the final polymer film. LPTEM can provide important insights into the dynamic processes in liquid samples and the growth of organic nanostructures. As a continuation of this work, polymerisation reactions can be studied *in situ* in the LPTEM setup to follow the structure evolution of monomer aggregates in solution. This can be performed with the biasing capabilities of the DENSsolutions Liquid Stream holder.

Furthermore, more information about the effects of the electric potential on the morphology of the polymer film in OEECTs and the performance of the final device is needed for the ability to predict how a similar device would function *in vivo* in biological tissue. A detailed study including modelling of the electric field in OEECT devices during channel growth could help shed more light on how the shape of the electric field changes during the different stages of film growth. The influence of the monomer aggregates on the electrical conductivity of the polymer film should also be investigated. Such a study would benefit from combining the SEM, LPTEM and AFM methodology applied in this work with molecular dynamics simulations.

Finally, this thesis work also explores the complex architecture of electroactive HA-BCN/PEG hydrogel scaffolds with incorporated PETE-S. The surface and bulk microstructure of the conducting hydrogels, revealed by a combination of SEM imaging and FIB cross-sectioning, could be described as pores separated by walls. The amount of ETE-S monomers present during fabrication of the hydrogels was found to affect the porous structure. The pore size increased with higher concentrations of PETE-S while the interconnectivity of the pores decreased. At intermediate PETE-S concentrations of 10-20 mg mL⁻¹ pore sizes in the range of 20-100 µm were observed. These dimensions are suitable for three-dimensional cell cultures of neuronal cell lines. However, the increasingly compact pore walls at higher PETE-S concentrations are suggested to be detrimental to cell proliferation as they hamper the transport of nutrients through the polymer hydrogel network. Moreover, the compact structure also makes the hydrogel increasingly

rigid, thereby reducing its mechanical compatibility with neuronal tissue. Optimal mechanical and electrical properties were achieved when small amounts of PETE-S were added to the HA-BCN/PEG hydrogel mix.

Moreover, in contrast to the electropolymerised films in OECT devices, large clusters of monomers were not found in the enzymatically polymerised hydrogels. Consequently, the enzymatic polymerisation route may be favourable over electropolymerisation if it is less affected by monomer clustering. Enzymatic polymerisation is also deemed to be a more mild strategy as it is not dependent on electrochemistry or strong redox chemistry and can be modulated by endogenous metabolites. This holds great promise for *in vivo* fabrication of organic electronics in physiological environments.

Bibliography

- [1] K. J. Barnham, C. L. Masters, and A. I. Bush, “Neurodegenerative diseases and oxidative stress,” *Nature Reviews Drug Discovery*, vol. 3, no. 3, pp. 205–214, 2004.
- [2] M. Rasool, A. Malik, M. S. Qureshi, A. Manan, P. N. Pushparaj, M. Asif, M. H. Qazi, A. M. Qazi, M. A. Kamal, S. H. Gan, and I. A. Sheikh, “Recent updates in the treatment of neurodegenerative disorders using natural compounds,” *Evidence-based Complementary and Alternative Medicine*, vol. 2014, 2014.
- [3] J. K. Krauss, N. Lipsman, T. Aziz, A. Boutet, P. Brown, J. W. Chang, B. Davidson, W. M. Grill, M. I. Hariz, A. Horn, M. Schulder, A. Mammis, P. A. Tass, J. Volkmann, and A. M. Lozano, “Technology of deep brain stimulation: current status and future directions,” *Nature Reviews Neurology*, vol. 17, no. 2, pp. 75–87, 2021.
- [4] A. M. Lozano, N. Lipsman, H. Bergman, P. Brown, S. Chabardes, J. W. Chang, K. Matthews, C. C. McIntyre, T. E. Schlaepfer, M. Schulder, Y. Temel, J. Volkmann, and J. K. Krauss, “Deep brain stimulation: current challenges and future directions,” *Nature Reviews Neurology*, vol. 15, no. 3, pp. 148–160, 2019.
- [5] D. T. Simon, E. O. Gabrielsson, K. Tybrandt, and M. Berggren, “Organic Bioelectronics: Bridging the Signaling Gap between Biology and Technology,” *Chemical Reviews*, vol. 116, no. 21, pp. 13009–13041, 2016.
- [6] S. M. Richardson-Burns, J. L. Hendricks, B. Foster, L. K. Povlich, D. H. Kim, and D. C. Martin, “Polymerization of the conducting polymer poly(3,4-ethylenedioxythiophene) (PEDOT) around living neural cells,” *Biomaterials*, vol. 28, no. 8, pp. 1539–1552, 2007.
- [7] M. G. Urbanek, T. A. Kung, C. M. Frost, D. C. Martin, L. M. Larkin, A. Wollstein, and P. S. Cederna, “Development of a Regenerative Peripheral Nerve Interface for Control of a Neuroprosthetic Limb,” *BioMed Research International*, vol. 2016, 2016.

- [8] E. Stavrinidou, R. Gabrielsson, K. P. R. Nilsson, S. K. Singh, J. F. Franco-Gonzalez, A. V. Volkov, M. P. Jonsson, A. Grimoldi, M. Elgland, I. V. Zozoulenko, D. T. Simon, and M. Berggren, "In vivo polymerization and manufacturing of wires and supercapacitors in plants," *Proceedings of the National Academy of Sciences of the United States of America*, vol. 114, no. 11, pp. 2807–2812, 2017.
- [9] G. Tommasini, G. Dufil, F. Fardella, X. Strakosas, E. Fergola, T. Abrahamsson, D. Bliman, R. Olsson, M. Berggren, A. Tino, E. Stavrinidou, and C. Tortiglione, "Seamless integration of bioelectronic interface in an animal model via in vivo polymerization of conjugated oligomers," *Bioactive Materials*, vol. 10, no. August 2021, pp. 107–116, 2022.
- [10] X. Strakosas, H. Biesmans, T. Abrahamsson, K. Hellman, M. S. Ejneby, M. J. Donahue, P. Ekström, F. Ek, M. Savvakis, M. Hjort, D. Bliman, M. Linares, C. Lindholm, E. Stavrinidou, J. Y. Gerasimov, D. T. Simon, R. Olsson, and M. Berggren, "Metabolite-induced in vivo fabrication of substrate-free organic bioelectronics," *Science*, vol. 379, no. 6634, pp. 795–802, 2023.
- [11] M. Hjort, A. H. Mousa, D. Bliman, M. A. Shameem, K. Hellman, A. S. Yadav, P. Ekström, F. Ek, and R. Olsson, "In situ assembly of bioresorbable organic bioelectronics in the brain," *Nature Communications*, vol. 14, no. 1, 2023.
- [12] J. Y. Gerasimov, R. Gabrielsson, R. Forchheimer, E. Stavrinidou, D. T. Simon, M. Berggren, and S. Fabiano, "An Evolvable Organic Electrochemical Transistor for Neuromorphic Applications," *Advanced Science*, vol. 6, no. 7, pp. 1–8, 2019.
- [13] J. Y. Gerasimov, D. Zhao, A. Sultana, T. Abrahamsson, S. Han, D. Bliman, D. Tu, D. T. Simon, R. Olsson, X. Crispin, M. Berggren, and S. Fabiano, "A Biomimetic Evolvable Organic Electrochemical Transistor," *Advanced Electronic Materials*, vol. 2001126, 2021.
- [14] J. Y. Gerasimov, A. Halder, A. H. Mousa, S. Ghosh, P. C. Harikesh, T. Abrahamsson, D. Bliman, J. Strandberg, M. Massetti, I. Zozoulenko, D. T. Simon, M. Berggren, R. Olsson, and S. Fabiano, "Rational Materials Design for In Operando Electropolymerization of Evolvable Organic Electrochemical Transistors," *Advanced Functional Materials*, vol. 32, no. 32, 2022.
- [15] M. Jury, I. Matthiesen, F. Rasti Boroojeni, S. L. Ludwig, L. Civitelli, T. E. Winkler, R. Selegård, A. Herland, and D. Aili, "Bioorthogonally Cross-

- Linked Hyaluronan–Laminin Hydrogels for 3D Neuronal Cell Culture and Biofabrication,” *Advanced Healthcare Materials*, vol. 11, no. 11, 2022.
- [16] I. Sahalianov, T. Abrahamsson, D. Priyadarshini, A. H. Mousa, K. Arja, J. Y. Gerasimov, M. Linares, D. T. Simon, R. Olsson, G. Baryshnikov, M. Berggren, and C. Musumeci, “Tuning the Emission of Bis-ethylenedioxythiophene-thiophenes upon Aggregation,” *Journal of Physical Chemistry B*, vol. 128, no. 27, pp. 6581–6588, 2024.
- [17] J. Cowie and V. Arrighi, *Polymers: Chemistry and Physics of Modern Materials*. CRC Press, 3rd ed., 2007.
- [18] K. Namsheer and C. S. Rout, “Conducting polymers: a comprehensive review on recent advances in synthesis, properties and applications,” *RSC Advances*, vol. 11, no. 10, pp. 5659–5697, 2021.
- [19] M. Berggren, X. Crispin, S. Fabiano, M. P. Jonsson, D. T. Simon, E. Stavrinidou, K. Tybrandt, and I. Zozoulenko, “Ion Electron–Coupled Functionality in Materials and Devices Based on Conjugated Polymers,” *Advanced Materials*, vol. 31, no. 22, pp. 1–15, 2019.
- [20] T. Nezakati, A. Seifalian, A. Tan, and A. M. Seifalian, “Conductive Polymers: Opportunities and Challenges in Biomedical Applications,” *Chemical Reviews*, vol. 118, no. 14, pp. 6766–6843, 2018.
- [21] J. L. Bredas and G. B. Street, “Polarons, bipolarons, and solitons in conducting polymers,” *Accounts of Chemical Research*, vol. 18, pp. 309–315, oct 1985.
- [22] V. Coropceanu, J. Cornil, D. A. da Silva Filho, Y. Olivier, R. Silbey, and J.-L. Brédas, “Charge Transport in Organic Semiconductors,” *Chemical Reviews*, vol. 107, pp. 926–952, apr 2007.
- [23] M. Koopmans, M. A. Leiviskä, J. Liu, J. Dong, L. Qiu, J. C. Hummelen, G. Portale, M. C. Heiber, and L. J. A. Koster, “Electrical Conductivity of Doped Organic Semiconductors Limited by Carrier-Carrier Interactions,” *ACS Applied Materials and Interfaces*, vol. 12, no. 50, pp. 56222–56230, 2020.
- [24] A. O. Patil, Y. Ikenoue, N. Basescu, N. Colaneri, J. Chen, F. Wudl, and A. J. Heeger, “Self-doped conducting polymers,” *Synthetic Metals*, vol. 20, pp. 151–159, jun 1987.
- [25] T. H. Le, Y. Kim, and H. Yoon, “Electrical and electrochemical properties of conducting polymers,” *Polymers*, vol. 9, no. 4, 2017.
- [26] R. Balint, N. J. Cassidy, and S. H. Cartmell, “Conductive polymers: Towards

- a smart biomaterial for tissue engineering,” *Acta Biomaterialia*, vol. 10, no. 6, pp. 2341–2353, 2014.
- [27] G. Kaur, R. Adhikari, P. Cass, M. Bown, and P. Gunatillake, “Electrically conductive polymers and composites for biomedical applications,” *RSC Advances*, vol. 5, no. 47, pp. 37553–37567, 2015.
- [28] S. D. Baranovskii, “Theoretical description of charge transport in disordered organic semiconductors,” *Physica Status Solidi (B) Basic Research*, vol. 251, no. 3, pp. 487–525, 2014.
- [29] Y. Yao, H. Dong, and W. Hu, “Ordering of conjugated polymer molecules: Recent advances and perspectives,” *Polymer Chemistry*, vol. 4, no. 20, pp. 5197–5205, 2013.
- [30] J. F. Franco-Gonzalez and I. V. Zozoulenko, “Molecular Dynamics Study of Morphology of Doped PEDOT: From Solution to Dry Phase,” *Journal of Physical Chemistry B*, vol. 121, no. 16, pp. 4299–4307, 2017.
- [31] M. Berggren and A. Richter-Dahlfors, “Organic bioelectronics,” *Advanced Materials*, vol. 19, no. 20, pp. 3201–3213, 2007.
- [32] J. Rivnay, R. M. Owens, and G. G. Malliaras, “The rise of organic bioelectronics,” *Chemistry of Materials*, vol. 26, no. 1, pp. 679–685, 2014.
- [33] H. P. Erickson, “Size and shape of protein molecules at the nanometer level determined by sedimentation, gel filtration, and electron microscopy,” *Biological Procedures Online*, vol. 11, no. 1, pp. 32–51, 2009.
- [34] J. Seiftner, A. Ratner, and D. Sloane, *Concepts in Medical Physiology*. Lippincott Williams & Wilkins, 2005.
- [35] A. Manuel Stephan, “Review on gel polymer electrolytes for lithium batteries,” *European Polymer Journal*, vol. 42, no. 1, pp. 21–42, 2006.
- [36] M. Hess, R. G. Jones, J. Kahovec, T. Kitayama, P. Kratochvíl, P. Kubisa, W. Mormann, R. F. T. Stepto, D. Tabak, J. Vohlídal, and E. S. Wilks, “Terminology of polymers containing ionizable or ionic groups and of polymers containing ions (iupac recommendations 2006),” *Pure and Applied Chemistry*, vol. 78, no. 11, pp. 2067–2074, 2006.
- [37] D. E. Discher, P. Janmey, and Y. L. Wang, “Tissue cells feel and respond to the stiffness of their substrate,” *Science*, vol. 310, no. 5751, pp. 1139–1143, 2005.
- [38] A. Buxboim, I. L. Ivanovska, and D. E. Discher, “Matrix elasticity, cytoskele-

- tal forces and physics of the nucleus: How deeply do cells 'feel' outside and in?," *Journal of Cell Science*, vol. 123, no. 3, pp. 297–308, 2010.
- [39] R. O. Hynes, "Integrins: A family of cell surface receptors," *Cell*, vol. 48, no. 4, pp. 549–554, 1987.
- [40] C. J. Wilson, R. E. Clegg, D. I. Leavesley, and M. J. Pearcy, "Mediation of biomaterial-cell interactions by adsorbed proteins: a review," *Tissue Engineering*, vol. 11, 2005.
- [41] C. Barberio, J. Saez, A. Withers, M. Nair, F. Tamagnini, and R. M. Owens, "Conducting Polymer-ECM Scaffolds for Human Neuronal Cell Differentiation," *Advanced Healthcare Materials*, vol. 11, no. 20, pp. 1–13, 2022.
- [42] S. Sze and K. K. Ng, *Physics of Semiconductor Devices*. John Wiley & Sons, Inc., oct 2006.
- [43] H. S. White, G. P. Kittlesen, and M. S. Wrighton, "Chemical Derivatization of an Array of Three Gold Microelectrodes with Polypyrrole: Fabrication of a Molecule-Based Transistor," *Journal of the American Chemical Society*, vol. 106, no. 18, pp. 5375–5377, 1984.
- [44] J. Rivnay, S. Inal, A. Salleo, R. M. Owens, M. Berggren, and G. G. Malliaras, "Organic electrochemical transistors," *Nature Reviews Materials*, vol. 3, 2018.
- [45] R. M. Owens and G. G. Malliaras, "Organic electronics at the interface with biology," *MRS Bulletin*, vol. 35, no. 6, pp. 449–456, 2010.
- [46] P. Lin and F. Yan, "Organic thin-film transistors for chemical and biological sensing," *Advanced Materials*, vol. 24, no. 1, pp. 34–51, 2012.
- [47] M. H. Bolin, K. Svennersten, D. Nilsson, A. Sawatdee, E. W. Jager, A. Richter-Dahlfors, and M. Berggren, "Active control of epithelial cell-density gradients grown along the channel of an organic electrochemical transistor," *Advanced Materials*, vol. 21, no. 43, pp. 4379–4382, 2009.
- [48] D. Khodagholy, J. Rivnay, M. Sessolo, M. Gurfinkel, P. Leleux, L. H. Jimison, E. Stavrinidou, T. Herve, S. Sanaur, R. M. Owens, and G. G. Malliaras, "High transconductance organic electrochemical transistors," *Nature Communications*, vol. 4, pp. 1–6, 2013.
- [49] A. Williamson, M. Ferro, P. Leleux, E. Ismailova, A. Kaszas, T. Doublet, P. Quilichini, J. Rivnay, B. Rózsa, G. Katona, C. Bernard, and G. G. Malliaras, "Localized Neuron Stimulation with Organic Electrochemical

- Transistors on Delaminating Depth Probes,” *Advanced Materials*, vol. 27, no. 30, pp. 4405–4410, 2015.
- [50] X. Ji, B. D. Paulsen, G. K. Chik, R. Wu, Y. Yin, P. K. Chan, and J. Rivnay, “Mimicking associative learning using an ion-trapping non-volatile synaptic organic electrochemical transistor,” *Nature Communications*, vol. 12, no. 1, pp. 1–12, 2021.
- [51] Y. Van De Burgt, E. Lubberman, E. J. Fuller, S. T. Keene, G. C. Faria, S. Agarwal, M. J. Marinella, A. Alec Talin, and A. Salleo, “A non-volatile organic electrochemical device as a low-voltage artificial synapse for neuro-morphic computing,” *Nature Materials*, vol. 16, no. 4, pp. 414–418, 2017.
- [52] D. A. Bernards and G. G. Malliaras, “Steady-state and transient behavior of organic electrochemical transistors,” *Advanced Functional Materials*, vol. 17, no. 17, pp. 3538–3544, 2007.
- [53] J. Rivnay, P. Leleux, M. Ferro, M. Sessolo, A. Williamson, D. A. Koutsouras, D. Khodagholy, M. Ramuz, X. Strakosas, R. M. Owens, C. Benar, J. M. Badier, C. Bernard, and G. G. Malliaras, “High-performance transistors for bioelectronics through tuning of channel thickness,” *Science Advances*, vol. 1, no. 4, pp. 1–5, 2015.
- [54] E. Stavrinidou, P. Leleux, H. Rajaona, D. Khodagholy, J. Rivnay, M. Lindau, S. Sanaur, and G. G. Malliaras, “Direct measurement of ion mobility in a conducting polymer,” *Advanced Materials*, vol. 25, no. 32, pp. 4488–4493, 2013.
- [55] R. Noriega, J. Rivnay, K. Vandewal, F. P. Koch, N. Stingelin, P. Smith, M. F. Toney, and A. Salleo, “A general relationship between disorder, aggregation and charge transport in conjugated polymers,” *Nature Materials*, vol. 12, no. 11, pp. 1038–1044, 2013.
- [56] D. Nilsson, T. Kugler, P. O. Svensson, and M. Berggren, “An all-organic sensor-transistor based on a novel electrochemical transducer concept printed electrochemical sensors on paper,” *Sensors and Actuators, B: Chemical*, vol. 86, no. 2-3, pp. 193–197, 2002.
- [57] Y. Wang, C. Zhu, R. Pfattner, H. Yan, L. Jin, S. Chen, F. Molina-Lopez, F. Lissel, J. Liu, N. I. Rabiah, Z. Chen, J. W. Chung, C. Linder, M. F. Toney, B. Murmann, and Z. Bao, “A highly stretchable, transparent, and conductive polymer,” *Science Advances*, vol. 3, no. 3, pp. 1–10, 2017.
- [58] H. F. d. P. Barbosa, A. Asyuda, M. Skowrons, A. Schander, and B. Lüssem,

- “Processing of organic electrochemical transistors,” *MRS Communications*, vol. 14, no. 2, pp. 132–148, 2024.
- [59] E. M. Ahmed, “Hydrogel: Preparation, characterization, and applications: A review,” *Journal of Advanced Research*, vol. 6, no. 2, pp. 105–121, 2015.
- [60] N. Annabi, J. W. Nichol, X. Zhong, C. Ji, S. Koshy, A. Khademhosseini, and F. Dehghani, “Controlling the porosity and microarchitecture of hydrogels for tissue engineering,” *Tissue Engineering - Part B: Reviews*, vol. 16, no. 4, pp. 371–383, 2010.
- [61] D. N. Heo, S. J. Lee, R. Timsina, X. Qiu, N. J. Castro, and L. G. Zhang, “Development of 3D printable conductive hydrogel with crystallized PEDOT:PSS for neural tissue engineering,” *Materials Science and Engineering C*, vol. 99, no. January, pp. 582–590, 2019.
- [62] P. Zhuang, A. X. Sun, J. An, C. K. Chua, and S. Y. Chew, “3D neural tissue models: From spheroids to bioprinting,” *Biomaterials*, vol. 154, pp. 113–133, 2018.
- [63] M. N. Collins and C. Birkinshaw, “Morphology of crosslinked hyaluronic acid porous hydrogels,” *Journal of Applied Polymer Science*, vol. 120, pp. 1040–1049, apr 2011.
- [64] I. Bružauskaitė, D. Bironaitė, E. Bagdonas, and E. Bernotienė, “Scaffolds and cells for tissue regeneration: different scaffold pore sizes—different cell effects,” *Cytotechnology*, vol. 68, no. 3, pp. 355–369, 2016.
- [65] R. A. Green, N. H. Lovell, G. G. Wallace, and L. A. Poole-Warren, “Conducting polymers for neural interfaces: Challenges in developing an effective long-term implant,” *Biomaterials*, vol. 29, no. 24-25, pp. 3393–3399, 2008.
- [66] R. A. Green, R. T. Hassarati, J. A. Goding, S. Baek, N. H. Lovell, P. J. Martens, and L. A. Poole-Warren, “Conductive Hydrogels: Mechanically Robust Hybrids for Use as Biomaterials,” *Macromolecular Bioscience*, vol. 12, no. 4, pp. 494–501, 2012.
- [67] B. Guo, L. Glavas, and A. C. Albertsson, “Biodegradable and electrically conducting polymers for biomedical applications,” *Progress in Polymer Science*, vol. 38, no. 9, pp. 1263–1286, 2013.
- [68] B. Lu, H. Yuk, S. Lin, N. Jian, K. Qu, J. Xu, and X. Zhao, “Pure PEDOT:PSS hydrogels,” *Nature Communications*, vol. 10, no. 1, 2019.
- [69] K. Kenry and B. Liu, “Recent Advances in Biodegradable Conducting Poly-

- mers and Their Biomedical Applications,” *Biomacromolecules*, vol. 19, no. 6, pp. 1783–1803, 2018.
- [70] K. I. Ritzau-Reid, C. D. Spicer, A. Gelmi, C. L. Grigsby, J. F. Ponder, V. Bemmer, A. Creamer, R. Vilar, A. Serio, and M. M. Stevens, “An Electroactive Oligo-EDOT Platform for Neural Tissue Engineering,” *Advanced Functional Materials*, vol. 30, no. 42, 2020.
- [71] M. ElMahmoudy, S. Inal, A. Charrier, I. Uguz, G. G. Malliaras, and S. Sanaur, “Tailoring the Electrochemical and Mechanical Properties of PEDOT:PSS Films for Bioelectronics,” *Macromolecular Materials and Engineering*, vol. 302, no. 5, pp. 1–8, 2017.
- [72] S. Budday, R. Nay, R. de Rooij, P. Steinmann, T. Wyrobek, T. C. Ovaert, and E. Kuhl, “Mechanical properties of gray and white matter brain tissue by indentation,” *Journal of the Mechanical Behavior of Biomedical Materials*, vol. 46, pp. 318–330, 2015.
- [73] D. Priyadarshini, C. Musumeci, D. Bliman, T. Abrahamsson, C. Lindholm, M. Vagin, X. Strakosas, R. Olsson, M. Berggren, J. Y. Gerasimov, and D. T. Simon, “Enzymatically Polymerized Organic Conductors on Model Lipid Membranes,” *Langmuir*, vol. 39, no. 23, pp. 8196–8204, 2023.
- [74] A. V. Volkov, S. K. Singh, E. Stavrinidou, R. Gabrielsson, J. F. Franco-Gonzalez, A. Cruce, W. M. Chen, D. T. Simon, M. Berggren, and I. V. Zozoulenko, “Spectroelectrochemistry and Nature of Charge Carriers in Self-Doped Conducting Polymer,” *Advanced Electronic Materials*, vol. 3, no. 8, pp. 1–8, 2017.
- [75] N. Elgrishi, K. J. Rountree, B. D. McCarthy, E. S. Rountree, T. T. Eisenhart, and J. L. Dempsey, “A Practical Beginner’s Guide to Cyclic Voltammetry,” *Journal of Chemical Education*, vol. 95, no. 2, pp. 197–206, 2018.
- [76] D. Mantione, E. Stavrinidou, E. Pavlopoulou, E. Istif, G. Dufil, L. Vallan, D. Parker, C. Brochon, E. Cloutet, G. Hadziioannou, and M. Berggren, “Thiophene-based trimers for in vivo electronic functionalization of tissues,” *ACS Applied Electronic Materials*, vol. 2, no. 12, pp. 4065–4071, 2020.
- [77] R. Daneman and A. Prat, “The Blood–Brain Barrier,” *Cold Spring Harbor Perspectives in Biology*, vol. 7, p. a020412, jan 2015.
- [78] G. Sonavane, K. Tomoda, and K. Makino, “Biodistribution of colloidal gold nanoparticles after intravenous administration: Effect of particle size,” *Colloids and Surfaces B: Biointerfaces*, vol. 66, no. 2, pp. 274–280, 2008.

-
- [79] S. A. Kulkarni and S. S. Feng, “Effects of particle size and surface modification on cellular uptake and biodistribution of polymeric nanoparticles for drug delivery,” *Pharmaceutical Research*, vol. 30, no. 10, pp. 2512–2522, 2013.
- [80] J. Y. Gerasimov, D. Tu, V. Hitaishi, P. C. Harikesh, C. Y. Yang, T. Abrahamsson, M. Rad, M. J. Donahue, M. S. Ejneby, M. Berggren, R. Forchheimer, and S. Fabiano, “A Biologically Interfaced Evolvable Organic Pattern Classifier,” *Advanced Science*, vol. 10, no. 14, pp. 1–9, 2023.
- [81] E. Stavrinidou, R. Gabrielsson, E. Gomez, X. Crispin, O. Nilsson, D. T. Simon, and M. Berggren, “Electronic plants,” *Science Advances*, vol. 1, no. 10, 2015.
- [82] J. R. Fraser, T. C. Laurent, and U. B. Laurent, “Hyaluronan: Its nature, distribution, functions and turnover,” *Journal of Internal Medicine*, vol. 242, no. 1, pp. 27–33, 1997.
- [83] T. A. Jennings, *Lyophilization*. Boca Raton: CRC Press, 1 ed., aug 1999.
- [84] S. Sornkamnerd, M. K. Okajima, and T. Kaneko, “Tough and Porous Hydrogels Prepared by Simple Lyophilization of LC Gels,” *ACS Omega*, vol. 2, no. 8, pp. 5304–5314, 2017.
- [85] J. Grenier, H. Duval, F. Barou, P. Lv, B. David, and D. Letourneur, “Mechanisms of pore formation in hydrogel scaffolds textured by freeze-drying,” *Acta Biomaterialia*, vol. 94, pp. 195–203, 2019.
- [86] T. Kopač, A. Ručigaj, and M. Krajnc, “The mutual effect of the crosslinker and biopolymer concentration on the desired hydrogel properties,” *International Journal of Biological Macromolecules*, vol. 159, pp. 557–569, 2020.
- [87] Y. Gombert, F. Roncoroni, A. Sánchez-Ferrer, and N. D. Spencer, “The hierarchical bulk molecular structure of poly(acrylamide) hydrogels: Beyond the fishing net,” *Soft Matter*, vol. 16, no. 42, pp. 9789–9798, 2020.
- [88] J. I. Goldstein, D. E. Newbury, J. R. Michael, N. W. Ritchie, J. H. J. Scott, and D. C. Joy, *Scanning Electron Microscopy and X-Ray Microanalysis*. New York, NY: Springer New York, 4 ed., 2018.
- [89] L. Reimer, *Scanning Electron Microscopy: Physics of Image Formation and Microanalysis*, vol. 45 of *Springer Series in Optical Sciences*. Berlin, Heidelberg: Springer Berlin Heidelberg, 2 ed., 1998.
- [90] D. C. Joy and J. B. Pawley, “High-resolution scanning electron microscopy,” *Ultramicroscopy*, vol. 47, pp. 80–100, nov 1992.

- [91] D. B. Williams and C. B. Carter, *Transmission Electron Microscopy*. New York, NY: Springer Science+Business Media, 1996.
- [92] C. Kisielowski, B. Freitag, M. Bischoff, H. Van Lin, S. Lazar, G. Knippels, P. Tiemeijer, M. Van Der Stam, S. Von Harrach, M. Stekelenburg, M. Haider, S. Uhlemann, H. Müller, P. Hartel, B. Kabius, D. Miller, I. Petrov, E. A. Olson, T. Donchev, E. A. Kenik, A. R. Lupini, J. Bentley, S. J. Pennycook, I. M. Anderson, A. M. Minor, A. K. Schmid, T. Duden, V. Radmilovic, Q. M. Ramasse, M. Watanabe, R. Erni, E. A. Stach, P. Denes, and U. Dahmen, “Detection of single atoms and buried defects in three dimensions by aberration-corrected electron microscope with 0.5-Å information limit,” *Microscopy and Microanalysis*, vol. 14, no. 5, pp. 469–477, 2008.
- [93] R. Egerton, *Electron Energy-Loss Spectroscopy in the Electron Microscope*. New York, NY: Springer Science+Business Media, 3 ed., 2011.
- [94] J. J. Hren, J. I. Goldstein, and D. C. Joy, *Introduction to Analytical Electron Microscopy*. New York, NY: Springer Science+Business Media, 1979.
- [95] R. F. Egerton, P. Li, and M. Malac, “Radiation damage in the TEM and SEM,” *Micron*, vol. 35, no. 6, pp. 399–409, 2004.
- [96] R. F. Egerton, “Radiation damage to organic and inorganic specimens in the TEM,” *Micron*, vol. 119, no. November 2018, pp. 72–87, 2019.
- [97] R. Henderson, “Image contrast in high-resolution electron microscopy of biological macromolecules: Tmv in ice,” *Ultramicroscopy*, vol. 46, no. 1, pp. 1–18, 1992.
- [98] Q. Chen, C. Dwyer, G. Sheng, C. Zhu, X. Li, C. Zheng, and Y. Zhu, “Imaging Beam-Sensitive Materials by Electron Microscopy,” *Advanced Materials*, vol. 32, p. 1907619, apr 2020.
- [99] R. F. Egerton, “Dose measurement in the TEM and STEM,” *Ultramicroscopy*, vol. 229, no. June, p. 113363, 2021.
- [100] B. Kuei and E. D. Gomez, “Pushing the limits of high-resolution polymer microscopy using antioxidants,” *Nature Communications*, vol. 12, no. 1, 2021.
- [101] F. M. Ross, *Liquid Cell Electron Microscopy*. Cambridge University Press, 2016.
- [102] Y. Liao, “Practical electron microscopy and database,” 2006. <https://www.globalsino.com/EM/> [Accessed: July 2024].
- [103] T. W. Hansen, J. B. Wagner, and R. E. Dunin-Borkowski, “Aberration cor-

- rected and monochromated environmental transmission electron microscopy: Challenges and prospects for materials science,” *Materials Science and Technology*, vol. 26, no. 11, pp. 1338–1344, 2010.
- [104] D. R. Lide, *CRC Handbook of Chemistry and Physics*. CRC Press, 85 ed., 2004.
- [105] S. Pu, C. Gong, and A. W. Robertson, “Liquid cell transmission electron microscopy and its applications,” *Royal Society Open Science*, vol. 7, no. 1, 2020.
- [106] M. J. Williamson, R. M. Tromp, P. M. Vereecken, R. Hull, and F. M. Ross, “Dynamic microscopy of nanoscale cluster growth at the solid-liquid interface,” *Nature Materials*, vol. 2, no. 8, pp. 532–536, 2003.
- [107] F. M. Ross, J. Tersoff, and M. C. Reuter, “Sawtooth faceting in silicon nanowires,” *Physical Review Letters*, vol. 95, no. 14, pp. 1–4, 2005.
- [108] J. E. Evans, K. L. Jungjohann, N. D. Browning, and I. Arslan, “Controlled growth of nanoparticles from solution with in situ liquid transmission electron microscopy,” *Nano Letters*, vol. 11, no. 7, pp. 2809–2813, 2011.
- [109] H. Zheng, R. K. Smith, Y. W. Jun, C. Kisielowski, U. Dahmen, and A. Paul Alivisatos, “Observation of single colloidal platinum nanocrystal growth trajectories,” *Science*, vol. 324, no. 5932, pp. 1309–1312, 2009.
- [110] S. W. Chee, S. H. Pratt, K. Hattar, D. Duquette, F. M. Ross, and R. Hull, “Studying localized corrosion using liquid cell transmission electron microscopy,” *Chemical Communications*, vol. 51, no. 1, pp. 168–171, 2015.
- [111] N. De Jonge, D. B. Peckys, G. J. Kremers, and D. W. Piston, “Electron microscopy of whole cells in liquid with nanometer resolution,” *Proceedings of the National Academy of Sciences of the United States of America*, vol. 106, no. 7, pp. 2159–2164, 2009.
- [112] N. Mohanty, M. Fahrenholtz, A. Nagaraja, D. Boyle, and V. Berry, “Impermeable graphenic encasement of bacteria,” *Nano Letters*, vol. 11, no. 3, pp. 1270–1275, 2011.
- [113] D. B. Peckys, P. Mazur, K. L. Gould, and N. De Jonge, “Fully hydrated yeast cells imaged with electron microscopy,” *Biophysical Journal*, vol. 100, no. 10, pp. 2522–2529, 2011.
- [114] D. B. Peckys and N. De Jonge, “Visualizing gold nanoparticle uptake in live cells with liquid scanning transmission electron microscopy,” *Nano Letters*, vol. 11, no. 4, pp. 1733–1738, 2011.

- [115] B. L. Mehdi, J. Qian, E. Nasybulin, C. Park, D. A. Welch, R. Faller, H. Mehta, W. A. Henderson, W. Xu, C. M. Wang, J. E. Evans, J. Liu, J. G. Zhang, K. T. Mueller, and N. D. Browning, "Observation and quantification of nanoscale processes in lithium batteries by operando electrochemical (S)TEM," *Nano Letters*, vol. 15, no. 3, pp. 2168–2173, 2015.
- [116] R. L. Sacci, N. J. Dudney, K. L. More, L. R. Parent, I. Arslan, N. D. Browning, and R. R. Unocic, "Direct visualization of initial SEI morphology and growth kinetics during lithium deposition by in situ electrochemical transmission electron microscopy," *Chemical Communications*, vol. 50, no. 17, pp. 2104–2107, 2014.
- [117] Z. Zeng, W. I. Liang, H. G. Liao, H. L. Xin, Y. H. Chu, and H. Zheng, "Visualization of electrode-electrolyte interfaces in LiPF₆/EC/DEC electrolyte for lithium ion batteries via in situ TEM," *Nano Letters*, vol. 14, no. 4, pp. 1745–1750, 2014.
- [118] J. Liu, B. Wei, J. D. Sloppy, L. Ouyang, C. Ni, and D. C. Martin, "Direct Imaging of the Electrochemical Deposition of Poly(3,4-ethylenedioxythiophene) by Transmission Electron Microscopy," *ACS Macro Letters*, vol. 4, no. 9, pp. 897–900, 2015.
- [119] M. A. Touve, C. A. Figg, D. B. Wright, C. Park, J. Cantlon, B. S. Sumerlin, and N. C. Gianneschi, "Polymerization-Induced Self-Assembly of Micelles Observed by Liquid Cell Transmission Electron Microscopy," *ACS Central Science*, vol. 4, no. 5, pp. 543–547, 2018.
- [120] C. Li, C. C. Tho, D. Galaktionova, X. Chen, P. Král, and U. Mirsaidov, "Dynamics of amphiphilic block copolymers in an aqueous solution: Direct imaging of micelle formation and nanoparticle encapsulation," *Nanoscale*, vol. 11, no. 5, pp. 2299–2305, 2019.
- [121] K. Gnanasekaran, H. Chang, P. J. Smeets, J. Korpany, F. M. Geiger, and N. C. Gianneschi, "In Situ Ni²⁺ Stain for Liposome Imaging by Liquid-Cell Transmission Electron Microscopy," *Nano Letters*, vol. 20, no. 6, pp. 4292–4297, 2020.
- [122] H. Wu, H. Friedrich, J. P. Patterson, N. A. Sommerdijk, and N. de Jonge, "Liquid-Phase Electron Microscopy for Soft Matter Science and Biology," *Advanced Materials*, vol. 32, no. 25, 2020.
- [123] N. De Jonge and F. M. Ross, "Electron microscopy of specimens in liquid," *Nature Nanotechnology*, vol. 6, no. 11, pp. 695–704, 2011.

-
- [124] I. G. Draganic, *The Radiation Chemistry of Water*. Academic Press, Inc., 1 ed., 2012.
- [125] A. J. Elliot and D. R. McCracken, “Computer modelling of the radiolysis in an aqueous lithium salt blanket: Suppression of radiolysis by addition of hydrogen,” *Fusion Engineering and Design*, vol. 13, no. 1, pp. 21–27, 1990.
- [126] M. A. Hill and F. A. Smith, “Calculation of initial and primary yields in the radiolysis of water,” *Radiation Physics and Chemistry*, vol. 43, no. 3, pp. 265–280, 1994.
- [127] B. Pastina and J. A. LaVerne, “Effect of molecular hydrogen on hydrogen peroxide in water radiolysis,” *Journal of Physical Chemistry A*, vol. 105, no. 40, pp. 9316–9322, 2001.
- [128] N. M. Schneider, M. M. Norton, B. J. Mendel, J. M. Grogan, F. M. Ross, and H. H. Bau, “Electron-Water interactions and implications for liquid cell electron microscopy,” *Journal of Physical Chemistry C*, vol. 118, no. 38, pp. 22373–22382, 2014.
- [129] A. F. Beker, H. Sun, M. Lemang, J. T. Van Omme, R. G. Spruit, M. Bremmer, S. Basak, and H. H. Pérez Garza, “In situ electrochemistry inside a TEM with controlled mass transport,” *Nanoscale*, vol. 12, no. 43, pp. 22192–22201, 2020.
- [130] E. A. Ring and N. De Jonge, “Microfluidic system for transmission electron microscopy,” *Microscopy and Microanalysis*, vol. 16, no. 5, pp. 622–629, 2010.
- [131] F. M. Ross, “Opportunities and challenges in liquid cell electron microscopy,” *Science*, vol. 350, no. 6267, 2015.
- [132] L. A. Giannuzzi and F. A. Stevie, “Introduction to Focused Ion Beams,” in *Compact Plasma and Focused Ion Beams* (L. A. Giannuzzi and F. A. Stevie, eds.), p. 357, New York, NY: Springer Science + Business Media, Inc., 2005.
- [133] N. Bassim, K. Scott, and L. A. Giannuzzi, “Recent advances in focused ion beam technology and applications,” *MRS Bulletin*, vol. 39, no. 4, pp. 317–325, 2014.
- [134] D. Drobne, M. Milani, V. Lešer, and F. Tatti, “Surface damage induced by FIB milling and imaging of biological samples is controllable,” *Microscopy Research and Technique*, vol. 70, no. 10, pp. 895–903, 2007.
- [135] S. Kim, M. Jeong Park, N. P. Balsara, G. Liu, and A. M. Minor, “Minimiza-

- tion of focused ion beam damage in nanostructured polymer thin films,” *Ultramicroscopy*, vol. 111, no. 3, pp. 191–199, 2011.
- [136] R. J. Bailey, R. Geurts, D. J. Stokes, F. de Jong, and A. H. Barber, “Evaluating focused ion beam induced damage in soft materials,” *Micron*, vol. 50, pp. 51–56, 2013.
- [137] N. D. Bassim, B. T. De Gregorio, A. L. Kilcoyne, K. Scott, T. Chou, S. Wirick, G. Cody, and R. M. Stroud, “Minimizing damage during FIB sample preparation of soft materials,” *Journal of Microscopy*, vol. 245, no. 3, pp. 288–301, 2012.
- [138] C. Fager, M. Röding, A. Olsson, N. Lorén, C. Von Corswant, A. Särkkä, and E. Olsson, “Optimization of FIB-SEM Tomography and Reconstruction for Soft, Porous, and Poorly Conducting Materials,” *Microscopy and Microanalysis*, vol. 26, no. 4, pp. 837–845, 2020.
- [139] G. M. McClelland, R. Erlandsson, and S. Chiang, “Atomic force microscopy: General principles and a new implementation,” in *Review of Progress in Quantitative Nondestructive Evaluation* (D. O. Thompson and D. E. Chimenti, eds.), (Boston, MA), pp. 1307–1314, Springer US, 1987.
- [140] Y. F. Dufrêne, T. Ando, R. Garcia, D. Alsteens, D. Martinez-Martin, A. Engel, C. Gerber, and D. J. Müller, “Imaging modes of atomic force microscopy for application in molecular and cell biology,” *Nature Nanotechnology*, vol. 12, no. 4, pp. 295–307, 2017.
- [141] K. Rohtlaid, G. Nguyen, C. Soyer, C. Eric, F. Vidal, and C. Plesse, “Poly(3,4-ethylenedioxythiophene):poly(styrene sulfonate)/polyethylene oxide electrodes with improved electrical and electrochemical properties for soft microactuators and microsensors,” *Advanced Electronic Materials*, vol. 5, pp. 1–11, 03 2019.
- [142] S. Sinha Ray, “Structure and Morphology Characterization Techniques,” in *Clay-Containing Polymer Nanocomposites*, pp. 39–66, Elsevier, 2013.
- [143] C. Fager, S. Barman, M. Röding, A. Olsson, N. Lorén, C. von Corswant, D. Bolin, H. Rootzén, and E. Olsson, “3D high spatial resolution visualisation and quantification of interconnectivity in polymer films,” *International Journal of Pharmaceutics*, vol. 587, no. July, 2020.
- [144] M. Röding, C. Fager, A. Olsson, C. von Corswant, E. Olsson, and N. Lorén, “Three-dimensional reconstruction of porous polymer films from FIB-SEM nanotomography data using random forests,” *Journal of Microscopy*, vol. 281, no. 1, pp. 76–86, 2021.

- [145] G. Stojkov, Z. Niyazov, F. Picchioni, and R. K. Bose, “Relationship between structure and rheology of hydrogels for various applications,” *Gels*, vol. 7, no. 4, 2021.
- [146] L. A. Flanagan, Y.-E. Ju, B. Marg, M. Osterfield, and P. A. Janmey, “Neurite branching on deformable substrates.,” *Neuroreport*, vol. 13, pp. 2411–5, dec 2002.
- [147] A. Tabet, S. Mommer, J. A. Vigil, C. Hallou, H. Bulstrode, and O. A. Scherman, “Mechanical Characterization of Human Brain Tissue and Soft Dynamic Gels Exhibiting Electromechanical Neuro-Mimicry,” *Advanced Healthcare Materials*, vol. 8, no. 10, pp. 1–5, 2019.

